Study of e^+e^- Interactions at Large Electron Positron Collider at CERN

SUCHANDRA DUTTA

Tata Institute of Fundamental Research
MUMBAI

1997

Study of e^+e^- Interactions at Large Electron Positron Collider at CERN

Suchandra Dutta

Tata Institute of Fundamental Research
Bombay 400 005

A Thesis submitted to the

University of Mumbai

for the degree of
Doctor of Philosophy in Physics

March, 1997

To my maternal grandfather
who introduced me to the alphabets.

Acknowledgement

It is a pleasure to acknowledge the guidance of my thesis supervisor, Prof.S.N. Ganguli. I thank him for never being tired of repeatedly explaining to me concepts that I found difficult to grasp at one go.

I acknowledge the hospitality of the European Organisation for Nuclear Research which enabled me to work at CERN. I owe a lot to the members of the LEP accelerator group who kept the machine in excellent condition throughout.

I thank Prof. Atul Gurtu for having taught me the intricacies of lineshape fitting. I am grateful to Prof. Sunanda Banerjee from whom I learnt much of what I know about data analysis and the L3 software.

I thank all the members of the L3 Lineshape group, in particular A. Böhm, J. Field, S. Gentile, J. Mnich, M. Grünewald, C. Paus, U. Uwer, C. Shäfer, L. Malgeri, S. Wynhoff, A. Robohm, T. Siedenburg and Wenwen Lu. Their encouragement, suggestions and useful criticisms went a long way towards improving my analysis.

Mehnaz and Rizwan deserve special mention for their help in minimising the problems with the L3 computing system.

I would like to thank Dr. R. Raghavan, Prof. S. C. Tonwar, Dr. K. Sudhakar, Dr. Tariq Aziz and Dr. Kajari Mazumdar for their suggestions regarding my work.

P. V. Deshpande who kept the computing system in our group at TIFR alive throughout deserves special thanks.

I thank my fellow students in the group Sandeep, Manas, Gobinda, Tania, Satyaki, Raja and Swagoto for providing a stimulating working environment.

I shall always remember the wonderful times spent in the company of Tapan, Debajyoti, Krishanu, Sreerup, Bunty, Zakir, Kartik, Gautam, Monoranjan, Soma, Nirmalya, Mrinal, Dilip and Sandip at TIFR.

Synopsis

Title of the Thesis	:	Study of e^+e^- interactions at Large Electron Positron Collider at CERN.
Name of the Candidate	:	Ms. Suchandra Dutta
Registration Number	:	TIFR–37 dated 23.11.93
Degree	:	Doctor of Philosophy
Subject	:	Physics
Thesis Supervisor	:	Prof. Som Nath Ganguli
Institution	:	Tata Institute of Fundamental Research, Homi Bhabha Road, Mumbai.

The Large Electron Positron (LEP) Collider at the European Centre for Nuclear Research, CERN was constructed to study the properties of Z^0 and $W^\pm$ bosons which are the mediators of the weak interactions. In the first phase of LEP, called LEP1, Z^0 particles are produced from collisions of electron and positron beams each of energy $\approx$ 45 GeV. There are four experiments ALEPH, DELPHI, L3 and OPAL surrounding four interaction regions of the LEP collider.

Experimental High Energy Physics Group in TIFR is a part of the L3 collaboration at LEP. The work presented in the thesis describes the determination of the properties of the Z^0 boson produced in e^+e^- interactions. The analysis was performed using the data collected by the L3 detector from the year 1990 to 1995, the entire period of LEP running at the Z^0 resonance, corresponding to centre of mass energy $E_{cm} \approx 91.0 \pm 3.0$ GeV. The data correspond to the integrated luminosity of 135 pb^{-1}.

The Standard Model [1] of particle physics describes the elementary particles and their interactions. The process $e^+e^- \longrightarrow f\bar{f}$, where $f\bar{f}$ is the fermion-antifermion pair, can be described in the lowest order of the electroweak theory through s-channel [also t channel for $e^+e^- \longrightarrow e^+e^-(\gamma)$] exchange of Z^0 and photon. At centre of mass energies near the Z^0 resonance, the Z^0 exchange term dominates over the γ exchange and the $\gamma - Z^0$ interference terms. This enables us to determine the properties of Z^0 boson, such as the mass (M_Z), the total width (Γ_Z), partial decay width of Z^0 to $f\bar{f}$ pair (Γ_f), from measurements of cross sections. The interference between the vector and axial vector currents introduces the forward backward asymmetry in the process hence it depends on the vector (g_V^f) and axial vector (g_A^f) couplings of Z^0 boson to fermions.

There are corrections to the lowest order interaction $e^+e^- \longrightarrow f\bar{f}$ due to non vanishing contribution from the higher order processes. These are commonly known as radiative corrections [2]. They are of three types : QED corrections, weak corrections and the QCD corrections. Precise measurement of the Z^0 parameters enables us to probe these higher order quantum corrections. QED corrections depending on the fine structure constant α are known with high accuracy. Weak corrections depend on the mass of Z^0, the top quark mass M_t and the Higgs mass M_H, and the QCD correction depends on the strong coupling constant α_s. Measurement of the radiative correction terms is one of the most crucial achievements of LEP experiments.

Z^0 parameters are determined in two ways : (1) Model independent framework and (2) Standard Model framework. In the first case QED corrections are considered fully, the weak corrections are not considered explicitly but they are taken care of by redefining the parameters, such as couplings. The couplings determined in the model independent framework are known as effective couplings. In the Standard Model framework QED as well as weak corrections are considered explicitly; one can estimate the top quark mass from this method. We use the analytical programs ZFITTER [4], ALIBABA [3] for calculating the theoretical predictions and the CERN library package MINUIT [5] for minimisation purpose.

The decay modes of Z^0 are given by $Z^0 \rightarrow$ hadrons (70%), e^+e^-(3.3 %), $\mu^+\mu^-$ (3.3 %), $\tau^+\tau^-$ (3.3 %) and $\nu\bar{\nu}$ (20 %). Z^0 decays into neutrinos are not visible in the detector. From widths of the visible decay channels and the total width of Z^0 one can determine the number of light neutrino species N_ν. We describe here the the methodology to determine the electroweak parameters studying different processes in e^+e^- interactions.

Experimentally one measures (a) the production rates or the cross sections of different processes in the e^+e^- annihilation and (b) the forward backward asymmetry in the final state. From the distribution of the cross sections as a function of centre of mass energy one can extract the shape parameters of the resonance curve which corresponds to different parameters of Z^0 boson. The position of the peak leads to the mass of the Z^0 boson(M_Z), the full-width at half maximum corresponds to the total width (Γ_Z) and the height is proportional to the product of initial and final state partial widths $\Gamma_e\Gamma_f$. Measuring total cross sections of e^+e^-, $\mu^+\mu^-$, $\tau^+\tau^-$ and hadronic channels we can determine separately the partial widths Γ_e, Γ_μ, Γ_τ and Γ_{had}.

(1) <u>Measurement of $e^+e^- \longrightarrow \tau^+\tau^-(\gamma)$ cross section and forward backward asymmetry :</u>
We have determined the cross section and the forward backward asymmetry of the process $e^+e^- \longrightarrow \tau^+\tau^-(\gamma)$. Tau leptons have a very short lifetime of 0.295 ps, and decay immediately even before reaching the first active part of the detector. $\tau^+\tau^-$ events are identified from the decay products of τ's. The selection criteria are designed to select cleanest sample of tau events from all possible background events. Selected events are statistically corrected for acceptance, efficiency and remaining backgrounds for determination of the cross section. Systematic errors are estimated studying all possible sources like selection cuts, Monte Carlo acceptance, trigger, background subtraction and the modelling of the tau decays in the generator. The forward backward asymmetry is determined from a maximum likelihood fit to the differential cross section measured as a function of the scattering angle. The most dominant contribution to the systematic error of the asymmetry measurement comes from the confusion of the charge measurement in the event. In 1992,

1994 and the early part of 1995 LEP ran at Z^0 peak whereas in later part of 1995 there was an energy scan, called 1995 scan, at three energy points on and around the Z^0 peak. The LEP run in 1995 before the energy scan is known as 1995 prescan. Measured values of the cross sections and forward backward asymmetries at different centre of mass energies in different years with errors (statistical and systematic errors are added in quadrature) are summarised in table 1.

Year	$\sqrt{s}$ (GeV)	Cross Section (nb)	Asymmetry
1992	91.293	1.468±0.016	0.013±0.012
1994	91.218	1.472±0.013	0.009±0.008
1995 prescan	91.160	1.464±0.026	0.003±0.024
1995 scan	89.452	0.491±0.013	-0.181±0.033
	91.293	1.522±0.031	-0.016±0.028
	92.984	0.684±0.014	0.152±0.026

Table 1: Measured cross sections and asymmetries of the process $e^+e^- \longrightarrow \tau^+\tau^-(\gamma)$

(2) Determination of Z^0 parameters from L3 experiment : Electroweak parameters are determined by minimising the difference of the measured quantities from their theoretical predictions which is a function of these parameters itself. We define the χ^2 of the fit in the following way,

$$\chi^2 = \Delta^T V^{-1} \Delta$$

Where Δ is a column matrix of dimension n containing the differences corresponding to n measurements and V, known as error correlation matrix, is an n $\times$ n matrix containing the uncertainties of the individual measurements and the correlation between them.

A total of 3.7 million Z^0 decays were observed in all the visible channels. Statistical and systematic errors in the cross section and asymmetry measurements, the uncertainty in the LEP beam energy measurement and the systematic error in the luminosity measurement correlating individual cross section measurements are taken into account in the fitting procedure. The results of the fit are listed in the 2nd column of table 2. The partial widths of the different leptonic channels are in good agreement with each other. The fit is also performed assuming the lepton universality i.e. assuming $\Gamma_e = \Gamma_\mu = \Gamma_\tau \equiv \Gamma_{lept}$ and the results are listed in 3rd column of table 2. The Standard Model predictions for these quantities using $M_t = 175$ GeV, $M_H = 300$ GeV and $\alpha_s = 0.123$ are also listed for comparison.

Parameter	Treatment of Leptons		Standard Model
	non-universality	universality	
M_Z (MeV)	91 188.1±2.9	91 188.1±2.9	
Γ_Z (MeV)	2 499.8±4.3	2 499.8±4.3	2 495.7
Γ_{had} (MeV)	1 745.2±5.5	1 745.6±4.2	1 742.8
Γ_e (MeV)	83.99±0.26	—	
Γ_μ (MeV)	83.78±0.47	—	
Γ_τ (MeV)	84.10±0.62	—	
Γ_{lept} (MeV)	—	83.98±0.19	83.92
Γ_{inv} (MeV)		502.5±3.4	501.4

Table 2: Values of the electroweak parameters as measured in the L3 experiment

(3) Combination of Z^0 parameters from the four LEP experiments : The electroweak results from four LEP experiments ALEPH, DELPHI, L3 and OPAL are combined inside the LEP Electroweak Working Group to obtain the global set of electroweak results from LEP. The correlation between the experiments are properly taken into account in the procedure : (i) the uncertainty in the LEP beam energy measurement is fully correlated among the experiments, (ii) the theoretical uncertainty in the cross section of the Bhabha process used in the luminosity measurement is also correlated. The set of parameters obtained after combination is given in table 3.

Parameter	Treatment of Leptons		Standard Model
	non-universality	universality	
M_Z (MeV)	91 186.3±2.0	91 186.3±2.0	
Γ_Z (MeV)	2 494.6±2.7	2 494.6±2.7	2 495.7
Γ_{had} (MeV)	1 743.6±2.5	1 743.6±2.5	1 742.8
Γ_e (MeV)	83.96±0.15	—	
Γ_μ (MeV)	83.79±0.22	—	
Γ_τ (MeV)	83.72±0.26	—	
Γ_{lept} (MeV)	—	83.91±0.11	83.92
Γ_{inv} (MeV)	—	499.5±2.0	501.4

Table 3: Values of the electroweak parameters after combination of 4 LEP experiments

The invisible width defined as,

$$\Gamma_{inv} = \Gamma_Z - \Gamma_{had} - \Gamma_e - \Gamma_\mu - \Gamma_\tau$$

enables us to determine the number of light neutrino species (N_ν) which are not seen in the detector.

$$N_\nu = \frac{\Gamma_{\rm inv}}{\Gamma_{\rm lept}} \left(\frac{\Gamma_{\rm lept}}{\Gamma_\nu}\right)_{\rm SM}$$

where $\Gamma_{\rm inv}$ and Γ_{lept} are measured experimentally and the ratio $\frac{\Gamma_{lept}}{\Gamma_\nu}$ is calculated from the Standard Model. The number of light neutrino species is found to be :

$$N_\nu = 2.989 \pm 0.012$$

which supports the assumption of three generations of neutrino in the Standard Model.

The precise set of electroweak parameters obtained from the data are then used to estimate the value of the top quark mass in the framework of the Standard Model. The fitted value of the top quark mass is found to be :

$$M_t = 171 \pm 8^{+17}_{-19} \ \text{GeV}$$

where the value of Higgs mass is fixed at 300 GeV during the fit and the effect due the variation of Higgs mass in the range 60-1000 GeV is quoted as the second error. The value of the top quark mass estimated indirectly from LEP experiments agrees very well with the recent direct measurement (175 $\pm$ 6 GeV) by CDF and D0 experiments at Fermilab.

Statement required under Ordinance of 0.770

I hereby state that the work described in this thesis has not been submitted to this or any other university for Ph.D. or any other degree .

Statement required under Ordinance of 0.771

Statement no. 1 regarding new facts :

Determination of the properties of the Z^0 boson, which was the primary goal of the Large Electron Positron collider, has been described in this thesis. Measurements of cross sections and forward backward asymmetries of the process $e^+e^- \longrightarrow \tau^+\tau^-(\gamma)$ at different centre of mass energies are presented with the methodology for the selection of $\tau^+\tau^-$ events. All data collected by the L3 experiment during the LEP running period around Z^0 resonance are used to extract the electroweak parameters. Huge statistics and better understanding of the experimental systematics result in a measurement of electroweak parameters with high precision. This undoubtedly establishes the existence of three light neutrino families. Radiative corrections of the Standard Model are used to estimate the mass of the top quark.

Statement no. 2 regarding author's contribution in joint work :

The work described in the thesis is a result of a collaborative effort of a large number of people in different ways. Over the years, the LEP accelerator has performed excellently as a result of enormous effort of the physicists, engineers and technicians in the LEP accelerator division. The L3 detector and the online and off line software are combined effort of many physicists and engineers from several institutes. References have been properly mentioned whenever use of earlier work has been made. I have done the analysis presented here, under the guidance of Prof. S. N. Ganguli. The major areas where I have contributed are described below.

I have developed the criteria to select tau events and determined the cross sections and forward backward asymmetries for 1992, 1994 and 1995 data, studying all possible sources of systematic errors of these measurements.

The necessary improvements in the fitting package to extract electroweak parameters were implemented by me which was necessary to cope up with the increasing precision of data.

I have used the measured cross sections and asymmetries of all the decay channels of Z^0 to extract the electroweak parameters.

I have also worked for combining the results from the four LEP experiments as a member of the LEP electroweak working group.

Suchandra Dutta
Signature of the Candidate
[Suchandra Dutta]

S N Ganguli
Signature of the Supervisor
[S. N. Ganguli]

References

[1] S. L. Glashow, Nucl. Phys. **22** (1961) 579;
S. Weinberg, Phys. Rev. Lett. **19** (1967) 1264;
A. Salam, in Proceedings of the 8th Nobel Symposium, ed. N. Svartholm, (Almquist and Wiksell, Slockholm, 1968).

[2] *Z Physics at LEP 1* G. Altarelli, R. Kleiss and C. Verzegnassi, CERN Yellow Report 1989.

[3] W. Beenakkar, F. A. Berends and S. C. van dar Marck, Nucl. Phys. **B349** (1991) 323.

[4] D. Bardin *et al.*, FORTRAN package ZFITTER, Preprint CERN-TH 6443/92;
D. Bardin *et al.*, Z. Phys. **C44**(1989) 493 ;
D. Bardin *et al.*, Nucl. Phys. **B351** (1991) 1 ;
D. Bardin *et al.*, Phys. Lett. **B255** (1991) 290 .

[5] F. James, CERN program library Long Writeup 506, MINUIT, 1994.

Contents

List of Figures

List of Tables

Chapter 1

Introduction

The discovery of the carriers of the weak interaction, $W^\pm$ and Z^0 bosons, at the $p\overline{p}$ collider at CERN in 1983, convincingly established the Standard Model of Electroweak Interactions proposed by Glashow, Salam and Weinberg [1] as the description of elementary particle interactions. A precise study of the properties of the newly discovered gauge bosons was a natural step to follow.

The mass and total width of Z^0 are two important electroweak parameters in the Standard Model. The total decay width of Z^0 involves all the decay channels of Z^0 and is related to the fundamental question of the number of fermion generations. The only way to measure the width is to change centre of mass energy for production in small steps around the mass of Z^0. This is difficult in $p\overline{p}$ collider, where actual collision takes place between the constituent partons in proton and anti-proton, which carry a fraction of the available energy. One can not tune the energy at which the partons should take part in hard collisions. Moreover, once a Z^0 is produced it has to be detected from hadronic debris resulting from the partons which did not take part in hard collision. All these demanded high luminosity and high energy e^+e^- colliders where the collision energy could be measured accurately and the environment would be very clean. For a precise determination of the electroweak parameters related to Z^0, the machine would operate at a centre of mass energy on or around the mass of Z^0 boson. The Large Electron Positron (LEP) collider at CERN and the Stanford Linear Collider (SLC) at Stanford Linear Acceleration Centre, came into existence for a precise measurement of the properties of the Z^0 and W bosons.

LEP became operational during the month of September, 1989. The centre of mass energy during phase I was chosen around the known mass of $Z^0 \approx 91$ GeV in order to have resonance production. The very clean environment of the e^+e^- collision was utilised to minimise the background. At that time the knowledge of some of the important electroweak parameters were the following:

(i) The mass of the Z^0 was known as $93.1 \pm 1.0 \pm 3.0$ GeV from UA1 [2],

$91.74 \pm 0.28 \pm 0.93$ GeV from UA2 [3] and $90.9 \pm 0.3 \pm 0.2$ GeV from CDF [4] experiments. The total width of Z^0 was known as $2.7^{+1.2}_{-1.0} \pm 1.3$ GeV from UA1 and $2.7 \pm 2.0 \pm 1.0$ GeV from UA2 experiments.

(ii) There were several attempts to determine the number of light neutrino families which is assumed to be three in the Standard Model. The upper bound of the number of light neutrino families came from the abundance of He^4 from primordial nucleo-synthesis. There were two limits by two groups which are $N_\nu < 5.5$ [5] and $N_\nu < 4.0$ [6]. This was also measured from the ratio of the total widths of Z^0 and $W^\pm$ in $p\bar{p}$ collider at CERN $Sp\bar{p}S$ and the limit obtained at that time was $N_\nu \leq 5.7$ at 90% C.L. [3, 7]. In the e^+e^- accelerator at PEP and PETRA from the study of the $\nu\bar{\nu}\gamma$ events from virtual Z^0 exchange, the 90% C.L. upper limit on light neutrino families was $N_\nu < 5.2$ [8].

(iii) There was an upper limit on the top quark mass (≤ 200 GeV at 90% confidence level) from a detailed analysis of the existing electroweak data and W and Z^0 mass measurements from $p\bar{p}$ collider given by two groups [9].

The parameters of Z^0 become modified from their lowest order predictions due to the effect of radiative corrections. In the vicinity of the Z^0 resonance the largest correction (25%) arises from QED. The weak corrections are of the order of 1%. Precise determination of the parameters of Z^0 allows to detect and estimate these corrections. The most interesting feature of the weak correction is that it is sensitive to the presence of particles in the spectrum which are heavier than Z^0 (top quark for example) and which can not be produced at a centre of mass energy on or around Z^0 resonance. LEP aimed to probe this quantum corrections also.

The work presented in this thesis describes the determination of the properties of Z^0 produced in the e^+e^- interaction at LEP. The huge statistics collected from 1990 to 1995 at LEP are used to study precisely the mass, total width and couplings of Z^0, and the electroweak mixing angle. The number of light neutrino families can be determined from the measurement of the total and partial decay widths of Z^0.

Precise measurement of cross sections for different decay modes of Z^0 is the first step to study its properties. The cross section as a function of the centre of mass energy shows resonance behaviour of Z^0 production. The position of the resonance peak corresponds to the mass, and the full width at half maximum of the curve corresponds to the total width, of Z^0. The height of the curve is proportional to the product of initial and final state partial widths, $\Gamma_e\Gamma_f$. Measurements of cross sections of different decay modes of Z^0 (hadrons, e^+e^-, $\mu^+\mu^-$ and $\tau^+\tau^-$), lead to the determination of mass, total width and the partial widths. The measurements of the forward backward asymmetries in the leptonic final states provide informations about the vector and axial vector couplings of Z^0 to leptons.

Z^0 parameters determined by four LEP experiments are in good agreement with each other. They can be combined to have a global set of parameters to utilise the full statistics at LEP. In the combination procedure we take into account the proper correlation between different measurements. These global set of parameters are finally used to constrain the Standard Model. This provides an estimate of the masses of the top quark and Higgs boson.

The main contribution of the author is in the determination of cross section and the forward backward asymmetry of $e^+e^- \rightarrow \tau^+\tau^-$ events (chapter 6) and the determination of the electroweak results using the measurements in L3 (chapter 7). The contribution also includes the combination of results from four LEP experiments (chapter 8).

A brief outline of each chapter is given in the following,

Chapter 2 discusses the basic concepts of the Standard Model. The process $e^+e^- \rightarrow f\bar{f}$ is described in detail and the experimental observables are defined. The radiative corrections to the lowest order processes are discussed as well.

Chapter 3 describes the Large Electron Positron collider with its injection scheme. The energy calibration and different systematic effects which affect the energy measurement are discussed.

Chapter 4 provides an overview of the L3 experiment describing the sub-detector components in some detail including the online trigger system in L3.

Chapter 5 describes the Monte Carlo simulation of events in the L3 experiment where event generation and detector simulation are discussed. The reconstruction of real and simulated data is discussed thereafter. The measurement of the luminosity in the L3 experiment is also discussed.

Chapter 6 presents the analysis of the process $e^+e^- \rightarrow \tau^+\tau^-$ using L3 detector. The first part describes the selection of a clean sample of $\tau^+\tau^-$ events. The second part deals with the determination of cross section and forward backward asymmetry of the process.

Chapter 7 presents the determination of electroweak parameters from measured cross sections and asymmetries. The incorporation of the experimental statistical and systematic errors of the measurements, the uncertainty in the centre of mass energy and the fitting procedure are discussed. The indirect estimation of the top quark mass in the Standard Model framework is also described.

Chapter 8 presents the combination procedure of the electroweak parameters obtained from the four LEP experiments. Within the framework of the Standard Model the constraint on the top quark and Higgs mass are described.

Chapter 9 summarises the main results of the work presented in this thesis.

Chapter 2

Theoretical Overview

The elementary constituents of matter and their interactions are best explained by the Standard Model of particle physics. The constituents are spin 1/2 point-like fermions, classified into leptons and quarks. The Standard Model, based on a gauge principle, describes strong, weak and electromagnetic interactions. According to the gauge principle, all these forces are mediated by the exchange of integral spin gauge bosons which are the quanta of gauge fields corresponding to the gauge group:

$$\mathrm{SU(3)_C \otimes SU(2)_L \otimes U(1)_Y}$$

Where $\mathrm{SU(3)_C}$, $\mathrm{SU(2)_L}$ and $\mathrm{U(1)_Y}$ are gauge symmetry groups with quantum numbers colour (C), weak isospin (I) and weak hypercharge (Y) respectively.

The weak and electromagnetic interactions are unified into a single electroweak interaction in the Glashow-Salam-Weinberg [1] model, also known as the Standard Model of Electroweak Interactions, based on the corresponding symmetry $\mathrm{SU(2)_L \otimes U(1)_Y}$ which is spontaneously broken to $\mathrm{U(1)_{em}}$.

The gauge theory which describes the strong interaction of the quarks is known as Quantum Chromodynamics (QCD). The symmetry group associated with it is $\mathrm{SU(3)_C}$. The strong interaction is mediated by massless gluons having colour charge. In the Standard Model, QCD is not unified with the electroweak theory.

2.1 Standard Model of Electroweak Physics

One can construct the Lagrangian of the Standard Model starting from the massless spin 1/2 fermionic fields. The Lagrangian for the fermionic fields is given by,

$$\mathcal{L} = \overline{\psi}(i\gamma^\mu \partial_\mu)\psi \tag{2.1}$$

where ψ belongs to the fundamental representation of the gauge group. This Lagrangian is invariant under a general global gauge transformation of the form

$$\psi \longrightarrow \psi' = \mathrm{e}^{-i\vec{\tau}\cdot\vec{\theta}}\psi \tag{2.2}$$

where $\vec{\tau}$ is the set of generators of the gauge group and $\vec{\theta}$ is independent of space and time. On the other hand under local gauge transformation such as

$$\psi \longrightarrow \psi' = e^{-i\vec{\tau}\cdot\vec{\theta}(x)}\psi \tag{2.3}$$

the Lagrangian no longer remains invariant. Introduction of additional massless gauge fields is required to restore the invariance. It follows that for a U(1) symmetry, the gauge fields obey Maxwell's equations. This acts as a motivation for more complicated theories such as the Standard Model.

In electroweak theory the left-handed and right-handed fermions defined as,

$$\psi_L = \frac{1}{2}(1-\gamma_5)\psi \qquad\qquad \psi_R = \frac{1}{2}(1+\gamma_5)\psi \tag{2.4}$$

are assigned to different representations of the gauge group. Right-handed fermions transform under the symmetry group $U(1)_Y$ only, whereas the left-handed fermions transform under both $SU(2)_L$ and $U(1)_Y$. The transformations are given by,

$$\begin{aligned} \psi_{L,R} &\longrightarrow e^{-i\frac{1}{2}g'Y\beta(x)}\psi_{L,R} && : U(1)_Y \\ \psi_L &\longrightarrow e^{-ig\frac{1}{2}\vec{\tau}\cdot\vec{\alpha}(x)}\psi_L && : SU(2)_L \end{aligned} \tag{2.5}$$

where $\vec{\tau}$ are the Pauli matrices.

The Lagrangian, which is invariant under the gauge transformation $SU(2)_L \times U(1)_Y$, has the form given by

$$\mathcal{L}_{\text{fermion}} = \overline{\psi}(i\gamma^\mu D_\mu)\psi \,. \tag{2.6}$$

Here the derivative ∂_μ has been replaced by the covariant derivative D_μ by introducing the gauge fields W_μ and B_μ corresponding to the symmetry groups $SU(2)_L$ and $U(1)_Y$ respectively,

$$D_\mu = \partial_\mu + ig\frac{1}{2}\overrightarrow{W}_\mu\cdot\vec{\tau} + i\frac{1}{2}g'B_\mu Y \quad , \tag{2.7}$$

where g and g' are the gauge couplings corresponding to the gauge groups $SU(2)_L$ and $U(1)_Y$. The gauge fields transform in the following way [12]

$$B_\mu \longrightarrow B_\mu + \partial_\mu\beta(x) \tag{2.8}$$

$$\overrightarrow{W}_\mu \longrightarrow \overrightarrow{W}_\mu + \partial_\mu\vec{\alpha}(x) + g\vec{\alpha}(x)\times\overrightarrow{W}_\mu \tag{2.9}$$

The fermion and gauge fields must be massless to preserve gauge invariance of the Lagrangian. One can generate masses of the fermion and gauge bosons through a mechanism known as spontaneous symmetry breaking discussed in the next section.

2.1.1 The Higgs Mechanism

An SU(2) doublet of scalar fields Φ provides the mechanism for spontaneous symmetry breaking (SSB) [10] through its self interaction to generate masses of gauge fields. Additional Yukawa interaction terms help to generate masses of fermionic fields.

The scalar doublet is specified by

$$\Phi = \begin{pmatrix} \phi^+ \\ \phi^0 \end{pmatrix} \tag{2.10}$$

where ϕ^+ and ϕ^0 are complex scalar fields.

The Lagrangian for the scalar can be written as,

$$\mathcal{L}_{\mathrm{scalar}} = |\mathrm{D}_\mu \Phi|^2 - \mathrm{V}(|\Phi|^2) \tag{2.11}$$

where the potential

$$\mathrm{V}(|\Phi|^2) = \mu^2|\Phi|^2 + \lambda|\Phi|^4 \tag{2.12}$$

The ground state is obtained by minimising the potential V. When $\mu^2 > 0$ the ground state is at $\Phi = 0$. If $\mu^2 < 0$ there is a local maximum at $\Phi = 0$ and the ground state at

$$|\Phi|^2 = -\frac{\mu^2}{2\lambda} \equiv \frac{1}{2}v^2, \tag{2.13}$$

where $v/\sqrt{2}$ is known as the vacuum expectation value of Φ. This new ground state is degenerate and selection of one as the physical vacuum, out of the infinite number of possible minimum values breaks the $\mathrm{SU}(2)_\mathrm{L} \otimes \mathrm{U}(1)_\mathrm{Y}$ symmetry.

By a redefinition of the scalar fields one can remove spurious degrees of freedom corresponding to massless scalar (Goldstone) bosons [11]. The remaining degree of freedom appears as a neutral scalar particle known as the Higgs boson. This is known as the Higgs mechanism.

Although the $\mathrm{SU}(2)_\mathrm{L} \otimes \mathrm{U}(1)_\mathrm{Y}$ symmetry is broken spontaneously there remains a residual $\mathrm{U}(1)_\mathrm{em}$ symmetry corresponding to the generator,

$$\mathrm{Q} = \mathrm{I}_3 + \frac{\mathrm{Y}}{2} \tag{2.14}$$

which implies that there should be a massless gauge boson in the spectrum which is identified as photon, the mediator of electromagnetic interactions. As stated before, this U(1) gauge field satisfies Maxwell's equations.

Fermion masses are generated in a similar manner. The massless fermions are coupled to the scalar field Φ through Yukawa couplings. After the spontaneous symmetry breaking, due to the non-vanishing vacuum expectation value of the scalar field, the fermions acquire mass.

2.1.2 Electroweak Currents

The electroweak Lagrangian thus has the form,

$$\mathcal{L}_{\mathrm{EW}} = \mathcal{L}_{\mathrm{fermion}} + \mathcal{L}_{\mathrm{scalar}} + \mathcal{L}_{\mathrm{gauge}} + \mathcal{L}_{\mathrm{Yukawa}} \tag{2.15}$$

which is invariant under $\mathrm{SU(2)_L} \otimes \mathrm{U(1)_Y}$ local gauge transformations. The individual terms are defined as

$$\begin{aligned}
\mathcal{L}_{\mathrm{fermion}} &= \overline{\psi}\,(\mathrm{i}\gamma^\mu \mathrm{D}_\mu)\,\psi && (2.16)\\
\mathcal{L}_{\mathrm{scalar}} &= (\mathrm{D}_\mu\Phi)^\dagger\,(\mathrm{D}^\mu\Phi) - [\mu^2\Phi^\dagger\Phi + \lambda^4\left(\Phi^\dagger\Phi\right)^2] && (2.17)\\
\mathcal{L}_{\mathrm{gauge}} &= -\frac{1}{4}\mathrm{Tr}[\mathrm{G}_{\mu\nu}\mathrm{G}^{\mu\nu}] - \frac{1}{4}\mathrm{F}_{\mu\nu}\mathrm{F}^{\mu\nu} && (2.18)\\
\mathcal{L}_{\mathrm{Yukawa}} &= \overline{\psi}_{\mathrm{R}}\tilde{\Phi}\psi_{\mathrm{L}} + \overline{\psi}_{\mathrm{L}}\Phi\psi_{\mathrm{R}} && (2.19)
\end{aligned}$$

After the spontaneous symmetry breaking has taken place, one obtains the three known massive $(\mathrm{W_\mu}^\pm, \mathrm{Z}_\mu)$ and one massless (A_μ), physical gauge bosons expressed as linear combinations of $(\mathrm{W_\mu}^1, \mathrm{W_\mu}^2, \mathrm{W_\mu}^3$ and $\mathrm{B}_\mu)$ as given by,

$$\mathrm{W_\mu}^\pm = \frac{\mathrm{W_\mu}^1 \mp i\mathrm{W_\mu}^2}{\sqrt{2}} \tag{2.20}$$

$$\begin{pmatrix} \mathrm{Z}_\mu \\ \mathrm{A}_\mu \end{pmatrix} = \begin{pmatrix} \cos\theta_\mathrm{W} & -\sin\theta_\mathrm{W} \\ \sin\theta_\mathrm{W} & \cos\theta_\mathrm{W} \end{pmatrix} \begin{pmatrix} \mathrm{W_\mu}^3 \\ \mathrm{B}_\mu \end{pmatrix} \tag{2.21}$$

θ_w is known as the electroweak mixing angle or Weinberg angle and follows the relations,

$$e = g\sin\theta_\mathrm{W} = g'\cos\theta_\mathrm{W} \tag{2.22}$$

The masses of the physical gauge bosons are the coefficients of the terms quadratic in gauge fields given by,

$$\begin{aligned}
\mathrm{M_W} &= \frac{1}{2}g\,v\\
\mathrm{M_Z} &= \frac{1}{2}\sqrt{g^2 + g'^2}\;v\\
\mathrm{M_A} &= 0
\end{aligned} \tag{2.23}$$

The interaction Lagrangian between fermions and gauge bosons is given by,

$$\mathcal{L}_{\mathrm{int}} = e\mathrm{J}^\mu_{\mathrm{em}}\mathrm{A}_\mu + \frac{g}{\sqrt{2}}(\mathrm{J}^{\mu+}\mathrm{W_\mu}^+ + \mathrm{J}^{\mu-}\mathrm{W_\mu}^-) + g_\mathrm{z}\mathrm{J}^\mu_\mathrm{z}\mathrm{Z}_\mu \tag{2.24}$$

where

$$g_\mathrm{z} = \frac{e}{\sin\theta_\mathrm{W}\cos\theta_\mathrm{W}} \tag{2.25}$$

The electromagnetic (J^μ_{em}), weak charged ($J^{\mu\pm}$) and the weak neutral (J^μ_Z) currents are defined as,

$$\begin{aligned} J^\mu_{em} &= \overline{\psi}\gamma^\mu Q\,\psi \\ J^{\mu\pm} &= \sqrt{2}\,\overline{\psi}\,\gamma^\mu I^\pm\,\psi \\ J^\mu_Z &= \overline{\psi}\,\gamma^\mu\,(I_3 - Q\sin^2\theta_W)\,\psi \end{aligned} \tag{2.26}$$

where ψ refers to either left-handed (ψ_L) or right-handed (ψ_R) fermions. The $\vec{I}$ operators have the representation $\frac{1}{2}\vec{\tau}$ on ψ_L while the ψ_R has $I = 0$ and we define $I^\pm = \frac{1}{\sqrt{2}}(I_1 \pm i\,I_2)$.

In the low energy limit the standard electroweak charged current interaction is equivalent to a point-like 4-fermion interaction and the Fermi constant G_μ, which is accurately measured from muon decay, is related to g by,

$$\frac{G_\mu}{\sqrt{2}} = \frac{g^2}{8{M_W}^2} \tag{2.27}$$

From the above, the Feynman rules for the fermion and gauge boson interactions are determined. The charged weak currents have the form $\gamma^\mu(1-\gamma_5)$, which is the famous V–A form. The electromagnetic current is purely of vector type and the weak neutral current contains a combination of vector and axial vector couplings.

$$J^\mu_Z = \frac{1}{2}\overline{\psi}_f\gamma^\mu(g^f_V - g^f_A\gamma_5)\psi_f \tag{2.28}$$

where

$$g^f_V = I^f_3 - 2\,Q^f\sin^2\theta_W \tag{2.29}$$

$$g^f_A = I^f_3 \tag{2.30}$$

In table 2.1 we have summarised the various quantum numbers of elementary fermions, gauge bosons and the Higgs boson in the Standard Model. In table 2.2 we have listed the neutral current couplings for the fermions.

The ρ parameter is defined as the ratio of the strengths of the weak neutral current to the weak charged current and is given by,

$$\rho = \frac{(g_Z/M_Z)^2}{(g/M_W)^2} = \frac{{M_W}^2}{{M_Z}^2\cos^2\theta_W} \tag{2.31}$$

In the Standard Model the value of ρ at the tree level is 1 indicating that the charged and neutral weak currents have the same strength.

2.2 e^+e^- Interactions at Z^0 Resonance

The electron-positron annihilation process $e^+e^- \to f\bar{f}$ with fermion pairs in the final state can occur through the exchange of γ and Z^0. The lowest order Feynman diagrams for

Generation	1	2	3	I_3	Y	Q
Leptons	$\begin{pmatrix} \nu_e \\ e \end{pmatrix}_L$	$\begin{pmatrix} \nu_\mu \\ \mu \end{pmatrix}_L$	$\begin{pmatrix} \nu_e \\ e \end{pmatrix}_L$	+1/2 −1/2	−1 −1	0 −1
	e_R	μ_R	τ_R	0	-2	-1
Quarks	$\begin{pmatrix} u \\ d \end{pmatrix}_L$	$\begin{pmatrix} c \\ s \end{pmatrix}_L$	$\begin{pmatrix} t \\ b \end{pmatrix}_L$	+1/2 −1/2	+1/3 +1/3	+2/3 −1/3
	u_R d_R	c_R s_R	t_R b_R	0 0	+4/3 -2/3	+2/3 -1/3
Gauge Bosons	γ Z^0 W^+ W^-					0 0 +1 -1
Higgs	H^0					0

Table 2.1: Elementary particles in the Standard Model

	g_V^f	g_A^f
ν_e, ν_μ, ν_τ	$\frac{1}{2}$	$\frac{1}{2}$
e, μ, τ	$-\frac{1}{2} + 2\sin^2\theta_W$	$-\frac{1}{2}$
u, c, t	$\frac{1}{2} - \frac{4}{3}\sin^2\theta_W$	$\frac{1}{2}$
d, s, b	$-\frac{1}{2} + \frac{2}{3}\sin^2\theta_W$	$-\frac{1}{2}$

Table 2.2: The neutral current couplings

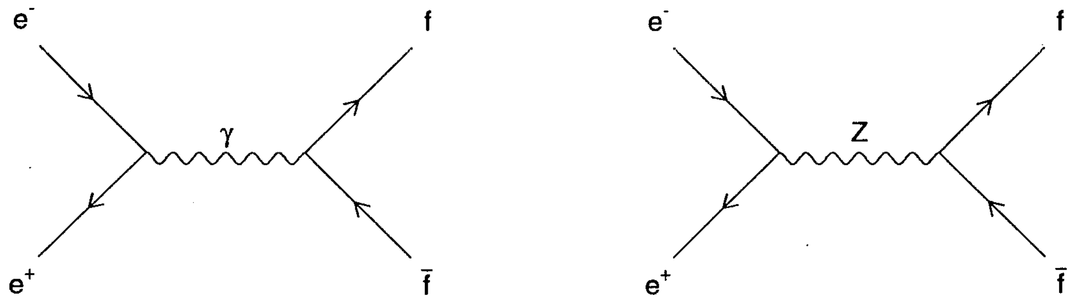

Figure 2.1: Tree level production diagram of the process $e^+e^- \rightarrow f\bar{f}$ through Z^0 and γ exchange

$f \neq e$ are shown in figure 2.1. The cross section has three contributions, pure Z^0 exchange, pure γ exchange and γZ^0 interference. The differential cross section for the process in s-channel at the tree level is given by [13],

$$\frac{d\sigma}{d\cos\theta} = \frac{\pi\alpha^2}{2s} N_f^C \sqrt{1-4\mu_f}\left[G_1(s)(1+\cos^2\theta) + 4\mu_f G_2(s)\sin^2\theta + \sqrt{1-4\mu_f}\, G_3(s) 2\cos\theta\right] \tag{2.32}$$

where N_f^C is the colour factor (1 for leptons and 3 for quarks), $\sqrt{s}$ is the total centre

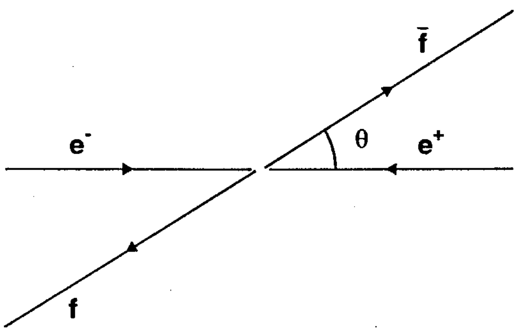

Figure 2.2: Definition of the scattering angle

of mass energy, $\mu_f = m_f^2/s$ and θ is the scattering angle (as shown in figure 2.2) in the centre-of-mass frame. The coefficients G_1, G_2 and G_3 can be expressed in terms of the weak coupling constants g_V, g_A and fermionic charges Q_e, Q_f.

$$\begin{aligned}
G_1 &= Q_e^2 Q_f^2 - 2 g_V^e g_V^f Q_e Q_f \mathrm{Re}\chi(s) + ((g_V^e)^2 + (g_A^e)^2)((g_V^f)^2 + (1-4\mu_f)(g_A^f)^2)|\chi(s)|^2 \\
G_2 &= Q_e^2 Q_f^2 - 2 g_V^e g_V^f Q_e Q_f \mathrm{Re}\chi(s) + ((g_V^e)^2 + (g_A^e)^2)(g_V^f)^2 |\chi(s)|^2 \\
G_3 &= -2 g_A^e g_A^f Q_e Q_f \mathrm{Re}\chi(s) + 4 g_V^e g_A^e g_V^f g_A^f |\chi(s)|^2
\end{aligned} \tag{2.33}$$

Where $\chi(s)$ has the Breit-Wigner form

$$\chi(s) = \frac{1}{4\sin^2\theta_W \cos^2\theta_W} \frac{s}{(s - M_Z{}^2) + iM_Z\Gamma_Z} \tag{2.34}$$

At LEP energies $\mu_f << 1$ for all fermions which can be pair-produced in the Standard Model, hence the differential cross section simplifies to

$$\frac{d\sigma}{d\cos\theta} = \frac{\pi\alpha^2}{2s} N_f^C \left[G_1(s)(1+\cos^2\theta) + G_3(s) 2\cos\theta\right] \tag{2.35}$$

The total cross section can be obtained by integrating the differential cross section over the full range of $\cos\theta$.

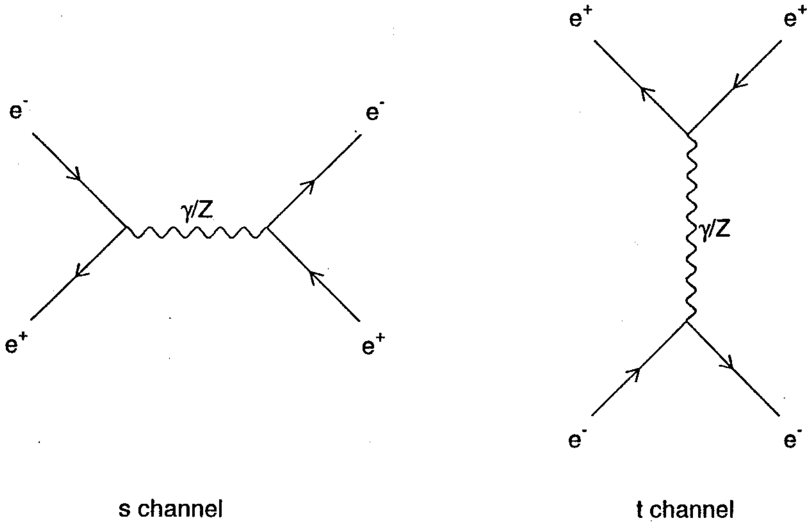

Figure 2.3: s and t channel production diagram for Bhabha scattering $e^+e^- \to e^+e^-$

In case of Bhabha scattering $e^+e^- \to e^+e^-$, initial and final states are identical and there are additional contributions to the total cross section due to t-channel exchange of the boson as shown in the figure 2.3. The total cross section of $e^+e^- \to e^+e^-$ thus has contributions from s-channel, t-channel and interference of s and t channels. The contribution from s-channel is as described above. Detailed descriptions from t–channel and s–t interference terms are given in reference [15].

2.2.1 Cross Section

The total production cross section of the process $e^+e^- \to f\bar{f}$ in the lowest order can be written as

$$\begin{aligned} \sigma^o_{tot} &= \frac{4\pi\alpha^2}{3s} N_f^C \left(Q_e^2 Q_f^2 - 2g_V^e g_V^f Q_e Q_f \mathrm{Re}\chi(s) + [(g_V^e)^2 + (g_A^e)^2][(g_V^f)^2 + (g_A^f)^2]|\chi(s)|^2\right) \\ &= \sigma^o_\gamma + \sigma^o_Z + \sigma^o_{Z\gamma} \end{aligned} \tag{2.36}$$

The γ exchange contribution or the pure QED cross section is given by,

$$\sigma^o_\gamma = \frac{4\pi\alpha^2}{3s} N^C_f Q^2_e Q^2_f \tag{2.37}$$

The pure Z^0 exchange contribution to the cross section is given by,

$$\sigma^o_Z = \frac{\pi\alpha^2}{12\sin^4\theta_W \cos^4\theta_W} N^C_f [(g^e_V)^2 + (g^e_A)^2][(g^f_V)^2 + (g^f_A)^2] \frac{s}{(s - {M_Z}^2)^2 + {\Gamma_Z}^2 {M_Z}^2} \tag{2.38}$$

which is of a Breit-Wigner form where M_Z and Γ_Z are the mass and decay width of the Z^0 boson respectively. At centre of mass energy $\sqrt{s} \sim M_Z$ this cross section is highly enhanced compared to the pure QED contribution.

The contribution of the γZ^0 interference to the cross section is given by,

$$\sigma^o_{\gamma Z} = -\frac{2\pi\alpha^2}{3\sin^2\theta_W \cos^2\theta_W} Q_e Q_f N^C_f g^e_V g^f_V \frac{(s - {M_Z}^2)}{(s - {M_Z}^2)^2 + {\Gamma_Z}^2 {M_Z}^2} \tag{2.39}$$

This contribution is very small compared to that of the Z^0 exchange and vanishes at $\sqrt{s} = M_Z$.

The partial width for $Z^0 \longrightarrow f\bar{f}$ is calculated to be

$$\Gamma_f = \frac{\alpha M_Z}{12\sin^2\theta_W \cos^2\theta_W} N^C_f [(g^f_V)^2 + (g^f_A)^2] \tag{2.40}$$

The Z^0 exchange contribution in terms of the partial widths of initial and final states can be written as

$$\sigma^o_Z = \frac{12\pi}{{M_Z}^2} \Gamma_e \Gamma_f \frac{s}{(s - {M_Z}^2)^2 + {\Gamma_Z}^2 {M_Z}^2} \tag{2.41}$$

where Γ_e is the partial width of $Z^0 \rightarrow e^+e^-$.

We can define the cross section at $\sqrt{s} = M_Z$ for the channel $e^+e^- \rightarrow f\bar{f}$ as,

$$\sigma^{peak}_Z = \frac{12\pi}{{M_Z}^2} \frac{\Gamma_e \Gamma_f}{{\Gamma_Z}^2} \tag{2.42}$$

Z^0 decays into $q\bar{q}$(70%) , $l\bar{l}$ (10%) and $\nu\bar{\nu}$ (20 %) channels where q = (u,d,c,s,b), l = (e, μ, τ), and $\nu = (\nu_e, \nu_\mu, \nu_\tau)$. All quark productions are considered collectively as *hadronic channel* and the hadronic width is defined as,

$$\Gamma_{had} = \Gamma_u + \Gamma_d + \Gamma_c + \Gamma_s + \Gamma_b \tag{2.43}$$

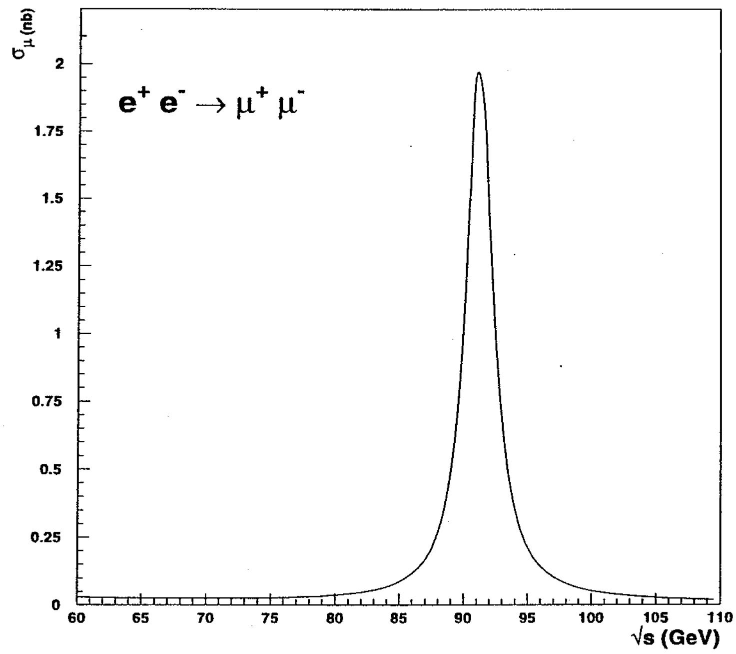

Figure 2.4: Cross Section as a function of centre of mass energy

Figure 2.4 shows the cross section for $e^+e^- \to \mu^+\mu^-$ as a function of centre of mass energy. The position of the peak in the resonance curve is determined by the mass (M_Z) of the Z^0, the width of the curve by the total width Γ_Z and the height of the curve corresponds to the product of the partial widths $\Gamma_e\Gamma_f$.

The total width Γ_Z is the sum of the partial widths of all possible decay widths of Z^0. In the Standard Model the number of light neutrino families is assumed to be 3 hence the total width can be written as

$$\Gamma_Z = \Gamma_{had} + 3\Gamma_\nu + \Gamma_e + \Gamma_\mu + \Gamma_\tau \tag{2.44}$$

Further, in the Standard Model lepton universality is implied i.e. the partial widths Γ_e, Γ_μ and Γ_τ are expected to be identical except for a small effect due to mass differences between e, μ and τ.

Assuming lepton universality and neglecting mass effects we can write,

$$\Gamma_Z = \Gamma_{had} + 3(\Gamma_\nu + \Gamma_{lept}) \tag{2.45}$$

The neutrinos are not detectable experimentally, so we cannot measure the width Γ_ν directly. We define the sum of the widths due to decays of Z^0 in all ν channels as invisible width, Γ_{inv}, and this is estimated from equation (2.45) as follows:

$$\Gamma_{inv} = \Gamma_Z - \Gamma_{had} - 3\Gamma_{lept} \tag{2.46}$$

2.2.2 Forward Backward Asymmetry

The forward backward asymmetry in $e^+e^- \to f\bar{f}$ is defined as

$$A_{FB} = \frac{\sigma_F - \sigma_B}{\sigma_F + \sigma_B} \tag{2.47}$$

where σ_F and σ_B are the cross sections when the final state fermion scatters in the forward ($\cos\theta > 0$) and backward ($\cos\theta < 0$) directions respectively with respect to the electron direction.

$$\sigma_F = \int_0^1 \frac{d\sigma}{d\cos\theta} d\cos\theta \qquad \sigma_B = \int_{-1}^0 \frac{d\sigma}{d\cos\theta} d\cos\theta \tag{2.48}$$

Experimentally asymmetry can be measured for charged fermions only and hence it is also called forward backward charge asymmetry. From the equation (2.32) for the differential cross section we can write [16]

$$A_{FB} = \frac{3G_3}{4G_1} \tag{2.49}$$

At the Z^0 peak the above equation simplifies to

$$A_{FB} = \frac{3}{4} A_e A_f \tag{2.50}$$

where

$$\begin{aligned} A_e &= \frac{2\, g_V^e g_A^e}{(g_V^e)^2 + (g_A^e)^2} \\ A_f &= \frac{2\, g_V^f g_A^f}{(g_V^f)^2 + (g_A^f)^2} \end{aligned} \tag{2.51}$$

2.2.3 Polarisation Asymmetry

The polarisation asymmetry is defined as

$$A_{pol} = \frac{\sigma_{(\lambda_f=+1)} - \sigma_{(\lambda_f=-1)}}{\sigma_{(\lambda_f=+1)} + \sigma_{(\lambda_f=-1)}} \tag{2.52}$$

where λ_f is the helicity of the final state fermion and $\sigma_{(\lambda_f=+1)}$ and $\sigma_{(\lambda_f=+1)}$ are the cross sections when the fermion is produced with positive and negative helicity respectively.

At $\sqrt{s} = M_Z$ we have

$$\begin{aligned} A_{pol} &= -A_f \\ &= -\frac{2g_V^f g_A^f}{(g_V^f)^2 + (g_A^f)^2} \end{aligned} \tag{2.53}$$

2.3 Higher Order Corrections

In the above sections, so far, we have discussed only the lowest order diagrams for the process $e^+e^- \to f\bar{f}$. It is important to take into account corrections from higher order diagrams. The higher order diagrams, as shown in figure 2.5, involve additional interaction

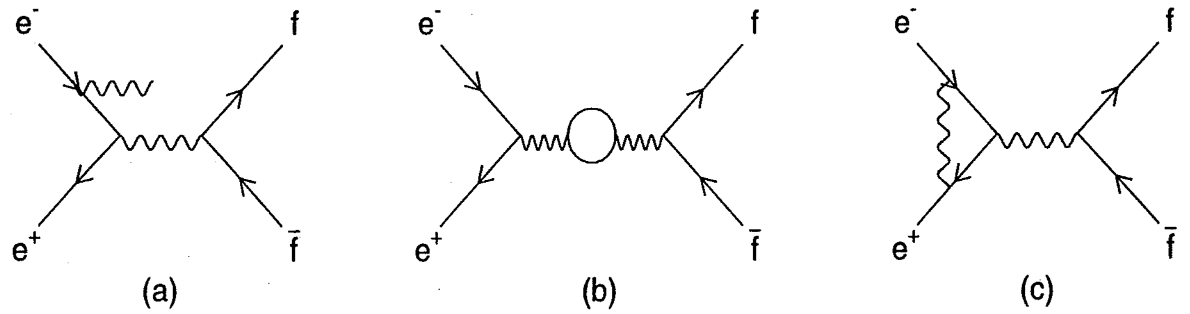

Figure 2.5: Examples of the important radiative corrections to the process $e^+e^- \to f\bar{f}$.(a) Bremsstrahlung correction, (b) Propagator correction, (c) Vertex correction

vertices and hence contain higher powers of the coupling constants. However, the particle content in the final state does not get modified (except for bremsstrahlung correction). The corrections to the tree level observables induced by the higher order terms are called *radiative corrections.* These corrections can be divided into different categories such as QED corrections, weak corrections and QCD corrections. Divergences in the corrections arising from diagrams containing loops are absorbed by redefinition of the parameters. This is known as renormalisation.

2.3.1 QED Corrections

The QED radiative corrections include diagrams with radiation of photons added at tree level to the process $e^+e^- \to f\bar{f}$. The photons can be radiated either from the initial state or from the final state. In addition to the real photon corrections there are virtual photon corrections also. Some of the possible diagrams are shown in figure 2.6. The most prominent contribution comes from the initial state radiations (ISR) at LEP energies. Initial state radiation changes the centre of mass energy of the collision and as a result the Z^0 lineshape curve is changed. For a centre of mass energy below M_Z, due to emission of an ISR photon, the interaction takes place at a reduced effective centre of mass energy. This corresponds to a lower cross section for that energy point. On the other hand, for a centre of mass energy above M_Z, emission of an ISR photon brings the effective centre of mass energy closer to the Z^0 pole, which results in an enhanced cross section at that energy point. As a result the measured peak position appears to be higher in energy and

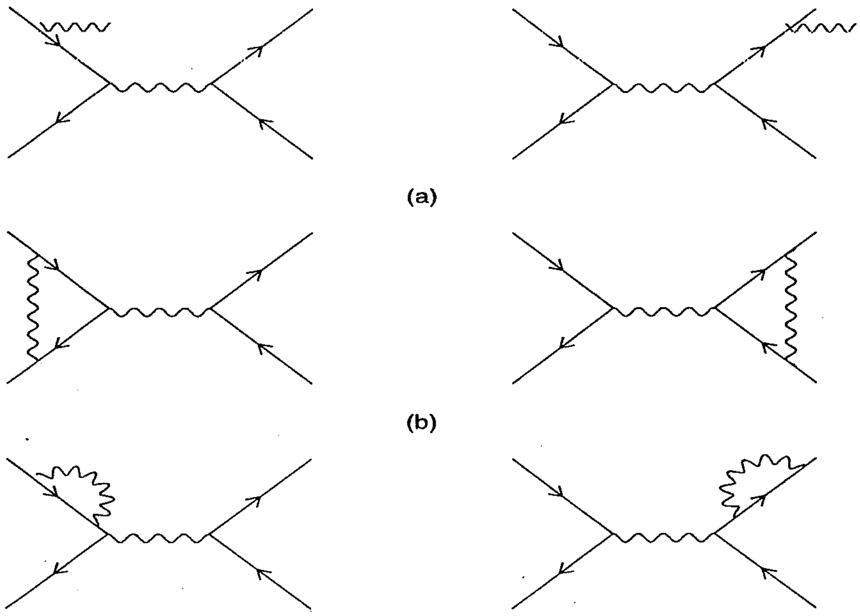

Figure 2.6: Diagrams contributing to QED corrections in initial and final state. (a) Bremsstrahlung (b),(c) virtual photon corrections

the width is broadened. Figure 2.7 illustrates these effects discussed above. The ISR effect is taken into account by convoluting the total cross section (Born) using a radiator function in the following way,

$$\sigma(s) = \int_0^{1-\frac{4m_f^2}{s}} \sigma_0(s')G(x,s)dx \tag{2.54}$$

where x is the fractional energy of the emitted photon : $x = \frac{E_\gamma}{E_b}$, and $\sqrt{s} = 2E_b$ is the centre of mass energy where E_b is the energy of the e^+/e^- beam. $\sigma_0(s')$ is the total cross section evaluated at the reduced centre of mass energy $\sqrt{s'}$ where

$$s' = s(1-x)$$

$G(x,s)$ is the radiator function which specifies the probability of photon radiation. The final state radiative corrections are included as a multiplicative factor $(1+\delta_{QED})$ in the decay widths as,

$$\Gamma_f \longrightarrow \Gamma_f(1+\delta_{QED}) \tag{2.55}$$

where,

$$\delta_{QED} = \frac{3\alpha}{4\pi}Q_f^2 \tag{2.56}$$

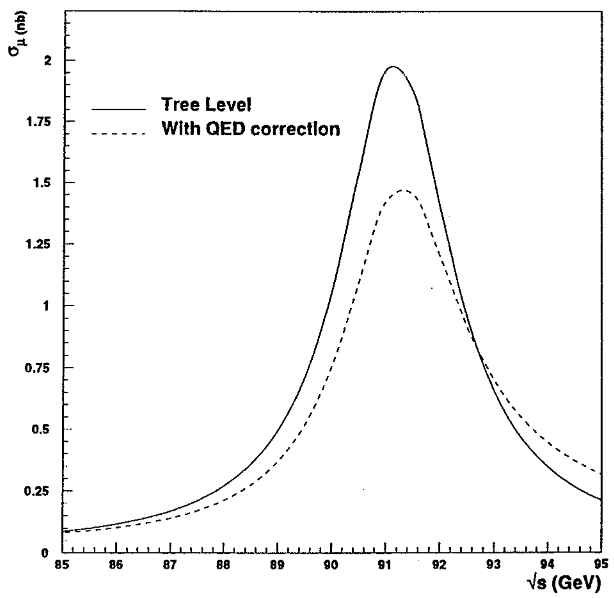

Figure 2.7: The cross section as a function of centre of mass energy for the process $e^+e^- \rightarrow \mu^+\mu^-$. The solid curve shows the tree level cross sections and the dashed one shows the QED corrected one.

The effect of QED radiative corrections is large. As an example, at the peak ($\sqrt{s} = M_Z$) the cross section is decreased by about 25% due to this correction.

2.3.2 Weak Corrections

The weak corrections arise from non-photonic higher order contributions to the tree level processes. The higher order diagrams consist of loops of fermions, gauge bosons or Higgs bosons. The weak corrections reflect the detailed structure of the electroweak theory and are sensitive to the parameters of the theory. The size of the weak corrections are much smaller ($\sim$ 1 %) compared to the QED corrections. Therefore a very accurate prediction of the QED correction is needed to probe the weak radiative corrections using experimental measurements. The weak corrections are classified as propagator corrections, vertex corrections and box diagram corrections.

Propagator Correction :

Diagrams contributing to the propagator correction are shown in figure 2.8. These corrections are independent of the flavour of the initial and final state fermions.

Vertex Correction :

Figure 2.9 shows the diagrams contributing to the vertex correction. This correction depends on the fermion species. For b quark the correction is largest due to the

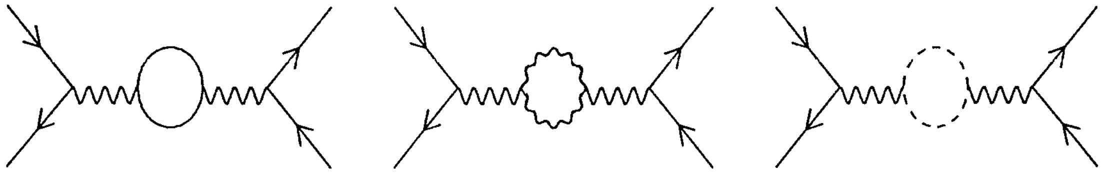

Figure 2.8: Propagator corrections

presence of the large top quark mass in the coupling. This non-vanishing contribution is due to the fact that the value of Cabibbo-kobayashi-Maskawa matrix element is almost unity as top and bottom quarks are the isodoublet partners. As a result of this effect Γ_b gets an additional contribution of 1% .

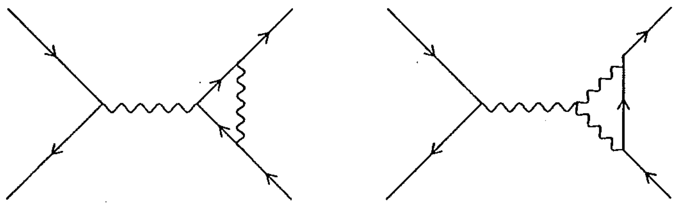

Figure 2.9: Vertex corrections

Box Diagram correction :

The corrections due to the box diagrams containing Z^0 and $W^{\pm}$ exchange shown in figure 2.10 have very small contributions at centre of mass energies near the Z^0 peak.

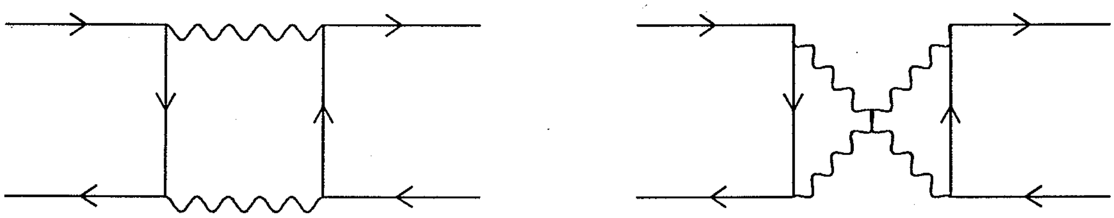

Figure 2.10: Box diagram corrections

The Fermi coupling constant gets modified with the inclusion of the higher order corrections to,

$$G_\mu = \frac{\pi\alpha}{\sqrt{2}{M_Z}^2 \sin^2\theta_W \cos^2\theta_W} \cdot \frac{1}{1-\Delta r} \tag{2.57}$$

where Δr estimates the effects of the radiative corrections [14]. Δr accounts for genuine weak corrections and the contribution due to running of the electromagnetic coupling constant α is written as,

$$\alpha(M_Z{}^2) = \frac{\alpha(0)}{1-\Delta\alpha} \tag{2.58}$$

We can write,

$$\frac{1}{1-\Delta r} = \frac{1}{1-\Delta\alpha}\cdot\frac{1}{1+\frac{\cos^2\theta_W}{\sin^2\theta_W}\Delta\rho} + (\Delta r)_{\text{remainder}} \tag{2.59}$$

The radiative correction to the ρ parameter which is the ratio of the neutral to charged current amplitudes and is unity at the tree level, is given by

$$\rho = 1+\Delta\rho \tag{2.60}$$

where,

$$\Delta\rho = \frac{3\,G_\mu\,M_t{}^2}{8\sqrt{2}\,\pi^2} \tag{2.61}$$

The term $(\Delta r)_{\text{remainder}}$ in equation (2.59) contains contributions from Higgs and top mass as given by,

$$(\Delta r)^{\text{top}}_{\text{remainder}} = \frac{\sqrt{2}G_\mu M_W{}^2}{8\pi^2}\left(\frac{\cos^2\theta_W}{\sin^2\theta_W}-\frac{1}{3}\right)\log\frac{M_t{}^2}{M_W{}^2}+\ldots. \tag{2.62}$$

$$(\Delta r)^{\text{Higgs}}_{\text{remainder}} = \frac{\sqrt{2}G_\mu M_W{}^2}{16\pi^2}\cdot\frac{11}{3}\left(\log\frac{M_H{}^2}{M_W{}^2}-\frac{5}{6}\right)+\ldots. \tag{2.63}$$

This signifies that the influence of the top quark mass and the Higgs boson mass on the observables becomes accessible through the weak corrections, although the particles themselves may not be directly observed.

Improved Born Approximation

The weak corrections can be absorbed in the lowest order Born formulae by a redefinition of the coupling constants. This is known as the improved Born approximation. In this framework the couplings and the width of Z^0 entering in the propagator become dependent on the energy and the masses of virtual particles in the radiative corrections:

$$\begin{aligned}
\Gamma_Z &\longrightarrow \Gamma_Z(s) = \frac{s}{M_Z{}^2}\Gamma_Z \\
\sin^2\theta_W &\longrightarrow \sin^2\overline{\theta}_w = \sin^2\theta_W(1+\frac{\cos^2\theta_W{}^2}{\sin^2\theta_W{}^2}\Delta\rho) \\
g^f_A &\longrightarrow \overline{g^f_A} = \sqrt{\rho_f}I_3 \\
g^f_V &\longrightarrow \overline{g^f_V} = \sqrt{\rho_f}(I_3 - 2|Q_f|\sin^2\overline{\theta}_w)
\end{aligned} \tag{2.64}$$

2.3.3 QCD Corrections

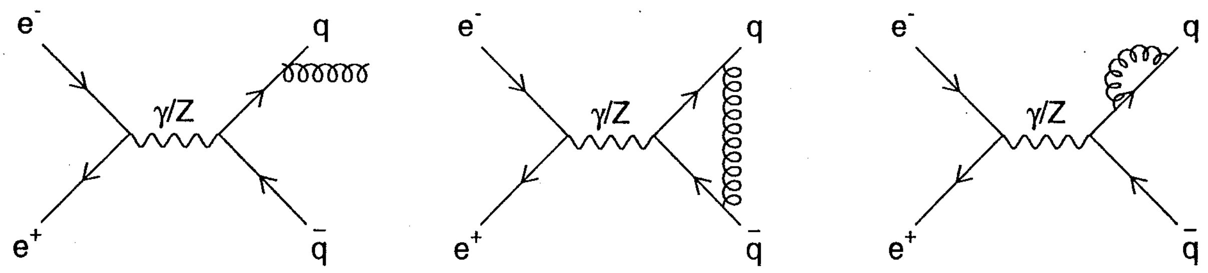

Figure 2.11: QCD corrections of the process $e^+e^- \rightarrow q\overline{q}$

QCD radiative corrections are principally due to the emission of gluons in the final state of the process $e^+e^- \rightarrow q\overline{q}$. The diagrams are shown in figure 2.11. This correction is taken care of by a multiplicative factor in the hadronic width and is given by,

$$\Gamma_{\mathrm{had}} \longrightarrow \Gamma_{\mathrm{had}}(1+\delta_{\mathrm{QCD}}) \tag{2.65}$$

These corrections are applied to the processes containing quarks in the final state as the gluons do not couple to leptons. δ_{QCD} is expanded in powers of $\frac{\alpha_s}{\pi}$, where α_s is the strong coupling constant [17], as follows :

$$\delta_{\mathrm{QCD}} = 1.060(\frac{\alpha_s}{\pi}) + 0.90(\frac{\alpha_s}{\pi})^2 - 15(\frac{\alpha_s}{\pi})^3 \tag{2.66}$$

The effect of δ_{QCD} is to increase the hadronic width by $\sim 4\%$.

Chapter 3

Large Electron Positron Collider

3.1 The LEP Machine

The Large Electron Positron (LEP) collider at CERN is constructed [22] to study the physics of e^+e^- interactions high energies. In the first phase LEP I, the centre of mass energy of LEP was around 91 GeV in order to produce the weak vector boson Z^0. The second phase is LEP II, where the centre of mass energy is gradually increased above the threshold for the pair production of W bosons.

The LEP storage ring is situated in an underground tunnel of 26.7 km circumference extending both in France and Switzerland as shown in figure 3.1. The tunnel is located 50−150 m beneath the surface level. The ring is in the form of an octagon consisting of eight straight sections and eight curved sections.

- The curved sections are each 2840 m long and composed of horizontally deflecting dipole magnets and alternating focusing and defocusing quadrupole magnets. There are a total of 3304 dipole magnets which produce a magnetic field up to 0.134 T, to keep the electrons and positrons on or near the ideal orbit during acceleration and storage. The particles in the ideal orbit do not get deflected by the quadrupole magnets.

- The straight sections are 490 m long. Each of the eight straight sections contains one interaction point (IP). Out of them, four points are equipped with four detectors, ALEPH (IP4) [19], DELPHI (IP8) [20], L3 (IP2) [18] and OPAL(IP6) [21]. Both sides of each detector are equipped with superconducting quadrupole magnets which focus the beam to the interaction point in order to increase the luminosity.

The electron and positron beams are accelerated from the injection energy to the collision energy by the radio frequency (RF) fields from acceleration cavities. During the LEP I phase, copper cavities were used for acceleration and they have been gradually replaced by superconducting cavities in the LEP II phase.

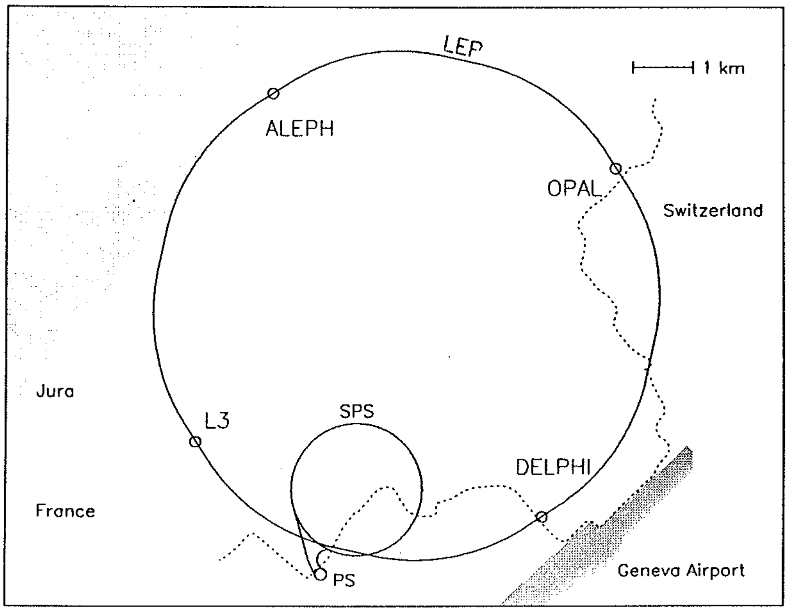

Figure 3.1: The LEP storage Ring

There are four NMR probes to monitor the magnetic field produced by the dipole magnets. Two of the NMR probes are placed in the dipole magnets inside the LEP tunnel near IP4 (NMROCT4) and IP8 (NMROCT8). The other two probes NMRREF and NMRVAC are located in the reference magnet which is situated in a surface building and connected in series with the tunnel dipole magnets. The dipole field in the LEP tunnel was monitored by the NMR probes for the first time in 1995 [35].

The electrons and positrons circulating in the ring lose energy due to synchrotron radiation. The amount of synchrotron radiation depends on the energy of the particle E and the radius of the orbit r ($\propto E^4/r$). At 45 GeV the energy loss is about 120 MeV per turn. The energy loss is compensated by the RF field.

The LEP injector system is shown in figure 3.2. The injection is done in different steps using other existing accelerator facilities at CERN.

- The LEP Injector Linac (LIL) system consists of two linear accelerators. The first one accelerates electrons up to 200 MeV and shoots them onto a tungsten target to produce positrons. The positrons and the electrons are then accelerated to 600 MeV by the second Linac.

- The electrons and positrons are injected into the Electron Positron Accumulator (EPA) from LIL as the next step. The EPA compresses the pulses into, so called, *bunches*.

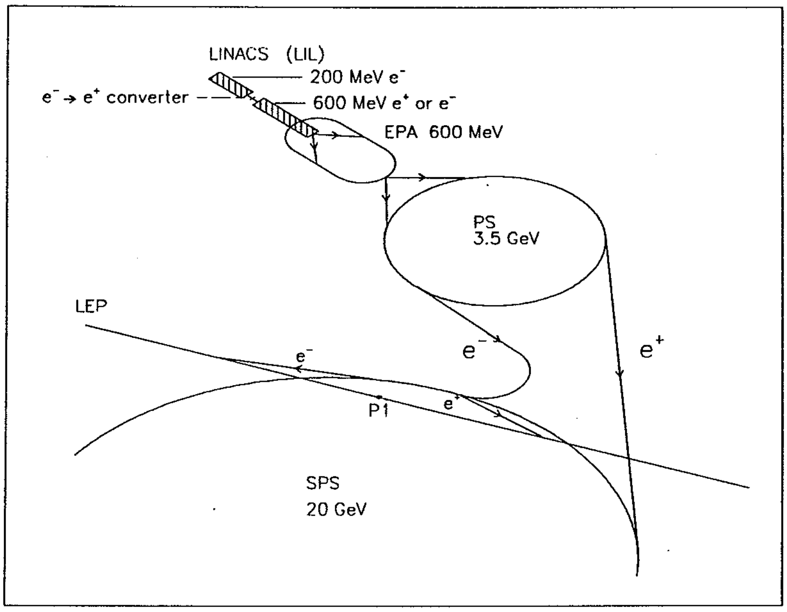

Figure 3.2: Injector system of LEP

- The bunches are thereafter accelerated in the Proton Synchrotron (PS) to 3.5 GeV.
- The Super Proton Synchrotron (SPS) then accelerates the electron and positron bunches further to 20 GeV.
- Finally the bunches are injected into the main LEP ring where they are accelerated to the required energy.

The electron and positron beams circulate in the LEP ring in opposite directions and are kept separated by electrostatic separators during the acceleration phase. After achieving the required energy, the bunches are brought to collision at the interaction points.

The beam energy and the luminosity are the two basic considerations for the design of a particle collider. The beam energy is dictated by the physics process of interest. LEP has been designed to study the properties of the Z^0 (LEP I phase) and $W^{\pm}$ (LEP II phase) bosons. The luminosity defines the rate of the interaction per unit cross section and is given by :

$$\mathcal{L} = \frac{N_e N_p n_b f_{rev}}{4\pi\sigma_x\sigma_y} \tag{3.1}$$

where $N_{e,p}$ are the number of electrons, positrons per bunch, n_b is the number of bunches per beam and f_{rev} is the revolution frequency of a bunch. σ_x and σ_y are the transverse beam sizes in the and perpendicular to the bending plane respectively. The design luminosity of LEP, during the phase I operation, is $1.7 \times 10^{31}\,\mathrm{cm}^{-2}\,\mathrm{s}^{-1}$.

LEP operated with 4 bunches per beam from 1990 to 1991. To increase the luminosity, the number of bunches was increased to 8 from 1992 to 1994 using *Pretzel scheme* [23]. In this scheme, the current per bunch was lower, hence only 50% increase in luminosity was achieved. In order to increase the luminosity further, the LEP operation entered the bunch train mode [31] from 1995. There has been four trains, each of 220 m long and consisting of 3 bunches.

Some of the parameters of LEP operation [34], such as, number of energy points scanned, the centre of mass energy, number of bunches per beam, integrated luminosity and the efficiency, which is the ratio of the actual time of physics run in a year to the total time allocated for physics run, are listed in table 3.1. In 1993 and 1995 significant amount of time was spent for energy calibration.

Year	1990	1991	1992	1993	1994	1995
No. of energy points	7	8	1	4	1	4
CM energy (GeV)	88.23–94.22	88.48–93.72	91.29	89.45–93.03	91.22	89.45–92.98
Number of bunches	4+4	4+4	4+4,8+8	8+8	8+8	12+12
$\int \mathcal{L}$ pb^{-1}	7.6	17.3	28.6	40.0	64.4	39.9
Efficiency (%)	42	45	51	55	59	46

Table 3.1: The performance of LEP from 1990 to 1995

3.2 Energy Calibration of LEP

The main purpose of the LEP collider is the precision measurement of mass and width of the Z^0 boson which are fundamental parameters of the electroweak theory. The production rate of the Z^0 boson shows a resonance behaviour when the centre of mass energy is in the vicinity of the Z^0 mass. The position and width of the resonance curve corresponds to the mass (M_Z) and total width (Γ_Z) of the Z^0 boson respectively, which are extracted from the energy dependence of the cross section of e^+e^- annihilations. Since the error in the beam energy reflects directly on the error in the Z^0 mass, it is essential to have a very precise energy calibration of e^- and e^+ beams at LEP.

The momentum of the electron and positron beams circulating in the LEP ring is proportional to the bending magnetic field integrated over the path length of the particles. The momentum p of a particle of charge Q, moving in a magnetic field of strength B, in a circular orbit of radius R is given by the relation $p = Q\,B\,R$.

The momentum of the particles traversing the ideal orbit, i.e. the centre of the quadrupole magnets, are determined by the field due to the dipole magnets. There is a small contribution due to the earth's magnetic field. For particles moving in non central orbits, contributions come from quadrupole magnets also.

The knowledge of the magnetic field is the basic ingredient for the energy calibration of LEP. There are different techniques used for the energy measurement and a combined analysis is done to obtain a precise energy calibration of LEP.

3.2.1 Field Display Measurement

The magnetic field produced by the dipole magnets are monitored using a rotating coil which measures the magnetic field in a reference magnet. The reference magnet is powered in series with the dipole magnets in the LEP ring and is kept in a controlled environment with temperature stabilisation. The magnetic field strength is determined by measuring the induced current in the rotating coil. The field is measured regularly and energy estimated from this is used as the reference value for individual fills of the machine. The corrections applied to it are based on the other calibration techniques. The main advantage of this measurement is that it can be performed even when the LEP ring is filled with beam. The reproducibility of the field display measurement is $\pm 2.5 \times 10^{-5}$ [24]. After installation of the NMR probes NMRREF and NMRVAC in the reference magnet, the field is measured simultaneously by the rotating coil and the NMR probes.

3.2.2 Flux Loop Measurement

The dipole magnets in the LEP ring are equipped with closed electrical loops of copper wire. There are eight such loops, each one passing through the dipole magnets in an octant of the ring. The alternating current in the dipole magnets produces induced current in the loop which is a direct measurement of the field produced by the dipole magnets in the LEP ring. The method allows the extrapolation of the field display measurement over the whole ring taking into account the non ideal effects. The absolute calibration of the flux loop measurement was performed with a precision of $\frac{\Delta E}{E} \sim 10^{-4}$ [24,25] before the installation of the dipole magnets in the ring. This method is insensitive to constant fields like earth's magnetic field and does not take into account the additional bending produced by quadrupole magnets to the particles circulating in the non central orbits.

3.2.3 Proton Calibration

Proton calibration is used to measure the momentum of the electron and positron beams circulating in the central orbit of the LEP ring. The calibration is performed at an energy of 20 GeV for the particles moving in the central orbit. The orbit, passing through the centres of the quadrupole magnets, is called central orbit. Particles traversing through the central orbit experience magnetic field produced by dipole magnets only.

The length of the central orbit C is measured from the frequency of the accelerating RF field and the harmonic number for a 20 GeV positron beam. One can write,

$$\beta_{e^+}\,c \;=\; C\,f_{e^+} \tag{3.2}$$

where f_{e^+} is the revolution frequency for positrons in central orbit. f_{e^+} is related to the frequency of the accelerating RF field by a harmonic number h_{e^+} as

$$f_{e^+}^{RF} \;=\; h_{e^+}\,f_{e^+} \tag{3.3}$$

Positrons at 20 GeV are ultra-relativistic, $\beta_{e^+} \sim 1$. The orbit length C is determined with a relative precision of 10^{-8}.

20 GeV protons are injected in the LEP ring and similar measurements are performed using the same magnetic settings as of LEP operation. Protons are not ultra-relativistic at 20 GeV.

The velocity of protons in the central orbit is given by

$$\begin{aligned} v_p = \beta_p c &= C\,f_p \\ &= \frac{C\,f_p^{RF}}{h_p} \end{aligned} \tag{3.4}$$

where h_p is the harmonic number for proton and f_p^{RF} is the corresponding RF frequency. β_p of proton can be determined from equations (3.2) and (3.4)

$$\beta_p \;=\; \frac{h_e\,f_p^{RF}}{h_p\,f_{e^+}^{RF}} \tag{3.5}$$

This gives a measurement of the proton momentum. At 20 GeV, momentum is measured with a precision of $\frac{\Delta p}{p} \sim 10^{-4}$ [25]. This measurement is extrapolated to measure the energies near 45 GeV using flux loop measurements. This leads to a degradation of precision to 2×10^{-4} .

3.2.4 Resonant Depolarisation

The LEP beam energy is measured accurately using resonant depolarisation method. Electrons and positrons circulating in the LEP ring get transversely polarised. The synchrotron radiation causes the transition of electrons and positrons to lower energy states. The spins of electrons and positrons may flip in this process with respect to the dipole magnetic field. The probability of spin flip transition from parallel state to anti-parallel state for electrons is slightly larger than that from anti-parallel to parallel state. The converse is true for positrons. As a result of the asymmetry in spin flip transitions, a transverse polarisation is developed.

The transversely polarised electrons and positrons precess about the vertical magnetic field due to dipole magnets. The beam energy is proportional to the spin tune, ν_s, which is the number of spin precession during one turn around the ring and can be written as,

$$\nu_s = a_e\gamma = \frac{g_e-2}{2}\frac{\mathrm{E_{beam}}}{\mathrm{m}_e\mathrm{c}^2} \tag{3.6}$$

Here $a_e = \frac{g_e-2}{2}$ is the anomalous magnetic moment for electron and m_e is the electron mass. The spin tune and hence the beam energy is measured by depolarisation technique.

The depolarisation is produced in a controlled way by exciting the vertically polarised beam with an oscillating magnetic field perpendicular to the direction of the beam. In the presence of such a weak field, the spins are slightly rotated away from the vertical axis. When the frequency of the field is in phase with the spin precession, the electron spins are coherently swept away from the vertical direction and polarisation disappears. The ratio of the frequency of the depolarising field to the revolution frequency is related to the spin tune through a positive integer :

$$\begin{aligned} \mathrm{f_{dep}} &= \nu_s \mathrm{f_{rev}} \\ &= (\mathrm{N_s} + \delta\nu_s)\mathrm{f_{rev}} \end{aligned} \tag{3.7}$$

The integer part of spin tune $\mathrm{N_s}$ is precisely known from other calibrations.

This technique measures the beam energy under the condition very close to that of the data taking and is so far the most precise method for beam energy measurement. The precision of this measurement is $\frac{\Delta \mathrm{E}}{\mathrm{E}} \sim 1.5 \times 10^{-5}$ [28, 29].

3.3 Systematic Effects to Energy Calibration

Four different methods of energy calibration in LEP allow the possibility of cross check among them. The resonant depolarisation technique is the most precise one. However, this measurement takes some time and cannot be done during the physics operation. Calibration results are extrapolated over the full period of running of LEP. So it is necessary to take into account all possible ways by which energy may change during the time interval between the calibrations. There are two types of effects which cause the change in the beam energy, variation in the magnetic field and change of length of the central orbit. Different sources causing these effects are discussed here.

- Dehydration Effect

  The core of the reference magnet is made of steel whereas the cores of the dipole magnets in the LEP ring are filled with concrete-steel. Due to the dehydration the cores of the dipole magnets shrink which affects the response of the flux loop measurement and as a result the field measured in the ring dipole magnets becomes different from the field measured in the reference magnet.

- Temperature Effect

The flux loop measurement has a dependence on temperature due to the temperature coefficient of the magnetic field. The temperature of the dipoles are measured with thermometers distributed in different positions in the ring. The temperature coefficient is measured from a set of reference magnets in the laboratory and the flux loop measurements performed at different temperatures. The accuracy of the temperature measurement is 0.1 °C which corresponds to a relative change in energy given by [24, 27]

$$\frac{\Delta E}{E} = (1.00 \pm 0.25) \times 10^{-4}/^{\circ}C$$

- Orbit Length Effect

The particles circulating in a stable orbit of the LEP tunnel are synchronous to the frequency of the accelerating RF field. Due to ground motion, the position of the magnets changes with time and hence the circumference of the ring changes. This forces the particles to move in the non ideal orbits and get extra deflections from quadrupole magnets leading to a time dependent change in energy [26, 27].

$$\frac{\Delta E(t)}{E} = -\frac{1}{\alpha}\frac{\Delta C(t)}{C} \tag{3.8}$$

where C is the length of the central orbit and E is the energy of the particles in the central orbit. α is the momentum compaction factor which relates the change in the orbit length to the beam energy. The measured value of α is 1.86×10^{-4} [29] at LEP. Tiny changes of the circumference results in 4 orders of magnitude change in energy.

- Tidal Effect

The gravitational attraction force from the sun and the moon is not uniform over the surface of earth due to its $1/r^2$ dependence. In these regions of earth the gravitational force and the centrifugal force are not in equilibrium which results in a small elastic deformation in earth's body producing two daily tide bulges depending on the relative position of the earth to sun and moon. This, along with the local gravitational stress of the earth, produces a change of 1 mm in the 26.7 km LEP circumference. The time dependent gravity variation $\Delta g(t)$ is related with the change in LEP beam energy [26] by,

$$\frac{\Delta E(t)}{E} = -\frac{1}{\alpha}\frac{\Delta C(t)}{C} = \kappa_{\mathrm{tide}}\,\Delta g(t) \tag{3.9}$$

- Beam Offset Effect

LEP has been operating in the bunch train mode from 1995. In this mode of operation, vertical dispersion of the beam causes a shift in the centre of mass energy. Vertical dispersions are produced due to the effect of the electrostatic separators which are used to avoid unwanted collisions. The dispersion is a periodic function of the orbit length. Particles moving in non central orbit have energy difference ΔE to the nominal energy E will have a displacement given by

$$\Delta u(s) = D(s)\ \frac{\Delta E}{E}$$

The coordinate u can be either horizontal (x) or vertical (y) with respect to the beam plane. If the displacements for electron and positron beams are different at the interaction point in the vertical plane, the shift in the centre of mass energy is given by,

$$\Delta E_{cm} = -\frac{1}{2}\frac{\Delta y}{\sigma_y^2}\frac{\sigma_E^2}{E}\,\Delta D_y \qquad (3.10)$$

where δy is the collision offset, ΔD_y the vertical dispersion difference between the beams, E and σ_E are the beam energy and the energy spread. This effect is illustrated in figure 3.3 and it causes the centre of mass energy to shift by several MeV at the interaction point [32].

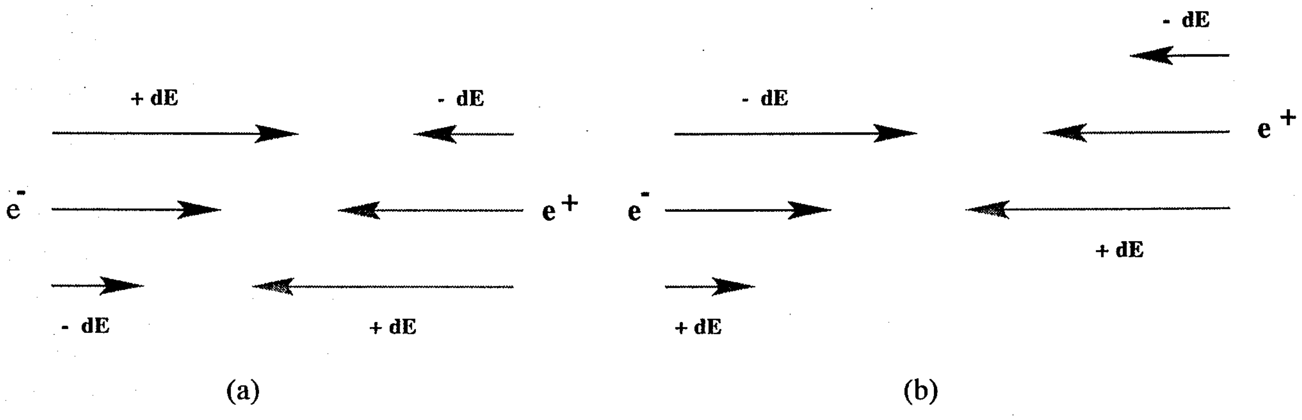

Figure 3.3: Schematic view of the collision of two bunches with opposite sign vertical dispersion. (a) No offset, (b) with vertical offset

- Train Effect

The dipole field in the LEP tunnel gets affected due to the current created by the DC powered trains travelling between Geneva and France passing near IP1 of LEP. This parasitic current leaks into earth and returns to power stations through the vacuum chamber of the LEP tunnel entering near IP1 and leaving between IP5 and IP7. This current interacts with the magnetic dipole field, hence changing the field B. This effect was observed by the NMR probes. The measured variation of the magnetic field causes an increase of up to 12 MeV in the beam energy [33].

3.4 Beam Energy Spread

Electrons and positrons circulating in the LEP ring perform oscillations in energy and azimuthal position with respect to the *synchronous* orbit. The particles suffer random energy losses at random times along their trajectory due to the synchrotron radiation. This results in a damping of the energy oscillations. Average of this type of motion over a large number of particles gives the equilibrium energy distribution of these particles. This is constant in time and is Gaussian in shape. The r.m.s of this energy distribution is referred to as the *beam energy spread* and its value is ≈ 55 MeV.

The energy spread (σ_{E}) in the beam is directly related with the bunch length (σ_{Z}) given by [30],

$$\sigma_{\mathrm{E}} = \frac{\mathrm{E_b}}{\alpha\,\mathrm{r}} \mathrm{Q_s}\, \sigma_{\mathrm{Z}} \tag{3.11}$$

where r is the bending radius, α is the momentum compaction factor and $\mathrm{Q_s}$ is the synchrotron tune.

The measured cross section and asymmetries which are functions of the centre of mass energy, need to be corrected for this energy spread. The error in the measurement of beam energy spread arises from different sources like bunch length measurement and from uncertainties of the synchrotron tunes and the finite dispersion at the interaction point. Its value is $\simeq 2$ MeV.

Chapter 4

The L3 Experiment

The L3 detector is one of the four detectors at the Large Electron Positron Collider at CERN to study the physics from the e^+e^- interactions. The L3 detector is located at the second interaction point (IP2) of the LEP ring, approximately 50 m underground. Figure 4.1 shows the perspective view of the detector. The detector is 14 m long and

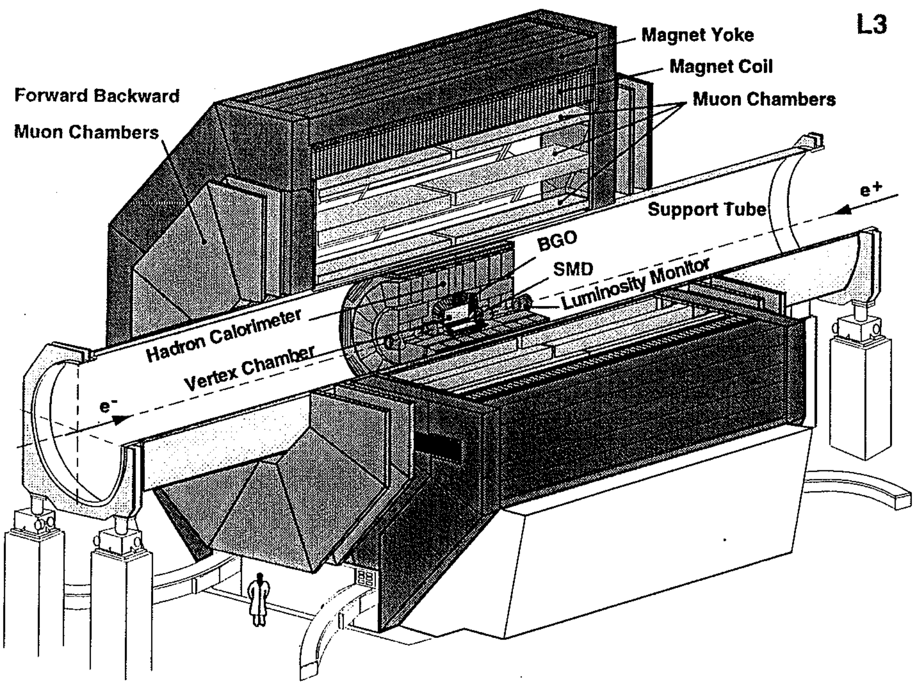

Figure 4.1: A perspective view of the L3 detector

16 m in diameter. The entire detector is placed inside a solenoidal magnet producing a uniform field of 0.5 T along the beam direction. The detector [18] consists of the following sub-detector components arranged in layers.

- Central tracking system

  - time expansion chamber (TEC) for the measurement of momenta, charge of particles and the determination of the interaction vertex,
  - silicon micro-vertex detector (SMD) in order to improve momentum resolution of tracks and for reconstruction of vertices,
  - central Z chamber for the measurement of z coordinates of tracks.

- Electromagnetic calorimeter
  - barrel and endcap electromagnetic calorimeter made of Bismuth Germanate (BGO) crystals for the measurement of energy and direction of electrons and photons,
  - instrumented (active) lead ring (ALR) for measurement of energy of electrons and photons at the small angles and to trigger two photon processes,
  - electromagnetic gap detector (EGAP) filling the gap between barrel and endcap electromagnetic calorimeter.

- Cylindrical array of scintillation counters for accurate measurement of event time.

- Hadron calorimeter
  - barrel and endcap hadron calorimeters (HCAL) made of proportional counters with uranium as absorber, used to measure the energy of hadronic jets,
  - active muon filter used for energy and coordinate measurement of hadrons.

- Muon spectrometer made of multi-wire drift chambers, to measure the momenta of muons.

- Luminosity Monitor (LUMI) to measure the luminosity using small angle Bhabha events.

- Solenoidal and toroidal magnets.

The following sub-detectors: central tracking system, electromagnetic and hadron calorimeters, scintillation counters and the luminosity monitors are mounted inside a 32 m long and 4.5 m diameter steel support tube which is coaxial to the beam pipe. The barrel and the forward backward muon chambers are mounted outside the support tube.

A right handed coordinate system is used to describe the detector. The origin is same as the geometrical centre of the detector which is also the nominal event vertex. The z axis is along the direction of e^- beam, y axis points vertically upwards and x axis points towards the centre of the LEP ring.

4.1 Central Tracking System

The central tracking system consists of a time expansion chamber, the Z chambers and a silicon micro-vertex detector. Figure 4.2 shows the perspective view of the central tracking detector.

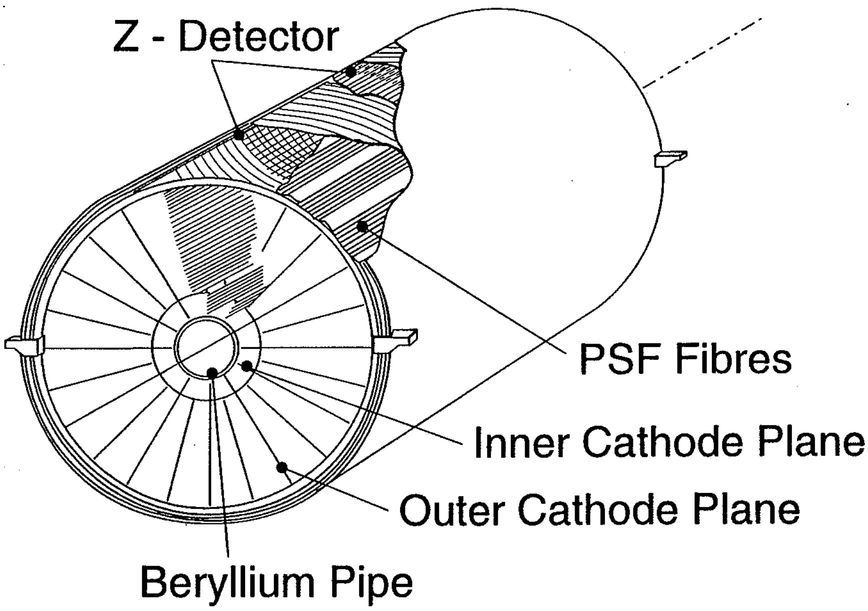

Figure 4.2: Perspective view of the tracking chamber

4.1.1 The Time Expansion Chamber (TEC)

The Time Expansion Chamber (TEC) consists of two concentric cylindrical drift chambers with common end plates, operated in the *time expansion mode* [36, 37]. The principle of TEC is demonstrated in figure 4.3. The drift area is subdivided into two regions with different electric field. A large volume with low but homogeneous field is called the drift region and a small volume with high field where the gas amplification takes place is called the amplification region. These two regions are separated by a grid plane which ensures the homogeneity of the field in the drift region. The TEC operates with a gas mixture of 80% of CO_2 and 20% C_4H_{10} at a pressure of 1.2 bar and temperature of 18°C. The drift velocity of electrons is $6\,\mu$m/ns.

The angular coverage of TEC is $42° < \theta < 138°$ and the radial length available to measure tracks is 31.7 cm. The wires are aligned parallel to the beam direction. The inner chamber of TEC is subdivided in 12 ϕ sectors whereas the outer chamber is subdivided in

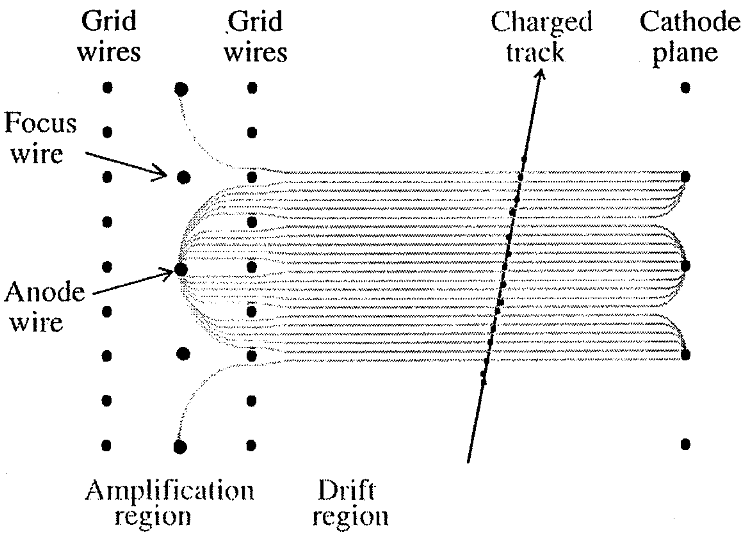

Figure 4.3: The principle of the Time Expansion Chamber

24 ϕ sectors. The sectors are separated from each other by cathode planes and the anode plane is at the middle of each sector. Each inner sector of TEC has 8 anode wires while each outer sectors has 54 anode wires. Hence a maximum of 62 coordinate measurements are possible for a single track. Figure 4.4 shows one such inner sector with two outer sectors. The sectors are symmetric with respect to the cathode plane which causes the left-right ambiguity. Groups of five grid wires on each side of the amplification region (pick-up wires) are read out. The induced signals on both sides are compared to solve this ambiguity.

Each outer segments of TEC on its outer surface is wrapped with plastic scintillating fibre (PSF) ribbon to monitor the drift velocity. Each ribbon consists of 143 fibres aligned parallel to the beam direction. The drift velocity is measured by plotting the average drift time for each anode wire versus the PSF position.

The resolution in coordinate measurement in the $r - \phi$ plane is $50\,\mu$m. This leads to a resolution of the measurement of transverse momentum of $\frac{\Delta p_t}{p_t^2} = 0.02$ GeV^{-1}.

4.1.2 The Z chamber

The z coordinate of tracks are measured using the Z chamber which covers the outer cylinder of TEC. The Z chamber consists of two concentric cylindrical proportional chambers with cathode strip readout. The Z chamber operates with 80% of argon and 20% of CO_2

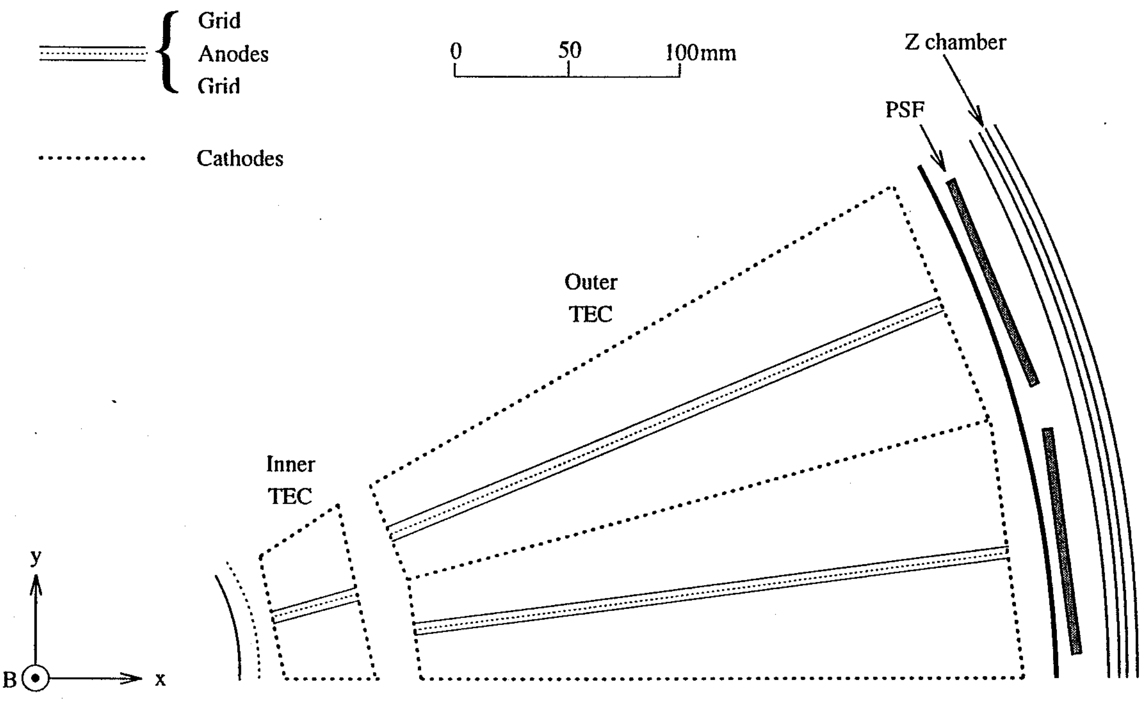

Figure 4.4: Geometry of TEC sectors

gas mixture. The effective length of Z chamber is 1068 mm, with outer diameter of 980 mm and thickness of 21.5 mm. The Z chamber has the angular coverage of $45° < \theta < 135°$. Signals are read out from a total of 920 cathode strips. The cathode strips of the inner chamber are inclined at 69° and 90° and the cathode strips of the outer chambers are inclined at −69° and 90° with respect to the beam direction. The resolution achieved by the Z detector is 320 μm.

4.1.3 Silicon Micro-vertex Detector (SMD)

The innermost component in the L3 detector is the silicon micro-vertex [38] detector, situated just outside the beam-pipe of radius 5.5 cm surrounding the interaction region.

SMD is 35.5 cm long and covers the angular range of $22° < \theta < 158°$. It consists of two radial layers of double sided silicon strip detectors in the form of ladders shown in figure 4.5. The layers have radii of 6 cm and 8 cm respectively. There are a total of 24 ladders. Each ladder consists of two half ladders. Each half ladder, in turn, consists of rectangular ($70 \times 40\,\mathrm{mm}^2$) double-sided high purity n type silicon strip sensors of thickness 300 μm. The active area of the sensor strips is $70 \times 38.3\ \mathrm{mm}^2$. In order to resolve a single track from ambiguities the ladders in two layers have a stereo rotation of 3° with respect to each other on the axis perpendicular to the ladder plane as shown in figure 4.6.

The outer silicon surface of each ladder is read out at 50 μm intervals for $r - \phi$ coor-

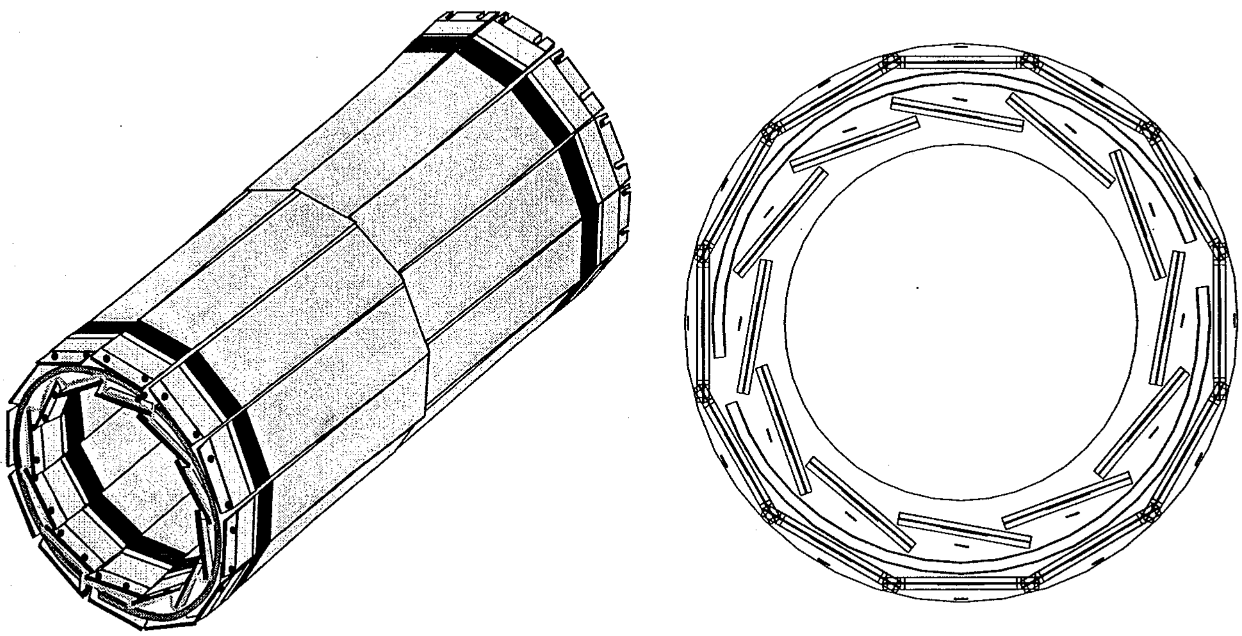

Figure 4.5: Perspective and cross-sectional views of the L3 silicon micro-vertex detector

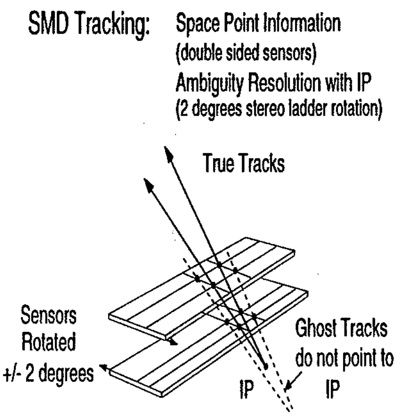

Figure 4.6: Relative stereo rotation of SMD ladders

dinate measurements. The inner surface is readout at 150 μm (central region) or 200 μm (forward) intervals for z coordinate measurements. The total number of readout channels is $\sim$ 73000. The design resolutions of the SMD are 0.3 mrad in ϕ, and 1 mrad in θ.

The SMD is designed to improve the tracking capabilities of the central tracking detector. This permits the measurements of secondary vertices, enhancing the b-tagging efficiency, transverse momentum resolution and jet identification capabilities.

4.2 Electromagnetic Calorimeter (ECAL)

The electromagnetic calorimeter in L3 detector is a homogeneous calorimeter for measuring the energy of electrons and photons through total absorption. It is made of Bismuth Germanate or BGO crystals having fantastic energy and spatial resolution for electrons and photons over a wide a range of energy (from 100 MeV to 100 GeV). The attractive properties of the BGO crystals are the following,

- small radiation length of 1.12 cm for electrons and photons which allows the detector to be compact,
- large nuclear absorption length (21.9 cm) makes it possible to efficiently distinguish electromagnetic particles from hadronic ones. The hadron to electron rejection ratio is 1000:1,
- the crystals are nonhygroscopic and radiation hard in nature,
- BGO has a reasonable light yield

The individual crystals are 24 cm long and trapezoidal in shape. The area of the front face of each crystal is 2×2 cm^2 and that at the back face is 2.6×2.6 cm^2 to 2.9×2.9 cm^2. Each crystal is mounted in a carbon fibre support structure. The scintillation light from each crystals is detected through two silicon photodiodes glued to its rear end. Figure 4.7 shows one such crystal. The calorimeter consists of a total of about 11000 crystals and is divided into a barrel and two endcap regions (figure 4.8). The crystals are positioned in such a way that in θ they are pointing towards the interaction point whereas in ϕ they are tilted by 0.6°. This arrangement reduces the possibility of leakage through the inactive material between crystals. The barrel region consists of 7860 crystals arranged in two cylindrical half barrels with total polar angular coverage of $42.3° < \theta < 137.7°$. Each half barrels consists of 24 rings of 160 crystals. Each endcap calorimeter consists of 1527 crystals. The endcap calorimeters cover the polar angular regions of $11.6° < \theta < 38°$. $142° < \theta < 168.4°$. The barrel calorimeter was calibrated in test beams using electrons of energies 0.18, 2, 10, and 50 GeV. The energy resolution from these measurements is 5% at 100 MeV, less than 2% above 2 GeV and about 1.2% at 45 GeV [18]. The

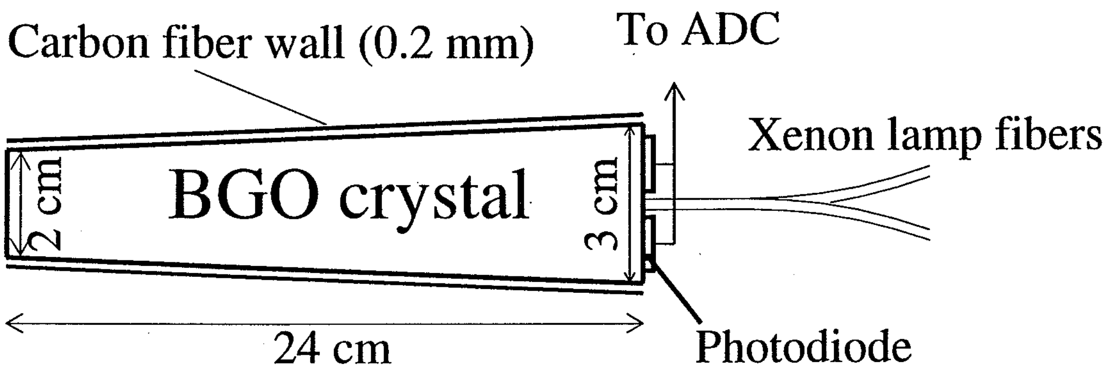

Figure 4.7: Mounting of a BGO crystal

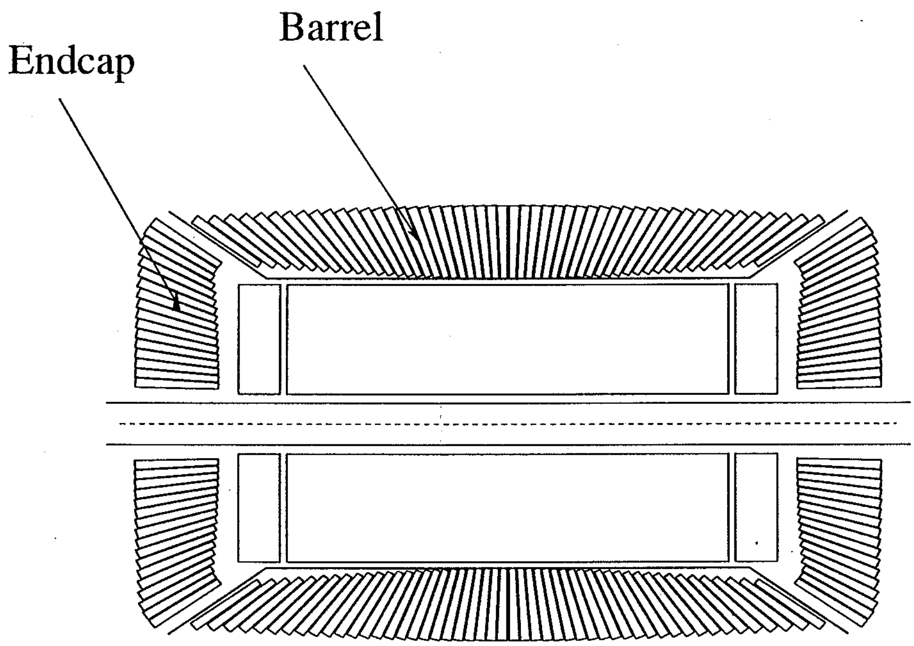

Figure 4.8: Side view of the L3 Electromagnetic calorimeter

resolution in BGO as obtained in the test beam studies is shown in figure 4.9. The

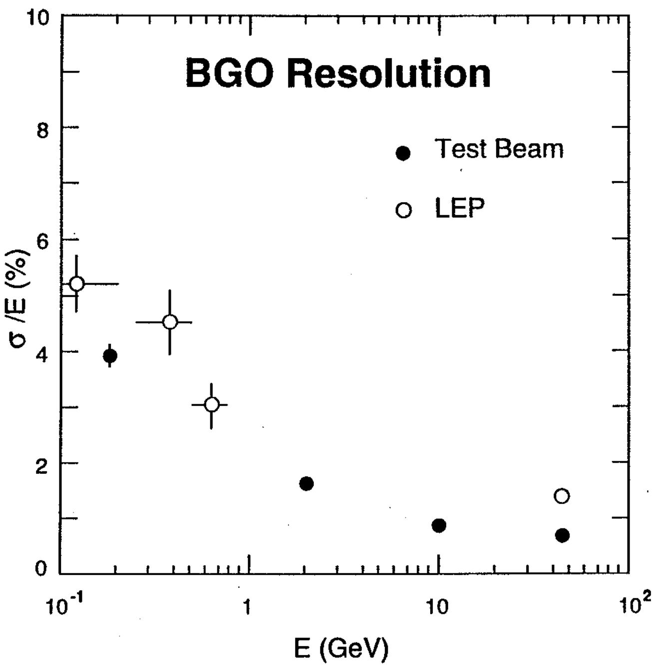

Figure 4.9: Energy resolution of the electromagnetic calorimeter

linearity is better than 1%. The position resolution determined by the center of gravity method is $\sim$ 1 mm for electromagnetic showers. The detector is continuously monitored to maintain the energy calibration obtained in the test beam run. For that purpose a Xenon light monitoring system has been installed. The Xenon light system injects light pulses into the rear face of each crystal to measure the crystal transparency [39]. The absolute energy calibration is done with Bhabha ($e^+e^- \rightarrow e^+e^-$) events around Z^0 peak. The minimum ionising signal of cosmic muons is utilised to perform energy calibration at lower energies [40].

4.2.1 The Active Lead Ring (ALR)

The active lead ring is situated between the electromagnetic calorimeter endcaps and the luminosity monitors. It covers the angular regions of $4.5^\circ < \theta < 8.8^\circ, 171.2^\circ < \theta < 175.5^\circ$ and is located at 108.0 cm $< |z| <$ 118.4 cm. ALR consists of three layers of plastic scintillator plates of thickness 10 mm sandwiched between 18.5 mm thick lead blocks. The scintillator plates are divided into 16 sectors in the $r - \phi$ plane and are individually read out by photodiodes. Successive layers are rotated by one third of a segment. ϕ coordinates are measured with a resolution of $\approx 1.3^\circ$. ALR is used to improve the efficiency to trigger the two photon processes with extended polar angle coverage.

4.2.2 The Gap Detector (EGAP)

The gap of 7.4 cm between the electromagnetic calorimeter barrel and endcaps has been filled with the gap detector (EGAP) during the 1995-1996 shutdown period. It consists of lead blocks instrumented with plastic scintillator fibres. The purpose is to improve the total energy resolution.

4.3 The Scintillation Counter

The scintillation counter system is placed between the electromagnetic and hadron calorimeters. The scintillation counters are designed for the precise measurement of relative timing of particles traversing the detector with respect to the beam crossing time. The barrel scintillation counter system consists of 30 strips each 290 cm long, covering the angular range of $34° < \theta < 146°$ and 93% of ϕ. Each strip is a 1 cm thick plastic scintillator read out on both sides by photomultipliers. They measure the time difference between the beam crossing and the signal received by them. The resolution of the counter is 460 ps determined using muon pairs and is shown in figure 4.10.

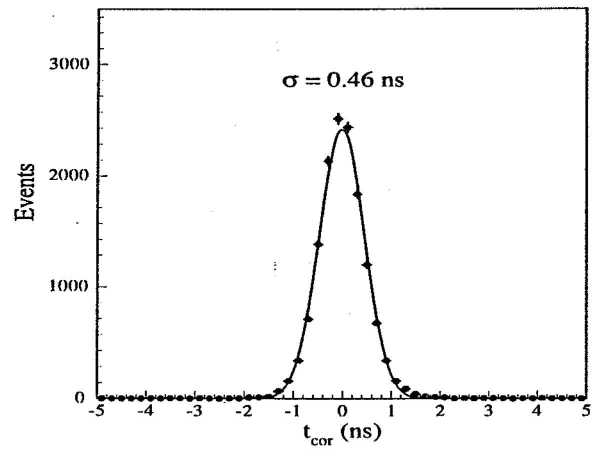

Figure 4.10: Time resolution of scintillation counters

At the beginning of 1995 two endcap disks of 16 scintillator sectors with wavelength shifting fibre read-out were added at $|z| = 103$ cm for the forward backward muon chambers.

The main purpose of the scintillation counter system is to discriminate between the dimuon events originating from Z^0 decays and the cosmic muons passing near the interaction point. The timing of the cosmic muons is uncorrelated with the beam crossing time and the time of flight is about 5.8 ns in opposite scintillation counters whereas for dimuon events the two opposite scintillators register pulses with almost zero time difference.

4.4 The Hadron Calorimeter (HCAL)

The hadron calorimeter [41] is a fine grained sampling calorimeter made of uranium absorber interspersed with brass tube proportional counters and is operated with 80% Ar and 20% CO_2 which act as the active medium. Due to very short nuclear absorption length of uranium, the calorimeter allows only non-showering particles to reach the muon chamber. HCAL consists of three parts: barrel, endcap and muon filter as shown in figure 4.11.

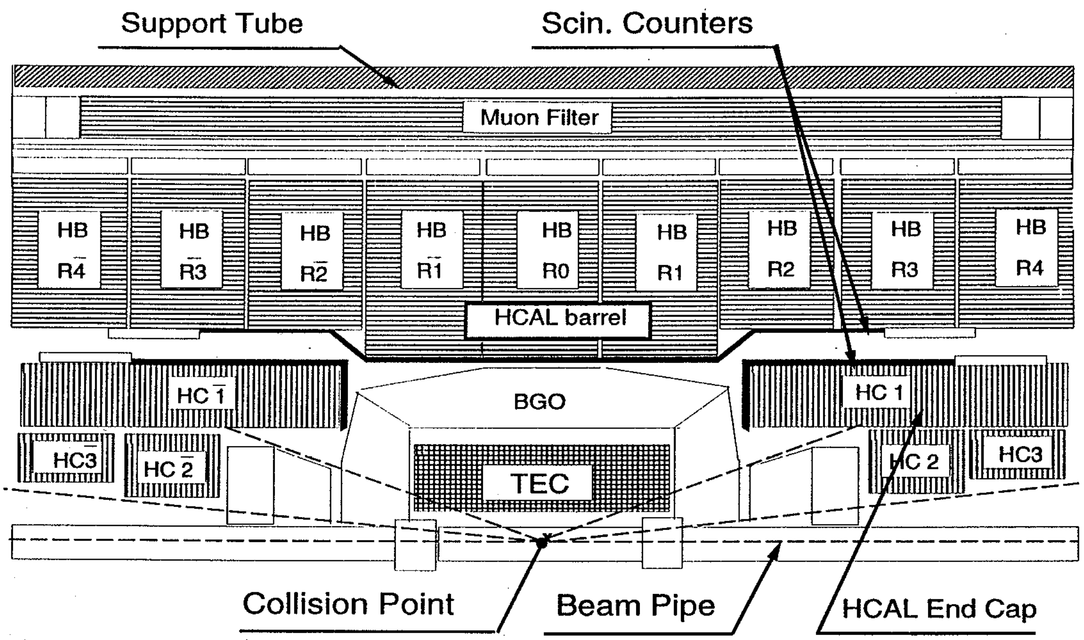

Figure 4.11: A longitudinal view of L3 detector showing the hadron calorimeter barrel and end caps

4.4.1 HCAL Barrel

The barrel hadron calorimeter covers the angular range of $35° < \theta < 145°$. It consists of 9 rings along the z direction. The hadron calorimeter barrel is 4.725 m long, has an outer radius of 1.795 m. The inner radius for the three central rings is 0.885 m and that for the outer rings is 0.979 m. Each ring is divided symmetrically into 16 modules in ϕ. Each module contains proportional wire chambers (PWC) interleaved with 5 mm uranium plates. Modules of the three central rings contain 60 chambers whereas the six outer rings contain 53 chambers. The anode wires in adjacent PWC planes are oriented at right angles and point alternately in z and ϕ directions. The signal wires from each module are grouped in towers which include wires from alternate layers. A total of $\sim$ 22 K towers are formed. The pattern of wire grouping provides 10 towers (8 for short modules) radially and 9 in z or ϕ direction. Each tower typically covers an angular range of $\Delta\theta = 2°$ and $\Delta\phi = 2°$.

4.4.2 HCAL Endcaps

The endcap hadron calorimeter consists of three separate rings, one outer ring HC1 and two inner rings HC2 and HC3. Each ring is split vertically in half rings, resulting in a total of 12 modules for the whole endcap detectors. The endcaps cover the angular regions of $5.5° < \theta < 35°$ and $145° < \theta < 174.5°$ over the full azimuthal angular range of $0° < \phi < 360°$. The endcaps are also constructed with alternate layers of uranium plate absorber and brass tube proportional chambers. The thickness of the uranium plates are 10 mm (in the front part of the outer rings it is 5 mm). The anode wires are stretched in the azimuthal direction and measure θ directly. There are 77, 27 and 23 layers of chambers in HC1, HC2 and HC3 modules respectively. One layer consists of 8 chambers each covering an angular range of $\Delta\phi = 45°$. The chambers of two consecutive layers are rotated by $\Delta\phi = 22.5°$ to ensure the full coverage in the ϕ angle. As in the barrel the wires are grouped to form a total of $\sim$ 4 K towers each covering an angular range of $\Delta\theta = 1°$.

4.4.3 Muon Filter

The muon filter [42] is situated outside the HCAL barrel and inside the support tube. There are eight octants, each 4 m long, 1.4 m wide and 0.2 m thick. Each octant is made of 6 alternate layers of 1 cm thick brass absorber plates with five layers of proportional chambers. The muon filter increases the absorption length of the hadron calorimeter by 1.03.

Combining the information from electromagnetic and hadron calorimeter the energy resolution obtained for hadronic jets is $\frac{\Delta E}{E} = \frac{55\%}{\sqrt{E}} \oplus 5\%$ and the jet axis can be determined with a resolution of 2.5°.

4.5 The Muon Chamber System

The muon chamber system (MUCH) [43] consists of barrel and forward backward muon chambers. The barrel muon chambers sample the muon tracks in the bending as well as in the non-bending plane with the use of momentum measuring (P) chambers and Z measuring chambers. The muon system has been designed for the measurement of the momenta of muons in the barrel region with an accuracy of $\frac{\Delta p}{p} = 2.5\%$ at 50 GeV.

4.5.1 The P Chambers

The barrel muon chamber is positioned between the support tube and the magnetic coil and consists of two ferris wheels (at +z and −z). Each wheel contains 8 octants, each of which consists of 5 precision (P) drift chambers distributed in 3 layers as shown in

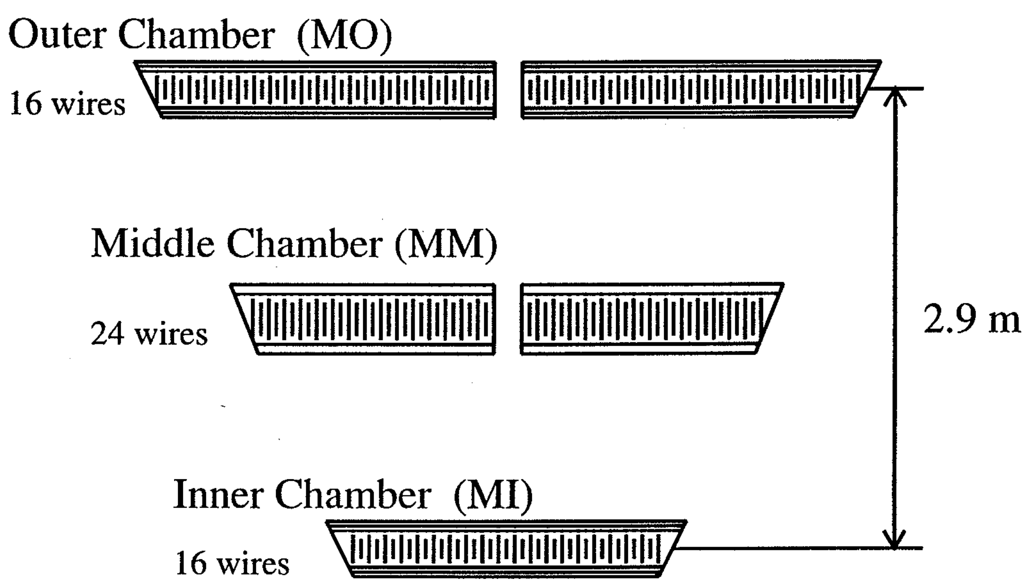

Figure 4.12: An octant of the muon spectrometer

figure 4.12. In the inner layer (MI) there is one chamber while the middle (MM) and outer (MO) layers contain two chambers each. Each P chamber consists of about 320 signal wires. These chambers measure very precisely the track coordinates in the $r - \phi$ plane. The muon momentum is then determined from the *sagitta* (s), the deviation of the track from a straight line due to the magnetic field as shown in figure 4.13. The resolution of the muon momentum can be expressed as

$$\frac{\Delta p}{p} \sim \frac{\Delta s}{s}$$

The sagitta s is given by

$$s \sim \frac{0.3}{8}\frac{BL^2}{p_t}$$

where L (= 2.9 m) is the lever arm available for sagitta measurement, B (= 0.5 T) is the magnetic field and p_t is the transverse momentum of the muon. For a 45 GeV muon,

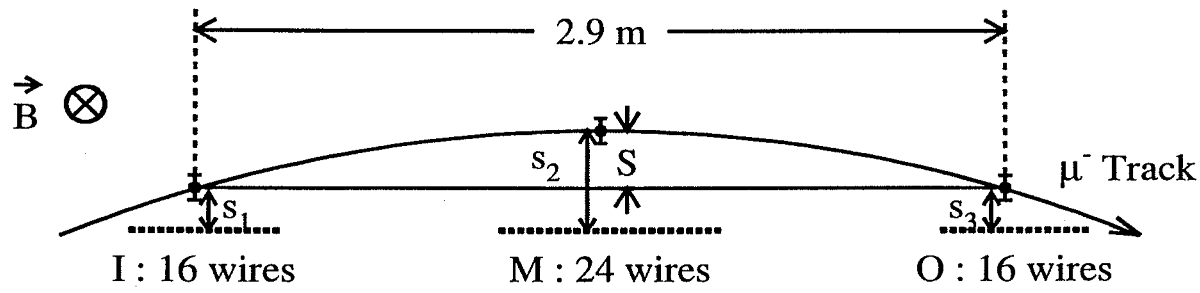

Figure 4.13: Momentum measurement of muons with sagitta method

sagitta is expected to be 3.4 mm. This is measured with an accuracy of $\Delta s \sim 70\,\mu m$ resulting in 2% resolution in the momentum measurement.

4.5.2 The Z chamber

All octants are equipped with additional drift chambers, called Z chambers, to measure the coordinate along the z direction. There are six Z chambers per module of dimension 6×2 m^2, covering the top and bottom of the MI and MO chambers. Each Z chamber consists of two layers of drift cells offset by one half cell with respect to each other, to resolve the left-right ambiguities. The position resolution obtained in the z chambers is $500\,\mu$m.

The central part of the muon chamber covers the angular range of $43° < \theta < 137°$.

4.5.3 Forward Backward Muon Chamber

The forward backward muon chambers [44] are mounted on the magnet doors on either side of the interaction point (figure 4.14). On each side there are three layers and each of them consists of 16 drift chambers. The forward backward system covers the angular region of $22° < \theta < 43°$ and $137° < \theta < 158°$. In the angular range of $36° < \theta < 43°$ the muon momentum is measured from 2 central (MI, MM) and 1 inner FB chambers using the curvature in the solenoidal magnetic field. The momentum resolution degrades with θ from 2–20%. Muon momentum in the angular range of $22° < \theta < 36°$ is measured using curvature in the toroidal magnetic field in three layers of FB muon chambers. The momentum resolution in this case is 20% for momentum less than 100 GeV, and it is dominated by the multiple scattering in the 1 m thick doors of the magnet.

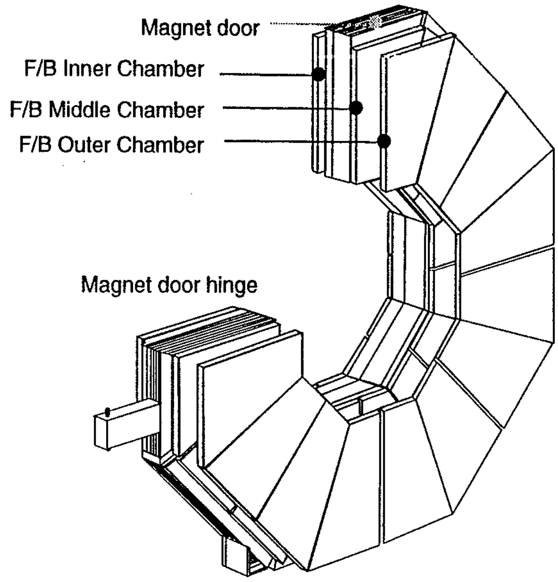

Figure 4.14: Forward backward muon chamber

4.6 Luminosity Monitor

The system to measure the luminosity at the L3 interaction point consists of two detectors installed symmetrically on either side of the interaction point at distances of $|z| = 2.65$ to 2.80 m. The luminosity monitor has been designed to detect events from very small angle (31−62 mrad from the z axis) Bhabha scattering $e^+e^- \to e^+e^-$. Each detector is divided into two mirror symmetric halves with respect of the beam axis. Each detector consists of a calorimeter subsystem and a tracking subsystem. Figure 4.15 shows the luminosity monitor on one side of the interaction point along with the other L3 detector components.

4.6.1 Calorimetric Luminosity Monitor (LUMI)

Each calorimetric subsystem consists of an array of 304 Bismuth Germanate (BGO) crystals. The crystals are arranged in eight cylindrically symmetric concentric rings extending radially from 6.8 to 19.0 cm. The polar angular coverage is 25 mrad $< \theta <$ 70 mrad. The rings cover the full ϕ angle in azimuth and is divided in 16 sectors. The energy resolution in the calorimeter is 2% at 45 GeV.

4.6.2 Silicon Luminosity Monitor (SLUM)

Two silicon detectors are placed in front of each of the crystal arrays for better determination of the angular acceptance and precise determination of the point where the particle enters the calorimeter. This improves the luminosity measurement defining the event ge-

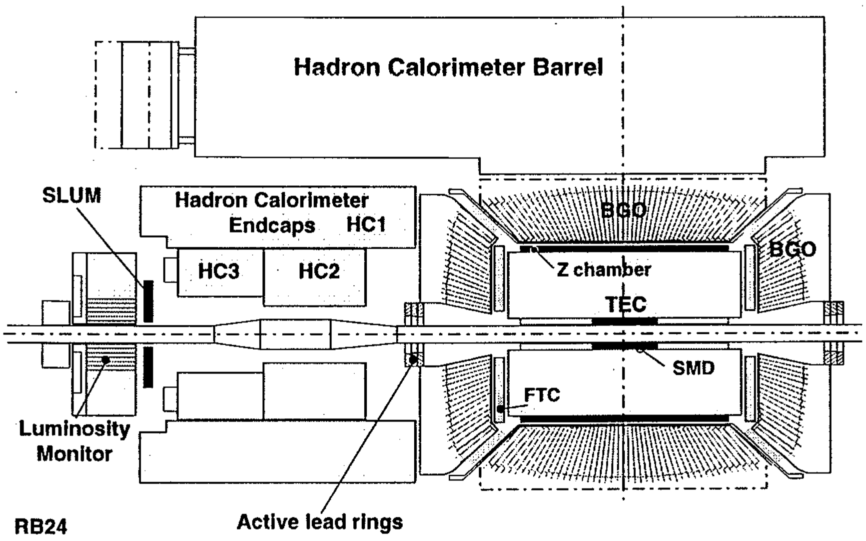

Figure 4.15: Side view of the L3 detector with the luminosity monitor

ometry very precisely. Each of the trackers consists of three layers of silicon wafers, two for r measurement and one for ϕ measurement.

4.7 Magnet

A huge solenoidal magnet is used in the L3 detector for charge and momentum measurement in the tracking chamber and in the muon spectrometer. The solenoid carries a current of 30 kA producing a uniform magnetic field of 0.5 T along the z direction. The coil is made of welded aluminium plates and has inner radius of 5.93 m and length of 11.9 m. The return yoke is made of soft iron and the outer radius of the whole system is 7.9 m. All the sub-detector components are installed inside the magnet. The solenoid is cooled by water flow system to protect the sub-detectors from the heat generated.

At a later stage 1.5 T toroidal magnets were added to the main magnet door for the forward backward muon chamber system.

4.8 Trigger System in L3

The bunch crossing rate at LEP is 45 kHz (in 4×4 mode) but most of them do not result in an e^+e^- interaction. The rate at which Z^0 events are produced is about 1 Hz. The trigger system decides whether an event should be recorded or not after each bunch crossing. The trigger system in L3 consists of three different levels with increasing complexity. The event rate is reduced at each level and finally the data is recorded in tapes at a rate of 2–3 Hz. Figure 4.16 shows the various levels of L3 online trigger system schematically. Level 1 trigger selects e^+e^- events together with the backgrounds coming from beam-gas and beam-wall interactions and from electronic noise whereas level 2 and level 3 reject the background and noisy events which pass the level 1 selection criteria. Level 1 trigger is

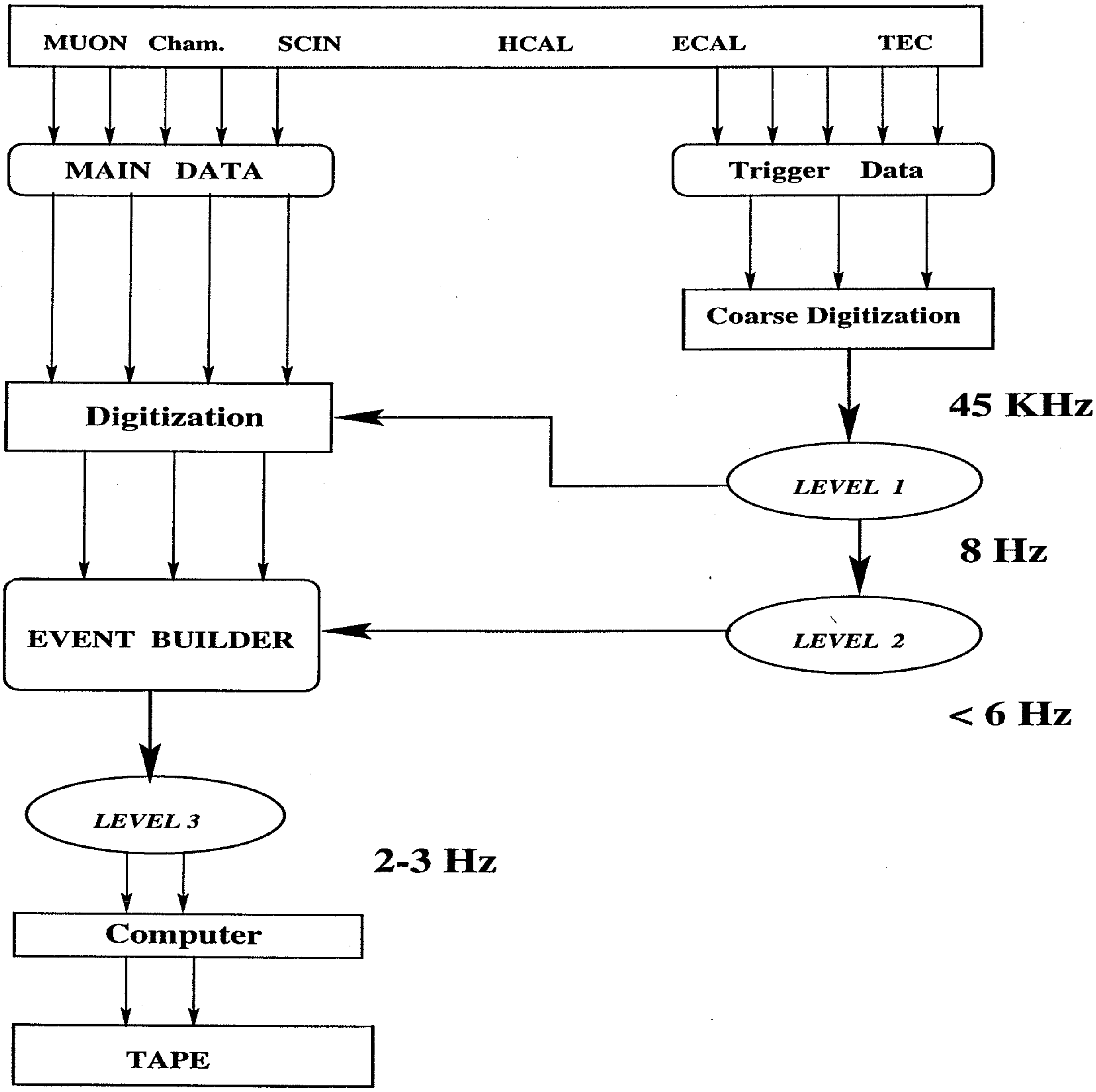

Figure 4.16: Schematic view of the on line trigger system in L3

controlled entirely by hardware using mostly CAMAC modules. These modules include arithmetic logic units (ALU), bus multiplexer (BS), memory look-up table (MLU), data stack (DS), ECL drivers and the fast encoding and readout ADC's. One can, of course, adjust the parameter setting. In the beginning, level 2 used to use XOP's which were replaced at a later stage with VME processors. Level 3 trigger uses RISC processors (VAX stations).

4.8.1 Level 1 Trigger

Level 1 trigger system consists of 5 independent triggers based on calorimetric energy (both electromagnetic and hadronic), TEC, scintillator, muon chamber and luminosity monitor. Each of them takes decision independently within 22 μs before the next beam crossing. On a positive decision of any of the five, the fine digitisation electronics commence operation which takes about 500 μs. This causes a dead time for the data acquisition system. On the other hand in case of a negative decision, all electronics are cleared and the detector becomes ready for the next beam crossing without introducing any dead time.

Energy Trigger

The level 1 energy trigger [45] has been designed to select events which deposit energy in electromagnetic or hadron calorimeters. This includes e^+e^-, $\tau^+\tau^-$, hadronic and $\nu\bar{\nu}\gamma$ final states.

The barrel and endcap BGO crystals are grouped into 32 ϕ $\times$ 16 θ blocks and the hadron calorimeter towers are grouped into 16 ϕ $\times$ 13 θ blocks. Analog signals from a total of 896 channels are digitised by fast ADC's and converted into energy depositions. The event is accepted if any of the following criteria is satisfied,

- the total calorimetric (ECAL + HCAL) energy in barrel and endcaps is greater than 25 GeV,
- the total calorimetric energy only in the barrel exceeds 15 GeV,
- the electromagnetic energy in barrel and endcaps is greater than 25 GeV,
- the electromagnetic energy only in barrel exceeds 8 GeV.

The $\theta - \phi$ projections are also used to search for clusters. The cluster threshold is 6 GeV. For clusters associated with a TEC track the threshold is 2.5 GeV.

The main source of background for this trigger is electronic noise. The typical trigger rate is 1–2 Hz.

TEC Trigger

The TEC trigger is used to select events with charged tracks. It includes most of the physics channels.

Signals from 14 anode wires from each of the 24 outer TEC sectors are used to search for correlated hits forming track. Tracks are required to have a minimum transverse momentum of 150 MeV and the event is accepted if at least two tracks are found with an acolinearity less than 60°. The main source of background for this trigger is cosmic events. The typical trigger rate is 1–4 Hz.

Scintillator Trigger

The scintillator trigger is used for high multiplicity events. Together with muon trigger it rejects the cosmic events. The event is selected if it has more than 5 hits spread over 90°. The typical trigger rate is 0.1 Hz.

Muon Trigger

The events having at least one particle penetrating the muon chamber are selected by muon trigger. The event is required to have a good track having at least hits in 2 P chamber layers and 3 Z chamber layers and a minimum transverse momentum greater than 1 GeV. The trigger rate is 10 Hz and it decreases to 1 Hz when one good scintillator hit is required in coincidence.

Luminosity Trigger

Luminosity trigger is used to select the small angle Bhabha events for luminosity measurement.

Each of the luminosity monitors on both sides are divided into 16 ϕ sectors and signal from all 32 sectors are processed. The event is accepted if one of the following three criteria is satisfied

- two back to back energy depositions of more than 15 GeV each (within $\pm$ 1 sector),
- total energy on one side more than 25 GeV and on the other side more than 5 GeV,
- a total energy on either side more than 30 GeV.

The typical rate of the luminosity trigger is 1.5 Hz.

4.8.2 Level 2 Trigger

Level 2 trigger [46] tries to reject background events coming from beam-gas and beam-wall interactions and from electronic noise which are selected by level 1.

The inputs to level 2 are the coarse data used in level 1, the decision in level 1, and informations of calorimetric energies, loosely reconstructed tracks, scintillator hits and the interaction point. The correlations between the individual sub-detector informations are taken into account here. Level 2 trigger can spend much longer time (8 ms) compared to level 1 and makes improved decision without incurring additional dead time. In case of negative decision in level 2, event builder memories are reset. It becomes operational to those events where only one trigger in level 1 has been satisfied. Events which satisfy more than one trigger in level 1 pass untouched in level 2. Level 2 reduces the trigger rate by 20–30%.

4.8.3 Level 3 Trigger

Level 3 trigger [47] takes the final decision whether the event should be written on tape or not. The selection criteria used by level 3 are based on the complete digitised data of the event from the full detector readout. The digitised data with finer granularity and resolution allow to apply tighter selection criteria. The selection criteria are based on the calibrated calorimetric energies, interaction vertex from matched TEC tracks with the calorimetric clusters and reconstructed muon tracks. The time available to level 3 trigger is 10 times larger than that of level 2. Events with multiple level 1 triggers are passed unhindered through level 3. The trigger rate is 2–3 Hz at this level.

Chapter 5

Simulation and Reconstruction

5.1 Monte Carlo Simulation

Monte Carlo simulation is one of the most important tools in high energy physics experiments. In the design phase of an experiment, simulation is used to optimise the detector geometry. Later on, during the execution phase, simulated events are studied to establish the selection criteria for different physical processes by optimising the efficiency and signal-to-background ratio. Systematic errors on physics results are determined by comparing data with the expectation from Monte Carlo simulation.

Monte Carlo simulation in the L3 experiment is performed in two steps (a) *Event Generation* and (b) *Detector Simulation.*

5.2 Event Generation

Events are generated according to different physics models. Generated events contain description of the particles in the form of particle identification and energy momentum four vectors, vertex information, decay length and also the pointer to the parent particle. These informations are then forwarded to the detector simulation and finally to the event reconstruction programme.

A variety of event generators exist for the study of physics processes relevant for e^+e^- interaction. An event-generator library (EGL3) is formed for the L3 experiment, where the event generators are interfaced to the L3 detector simulation programme SIGEL3. These generators are tested and tuned for the LEP physics.

The event generators which are commonly used for the Z^0 lineshape studies are described below.

- *BHLUMI*

  The event generator BHLUMI [48] simulates the small angle Bhabha scattering $e^+e^- \rightarrow e^+e^-$. This is extensively used for the analysis of the luminosity events at

LEP. The theoretical uncertainty due to uncalculated higher order terms is 0.11%.

- *BABAMC and BHAGENE*

  The large angle scattering of $e^+e^- \to e^+e^-$ events are studied using the generators BABAMC and BHAGENE [49,50]. BABAMC includes first order QED radiative corrections and hence events contain up to one real bremsstrahlung photon. The lowest order electroweak corrections are implemented here. The event generator BHAGENE is capable of simulating up to three bremsstrahlung photons. Complete one loop electroweak corrections are implemented here, including soft photon exponentiation.

- *KORALZ*

  The event generator KORALZ [51] is mainly used for the analysis of the processes $e^+e^- \to \mu^+\mu^-$ and $e^+e^- \to \tau^+\tau^-$. The initial state radiation and the first order QED corrections for final states are implemented here. A complete $\mathcal{O}(\alpha)$ electroweak treatment is implemented. The electroweak library DIZET is used here. The package TAUOLA [52] is used to simulate the process $e^+e^- \to \tau^+\tau^-$. Tau decays into different final states like e, μ, π, ρ, a_1, K, K* are modelled in this package. The effect of τ helicity on decay kinematics is also taken into account.

- *JETSET*

  The JETSET Monte Carlo programme simulates the process $e^+e^- \to q\bar{q}$. This programme is based on parton shower model to describe emission of gluons off the quarks and the subsequent parton cascade originating from gluon splitting and secondary gluon emission. JETSET PS [53] uses *string fragmentation* [54] to model hadronisation. JETSET implements first order initial state corrections and has a detailed library to describe the decays of unstable hadrons.

- *DIAG36*

  The four fermion final state of the two photon interaction in e^+e^- annihilation is described by the generator DIAG36 [55].

- *PYTHIA*

  The event generator PYTHIA [56] is used to generate $e^+e^- \to e^+e^-q\bar{q}$ final states.

5.3 Detector Simulation

The finite resolution of detectors and their limited acceptance distort all observables measured in high energy physics experiments. These effects can be studied by simulating the response of the detector for a given initial state and then reconstructing back the event. The particles are traced through the detector media in steps and different interactions of particles with the detector material, such as pair production, bremsstrahlung, multiple scattering, nuclear interactions are simulated in detail. The effect of magnetic field, finite lifetime of particles are also simulated.

The L3 detector simulation programme SIGEL3 is based on GEANT3 [57], which is a general purpose detector simulation programme. This programme allows to define the detector geometry as well as the properties of the detector materials. The energy loss in the sensitive parts of the detector in each step is recorded. The hadronic interaction is simulated in GEANT3 using the package GHEISHA [58].

The SIGEL3 programme contains a complete representation of the L3 detector including the details of each sub-detector geometry to necessary precision (typically 10$-$100 μm). For example, in hadron calorimeter 426904 brass cells are grouped into $\sim$ 26000 towers which is fully described in the simulation. Similarly in electromagnetic calorimeter 10734 BGO crystals with many different shapes together with the thin-walled carbon fibre structure is described completely.

Simulation of hadronic and electromagnetic showers in complex non uniform media requires tracking of low energy particles down to the sensitivity limit of the detectors. Electrons and photons are tracked down to $\sim$ 100 KeV, muons and charged hadrons down to 1 MeV and neutrons down to 10 KeV.

The detector parameters in the simulation are tuned using test beam results [18]. The important parameters are (a) step size for particle tracking in all sub detectors, (b) medium dependent energy cut off, (c) saturation in light yield, (d) light collection efficiency and electronic noise in the electromagnetic calorimeter and (e) uranium noise in the hadron calorimeter.

Hits in the central tracking chamber and the muon chamber are simulated using the time to distance relation measured in the test beam data. The simulation includes the effects of the multiple hits, cross talks and δ-rays.

ADC and TDC informations of the scintillation counter are also simulated. Pulse heights are corrected for attenuation. Times are corrected for the time-of-flight of particles, light transmission delay in the scintillators, etc.

5.3.1 Detector Imperfections

The detector simulation described above assumes a perfect detector in its model. For measurements with high precision (below 1%), it becomes necessary to take into account the time dependent imperfections of the detector. The deviation of the detector model arises due to various effects like dead or noisy crystals in the electromagnetic calorimeter, defective towers in the hadron calorimeter, disconnected sectors and inefficient wires in

TEC, dead cells in the muon chambers etc.

Informations about the status and calibrations of all the sub-detectors are stored in the L3 database system. At the time of reconstruction, relevant informations are retrieved from the database using time and date of each event. In case of simulated data, date and time are assigned to events using the data taking period of the detector with proper luminosity weighting. During reconstruction of these events corresponding information from the data base are used. This process is known as the *real detector simulation* of Monte Carlo events.

5.4 Event Reconstruction

Event reconstruction is the procedure where the digitised informations of an event are converted into physically meaningful quantities. The Monte Carlo events after detector simulation and the real data recorded by the L3 data acquisition system are reconstructed in the same way, as shown in a block diagram in figure 5.1. The event reconstruction in L3 is performed in the framework, known as REGEL3. Events are reconstructed at individual sub-detector level in the first step where the measurements from that sub-detector component are considered without any reference to other sub-detectors. At a later stage, informations from different sub-detectors are combined to obtain global quantities. Some of the standard reconstruction procedures are described below.

5.4.1 Track Reconstruction

The trace of a charged particle passing through the central tracking chamber is reconstructed from the hits generated by the particle in detector. The momentum as well as the sign of the charge of a track is reconstructed from a fit to the coordinates of the hits. The θ and ϕ coordinates of the track at the vertex are also measured. The parameters which define the quality of a reconstructed track are given by

- number of hits associated to the track,
- total length of the track segment (SPAN) from the innermost and outermost hits,
- the distance of closest approach (DCA) of the track to the interaction vertex,
- the transverse momentum of the track (p_T),
- the χ^2 of the track fit.

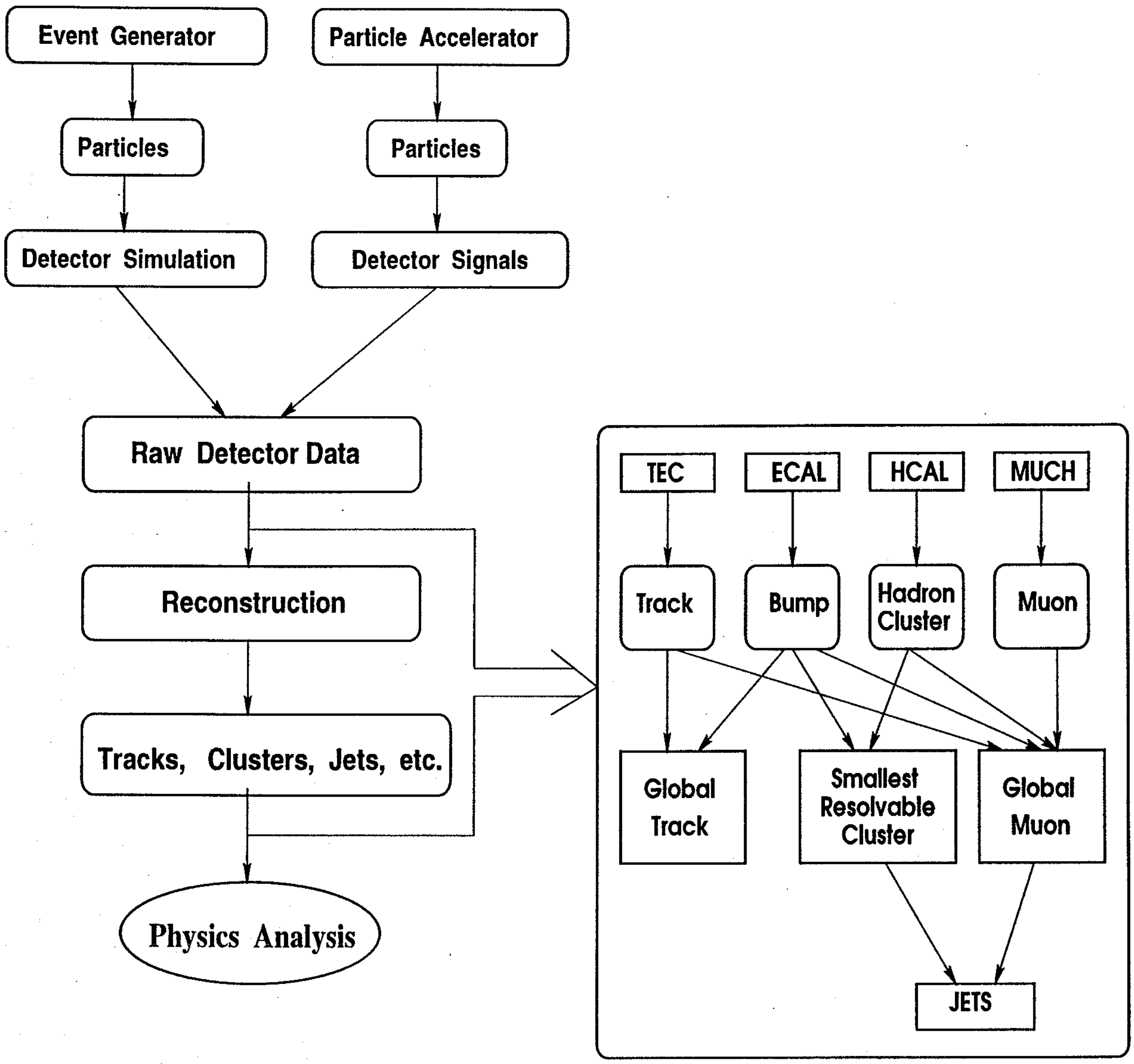

Figure 5.1: Schematic view of event reconstruction

5.4.2 Reconstruction of Clusters in Electromagnetic Calorimeter

The energy and direction of the particles interacting with the crystals in the electromagnetic calorimeter are determined by reconstructing clusters from the energy deposits in the individual crystals.

Raw ADC signals in each crystal are converted into energy deposits taking into account the variation of response of the crystals, due to variation of temperature, radiation damage and aging effect. Adjacent crystals with energy greater than 10 MeV are combined into groups to form geometrical clusters. Clusters having energy less than 40 MeV are dropped.

Within a geometrical cluster, crystals corresponding to local maxima are identified. These crystals are known as *bump crystals* and should have energy greater than 40 MeV. In the next step the remaining crystals are associated to their nearest bump crystal in the same geometrical cluster. If a crystal is at the same distance from more than one bump crystals, it is associated with the more energetic one. A bump crystal along with its associated neighbouring crystals forms a *bump*. A single bump corresponds to a particle in the electromagnetic calorimeter.

As electrons, photons, hadrons and muons interact differently with the electromagnetic calorimeter, the study of the shape of the shower produced in the electromagnetic calorimeter enables us to identify the origin of the shower.

A cluster in the electromagnetic calorimeter is characterised by,

- number of crystals associated,
- energy of the bump crystal (E_1),
- energy deposits (E_9 and E_{25}) in neighbouring 3×3 and 5×5 crystal matrix,
- the ratio of E_9 and E_{25},
- The χ^2 of the shower shape fit.

5.4.3 Reconstruction of Clusters in Hadron Calorimeter

Clusters in the hadron calorimeter are formed from the signals from individual towers. To reduce uranium noise contribution to a minimum, only towers with energy deposits larger than 9 MeV are accepted. Neighbouring towers, either radially or at an angle, are then combined to form clusters using pattern recognition algorithms. Clusters can be classified as originating either from interacting hadrons or muons.

5.4.4 Muon Reconstruction

Muons are reconstructed from the signals in the muon chamber. Hits are combined into segments in both P and Z chambers. Thereafter the P segments are matched with the Z segments in the same octant. A reconstructed muon track should have at least two P segments and one Z segment. A muon track is characterised by,

- number of P or Z segments in the track,
- total or transverse momentum of the track,
- distance of closest approach (DCA) of the muon track back traced to the interaction vertex,
- time of flight measured by associated scintillators.

5.4.5 Smallest Resolvable Cluster

Reconstructed objects from individual sub-detector components are combined to form global reconstructed objects. In the first step, tracks reconstructed in the central tracking chamber are associated, depending on the angular closeness, to the energy deposits in the electromagnetic calorimeter and in the hadron calorimeter. The remaining bumps in the electromagnetic calorimeter are then matched with the hadron clusters provided there is energy deposit in the front layer of the hadron calorimeter. Finally muon tracks are matched with the closest calorimetric energy deposits.

The resulting objects are known as the *smallest resolvable clusters* (SRC's). The SRC's are classified as electromagnetic, hadronic or mixed origin depending on the information of the corresponding subdetectors.

5.4.6 Jet Reconstruction

The jets are reconstructed from the reconstructed electromagnetic and hadronic clusters and the muons in a geometrically connected region in the detector. The most energetic cluster in that region is selected as a seed to form a jet. By an iterative process neighbouring clusters are associated with the seed till a predefined criteria is fulfilled. The main characteristics of a reconstructed jet are the following,

- energy of the jet,
- polar and azimuthal angles of the jet
- invariant mass of the jet,
- multiplicity of the jet.

The reconstructed data are written in three different formats with decreasing size and complexity.

(i) *Data Reconstruction* (DRE) Format: Most of the raw detector informations are available in this format along with the reconstructed quantities.

(ii) *Data Summary* (DSU) Format: The size of the data is reduced in the DSU format after discarding some of the reconstruction results. The raw data can be re-calibrated or the reconstruction of higher level objects can be redone from the DSU files.

(iii) *Data Avanti* (DVN) Format: The simplest data format is DVN, it contains most of the reconstructed quantities, but no raw data information. The size is much reduced and hence it allows a fast data access option. However, re-calibration or re-reconstruction is not possible from DVN files.

5.5 Measurement of Luminosity

Precise determination of cross section of a process in a collider experiment requires very accurate measurement of the integrated luminosity. For a particular process of cross section σ, luminosity $\mathcal{L}$ determines the number of events that might be detected during a time interval.

In e^+e^- collider luminosity is determined from the number of small angle Bhabha events, $e^+e^- \to e^+e^-$.

$$\mathcal{L} = \frac{N_{\mathrm{Bhabha}}}{\epsilon \cdot \sigma_{\mathrm{Bhabha}}} \tag{5.1}$$

where N_{Bhabha} is the measured number of Bhabha events, σ_{Bhabha} is the theoretical cross section of the process and ϵ is the detector acceptance for the events.

At small angle the process is dominated by the photon exchange in t channel. The differential cross section in the t channel scattering is given by

$$\frac{d\sigma_{\mathrm{Bhabha}}}{d\cos\theta} \propto \frac{1}{\theta^3} \tag{5.2}$$

where θ is the scattering angle. Clearly the cross section rises sharply at small scattering angles. These small angle events are detected in the luminosity monitor situated in the very forward direction on both sides of the interaction point.

The selection of these events is based on the energy deposits in the calorimetric part of the luminosity monitor. Events are required to have two back to back energy clusters one in the forward (+Z) and the other in the backward (−Z) luminosity monitors. The selection criteria [61, 62] are the following,

- The reconstructed cluster energy on one side must be greater than 80% of the beam energy and on the other side must be greater than 40% of the beam energy.

$$\begin{aligned} E_{max} &> 0.8\,E_{beam} \\ E_{min} &> 0.4\,E_{beam} \end{aligned}$$

- The reconstructed cluster is required to have θ and ϕ coordinates one crystal away from the calorimeter edges to avoid the edge effects. Cluster on one side must be confined to a tight fiducial volume defined as

$$\begin{aligned} 32\,\text{mrad} &< \theta < 54\,\text{mrad} \\ |\phi - 90^\circ| &< 11.25^\circ \\ |\phi - 270^\circ| &< 11.25^\circ \end{aligned}$$

  and the cluster on the other side is required to be within a loose fiducial volume given by,

$$\begin{aligned} 27\,\text{mrad} &< \theta < 65\,\text{mrad} \\ |\phi - 90^\circ| &< 3.75^\circ \\ |\phi - 270^\circ| &< 3.75^\circ \end{aligned}$$

  The definition of the fiducial volume is very crucial as the cross section varies rapidly with scattering angle θ.

- The coplanarity angle of the two clusters on either side must satisfy

$$|\Delta\phi - 180| < 10^\circ$$

The cross section for the events $e^+e^- \rightarrow e^+e^-$ has been determined from the event generator BHLUMI [48]. The theoretical uncertainty due to missing higher order calculation is 0.11 % which contributes to the systematics error. Due to the high statistics of events the luminosity measurement is dominated by systematic errors. The measured values of luminosity in different years are listed in table 5.1. The systematic error with contributions from various sources are also summarised in the table. The measurements for the year 1990-1992 and 1993-1994 are published [61], [62]. The measurements of 1995 are *preliminary.*

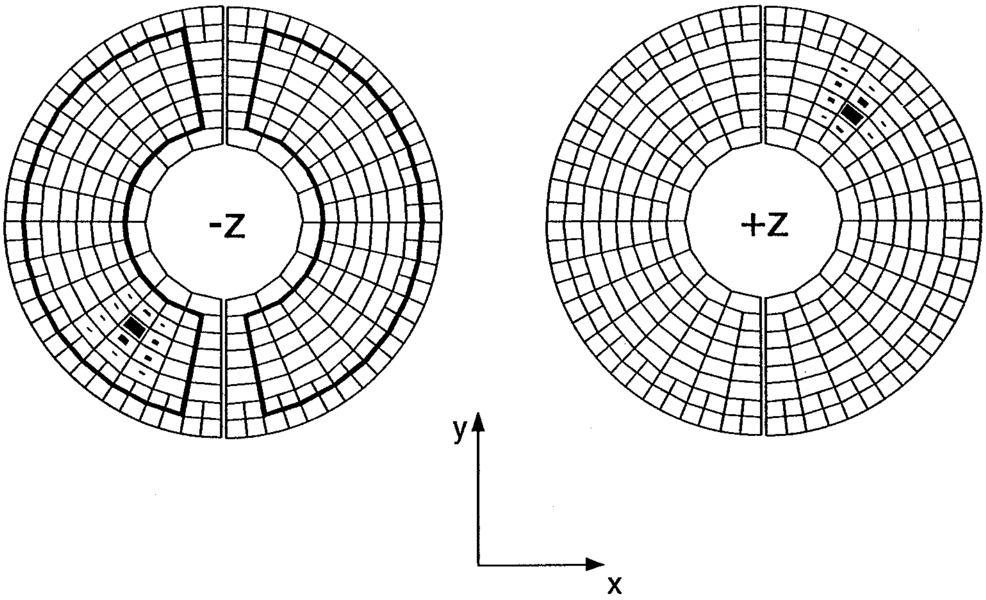

Figure 5.2: A small angle Bhabha event in the luminosity monitors

	1990/1991	1992	1993	1994	1995
Measured Luminosity (pb^{-1})	18.4	22.4	31.7	43.2	19.4
Systematic Errors					
Sources	Fraction (%)				
Selection Criteria	0.30	0.30	0.04	0.05	
Detector Geometry	0.40	0.40	0.06	0.03	
Total Experimental	0.50	0.50	0.08	0.05	0.10
Monte Carlo Statistics	0.10	0.10	0.06	0.06	0.08
Theoretical uncertainty	0.25	0.25	0.11	0.11	0.11
Overall	0.60	0.60	0.15	0.14	0.17

Table 5.1: The measured values of luminosity in different years with the systematic error.

Chapter 6

Analysis of $e^+e^- \rightarrow \tau^+\tau^-$ Events

A precise measurement of the mass and decay width of Z^0 requires a very accurate determination of cross sections for different centre of mass energy points of the different processes $e^+e^- \rightarrow Z^0 \rightarrow$ e^+e^-, $\mu^+\mu^-$, $\tau^+\tau^-$, $\nu\bar{\nu}$ and hadrons. Z^0 dominantly decays into hadrons (Branching ratio $\sim$ 70%), whereas charged leptons contribute only 10% to the total width of Z^0. The neutrinos, which are invisible in the detector, account for 20% of all the final states.

In this chapter we describe the analysis of the process $e^+e^- \rightarrow \tau^+\tau^-$ using L3 detector. We first describe the selection of $\tau^+\tau^-$ events. The determination of cross section and forward backward asymmetry from the selected sample of events are then described. Different sources of the systematic errors to these measurements and their estimations are also discussed.

6.1 Event Signature

The mean life time of τ is 0.295 ps which corresponds to an average decay length of 2.3 mm (at 45 GeV in the lab frame). So τ's decay inside the beam pipe before reaching the first sensitive layer of the detector. We need to identify τ's from their decay products. τ can decay to a variety of final states. The present knowledge of the various decay modes of τ is summarised in table 6.1 [63]. In terms of number of charged particles, branching ratio of τ to one prong, three prongs and five prongs or more are 84.96%, 14.91% < 0.1% respectively.

The visible decay products of τ consist of electron or muon or a small number of charged and neutral hadrons. Due to the presence of neutrinos, a tau event is always accompanied by missing energy. The decay products of τ are highly boosted at LEP energies. So the jets are narrow and almost back to back in case of hadronic τ decays. The characteristics of τ-pair events are the following: a few tracks in the tracking chamber, energy deposits in the electromagnetic and hadron calorimeters and in case of muonic τ decays, identified muons

Decay mode of τ	Branching Fraction (%)
$\tau \rightarrow e\overline{\nu}_e\nu_\tau$	18.01 ± 0.18
$\tau \rightarrow \mu\overline{\nu}_\mu\nu_\tau$	17.65 ± 0.24
$\tau \rightarrow \pi\nu_\tau$	11.70 ± 0.40
$\tau \rightarrow \rho\nu_\tau$	25.20 ± 0.40
$\tau \rightarrow a_1\nu_\tau$	15.20 ± 1.10
$\tau \rightarrow K^*\nu_\tau$	1.45 ± 0.18
$\tau \rightarrow K\nu_\tau$	0.67 ± 0.23
$\tau \rightarrow$ Others	10.12 ± 1.10

Table 6.1: Branching ratio of τ in different decay modes

in the muon chamber. As a consequence, selection of τ-pair events requires information from almost all the sub-detectors starting from tracking chamber all the way upto the muon chamber. A candidate event is shown in figure 6.1.

The background contribution comes from e^+e^-, $\mu^+\mu^-$, $q\overline{q}$, various two photon processes and cosmic rays. Selection of a pure sample of τ-pair events would need to remove events from all these backgrounds processes.

We have used the data collected in 1992, 1994 and 1995 for our analysis. During 1992 and 1994, the LEP e^+e^- collider operated at Z^0 peak ($\sqrt{s} \approx M_Z$) whereas in 1995 a scan of Z^0 resonance was performed at three energy points on or around the Z^0 peak ($\sqrt{s} \approx M_Z$, and $\sqrt{s} \approx M_Z \pm 2$ GeV).

For this analysis, we have used data taken in good running condition of the detector. Data with bad condition of TEC, electromagnetic calorimeter, hadron calorimeter, scintillator, muon chamber or the trigger are not used.

The data are compared with Monte Carlo events, generated using the KORALZ 4.02 [51] for signal and JETSET 7.4 [53], PYTHIA 5.7 [56], BHAGENE [50], DIAG36 [55] for the different background processes.

In the detector modelling, the condition of the real detector (dead cells, hot crystals, etc.) has been simulated on a run by run basis. A run corresponds to a number of events collected over a time when the detector conditions do not change.

6.2 Event Selection

The selection criteria are designed to select a sample of signal ($e^+e^- \rightarrow \tau^+\tau^-$) events with high efficiency and with background contamination from other processes as low as possible. Using this clean sample of events, one can proceed to determine cross section

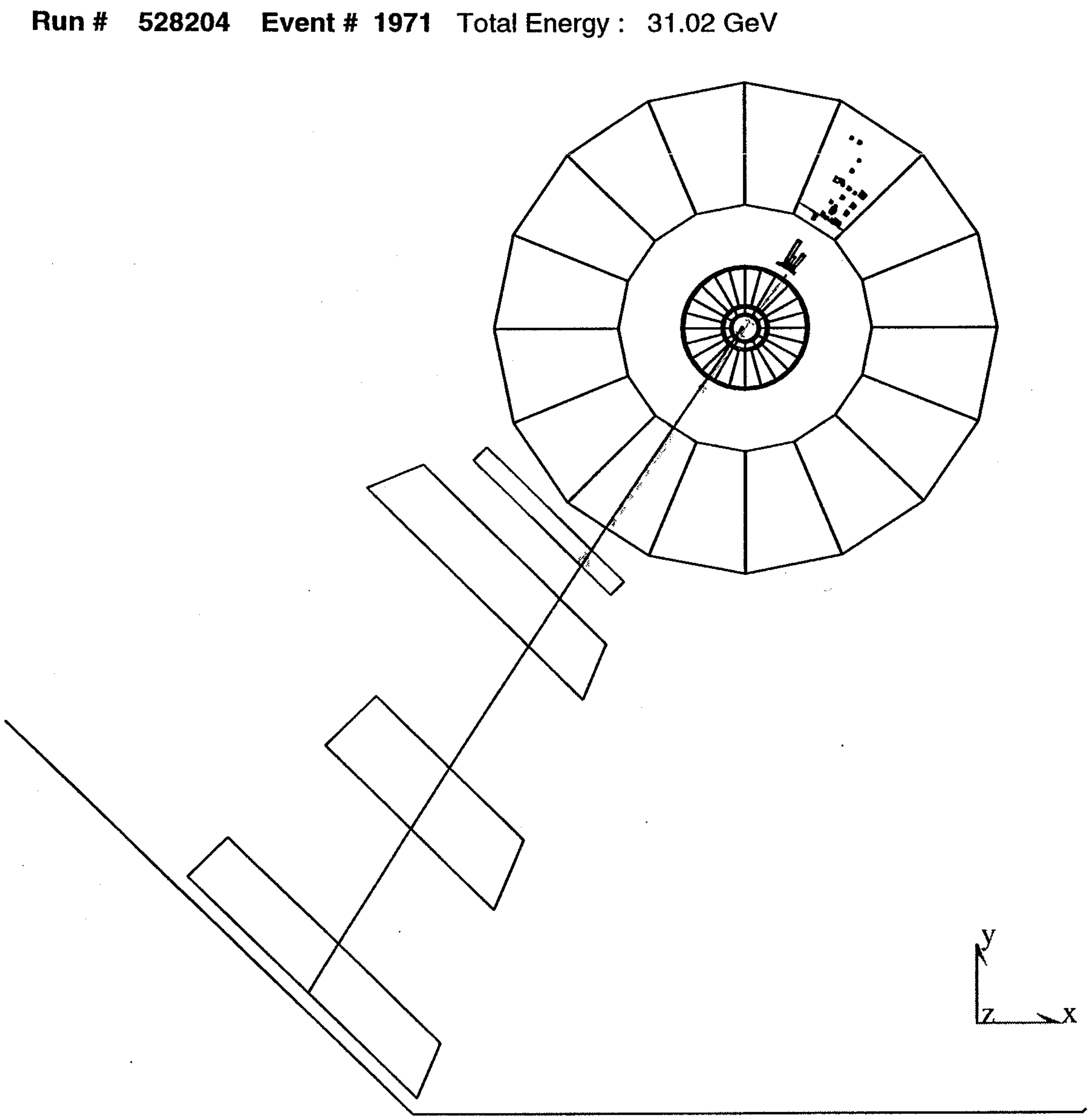

Figure 6.1: A candidate τ-pair event in the L3 detector. One of the τ's has decayed hadronically depositing energy in the hadron calorimeter. The other τ has decayed in the muon mode giving a very good muon track reconstructed from hits in all three layers of the muon chamber.

and asymmetry.

6.2.1 Selection Variables

Objects reconstructed in the central tracking chamber, calorimeters and muon chamber and their characteristics are utilised to identify a clean sample of τ-pair events. These reconstructed objects should qualify some specific criteria before they can be used to build selection variables. The selection variables used are discussed in the following.

- Thrust:

  The event thrust [65] is defined as,

$$\mathrm{T} = \frac{\max \sum_{\mathrm{i}} |\vec{\mathrm{p}}_{\mathrm{i}} \cdot \vec{\mathrm{n}}_{\mathrm{T}}|}{\sum_{\mathrm{i}} |\vec{\mathrm{p}}_{\mathrm{i}}|} \tag{6.1}$$

  where i runs over all the final state particles. The axis $\vec{\mathrm{n}}_{\mathrm{T}}$ is chosen to maximise the value of the above expression. The direction corresponding to the event thrust is called thrust axis ($\vec{\mathrm{n}}_{\mathrm{T}}$).

- Jet:

  Jets are reconstructed from the smallest resolvable clusters and the muons in the detector. Starting from the most energetic cluster, one combines other clusters within a certain cone. Reclustered objects above a minimum energy are called jets.

- Acolinearity Angle:

  Acolinearity angle between the two most energetic jets describes the amount of deviation from back to back configuration of the two jets. We define acolinearity angle as,

$$\zeta_{12} = \pi - \psi_{\mathrm{jet_1,jet_2}} \tag{6.2}$$

  where $\psi_{\mathrm{jet_1,jet_2}}$ is the angle between the two jets.

- Bumps:

  Electrons and photons deposit their energies in BGO crystals which are contained within a few crystals around the central one. Showers produced by hadrons in BGO, on the other hand, have much broader lateral distributions. A bump is identified to be of electromagnetic origin if it satisfies

$$\frac{\mathrm{E_9}}{\mathrm{E_{25}}} > 0.98 \tag{6.3}$$

  where $\mathrm{E_9}$ and $\mathrm{E_{25}}$ refer to the energy deposits in the crystal matrices of 3×3 and 5×5 crystals respectively around the central one.

- Clusters:

  Particle multiplicity in an event is defined from smallest resolvable clusters (SRC) discussed in section 5.4.5. We define a cluster for our analysis if one of the following criteria is satisfied.

  - energy in the electromagnetic calorimeter is greater than 0.1 GeV and energy in the hadron calorimeter is greater than 0.9 GeV,
  - energy in the electromagnetic calorimeter is greater than 0.1 GeV and there are at least two crystals in the bump,
  - if there is no energy deposit in the electromagnetic calorimeter then the energy in the hadron calorimeter should be greater than 1.4 GeV (1.8 GeV for 1995 data).

  The hadron calorimeter gate was changed in 1995 and hence the energy cut was increased to 1.8 GeV to minimise the noise.

- Good Track:

  A reconstructed track is qualified as a *good track*, if it fulfils the following conditions,

  - at least 20 hits,
  - a minimum SPAN of 30,
  - distance of closest approach (DCA) to the vertex point less than 20 mm,
  - a minimum transverse momentum (p_T) of 50 MeV.

  We also demand that the track should lie in an efficient ϕ sector of TEC. Sometimes the ϕ coordinate of a track is affected by mirroring of the track in TEC sectors. Mirroring happens when a track does not have an inner TEC sector hit and passes through a region very close (less than 2°) to the cathode plane. In that case, left-right ambiguity wires are not able to solve the ambiguity. We identify those tracks and try to match it with a calorimetric cluster of energy above 100 MeV or a muon identified in the muon chamber, in a cone less than (2.5°). The solution (between the original and the mirror) for which the cluster or the muon is closer is selected. If neither of the solutions has such a neighbour we do not consider the track as a good one. Only good tracks are used for the analysis.

6.2.2 Summary of Selection Cuts

We discuss here the selection cuts which are applied on different selection variables described in section 6.2.1. The distribution of different selection variables are compared with the Monte Carlo predictions where different backgrounds are superimposed on the signal. Figures 6.2-6.8 show distributions of different selection variables where all other selection cuts except the one under consideration are applied. The dots represent the data and the shaded areas represent contributions from different background processes estimated from Monte Carlo. The empty region represents the signal Monte Carlo. Shades corresponding to different background processes are indicated in figure 6.3. The arrow indicates the value where the cut for a particular variable has been applied.

Events are selected in the fiducial volume restricted to the central part of the detector. We define the barrel region by putting a cut on the direction of the thrust axis (figure 6.2) :

$$|\cos\Theta_{\mathrm{thrust}}| < 0.73$$

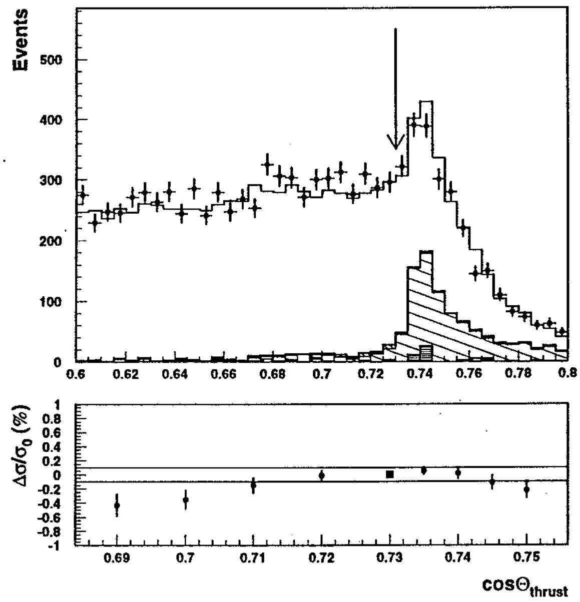

Figure 6.2: Distribution of cosine of the polar angle of thrust alongwith Monte Carlo predictions. The most dominant background comes from Bhabha events. The arrow shows the nominal position of the cut. The systematic error due to the variation of this cut is shown at the bottom.

We demand that there should be at least two jets in the event with energies with energies (figure 6.3):

$$\mathrm{E_{Jet1}} > 7\ \mathrm{GeV}$$
$$\mathrm{E_{Jet2}} > 3\ \mathrm{GeV}$$

The cuts mentioned above conform to the requirements in level 1 energy trigger (the primary trigger for τ-pair events).

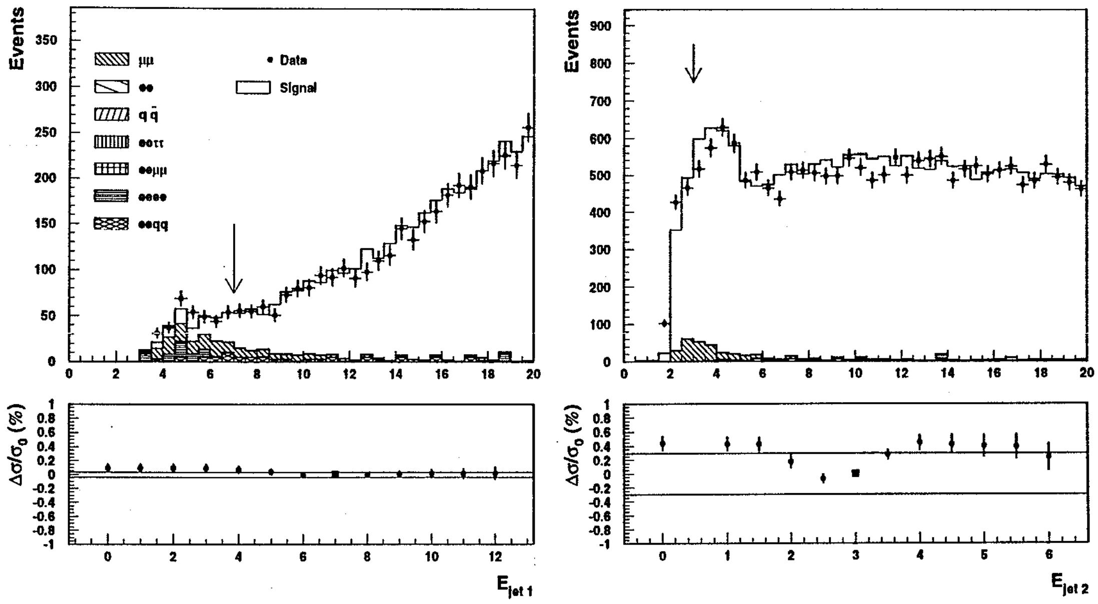

Figure 6.3: Distribution of the most (left) and second most (right) energetic jets compared with Monte Carlo predictions. The arrows show the nominal positions of the cuts. The systematic error due to the variation of cut is negligible for the most energetic jet compared to that for the second most energetic jet.

To remove most of the beam gas and two photon backgrounds we require that the jets should be back to back as expected from $Z^0 \rightarrow f\bar{f}$ decays in the laboratory frame. This requirement is fulfilled by demanding the acolinearity angle (ζ_{12}) of the two most energetic jets to be (see figure 6.4):

$$\zeta_{12} < 0.25 \text{ rad}$$

Cosmic events and dimuon events with muons not reconstructed in the muon chamber are removed by a cut on the total energy deposited in the electromagnetic calorimeter. This cut uses the fact that the muons give the signature of a minimum ionising particle in the calorimeter (see figure 6.5):

$$E_{BGO} > 2 \text{ GeV}$$

Cosmic background is further suppressed by applying a cut on the time recorded by the scintillators with respect to the beam crossing time after the correction for time of flight. The scintillator time for cosmic muons are not correlated with the beam crossing time, but the muon coming from the real Z^0 decays are. The cosmic muons give a flat distribution as shown in figure 6.5. The best scintillator time should be:

$$\begin{aligned} |t_{best}| &< 2.5 \text{ ns (for 1994 data)} \\ &< 3.0 \text{ ns (for 1995 data)} \end{aligned}$$

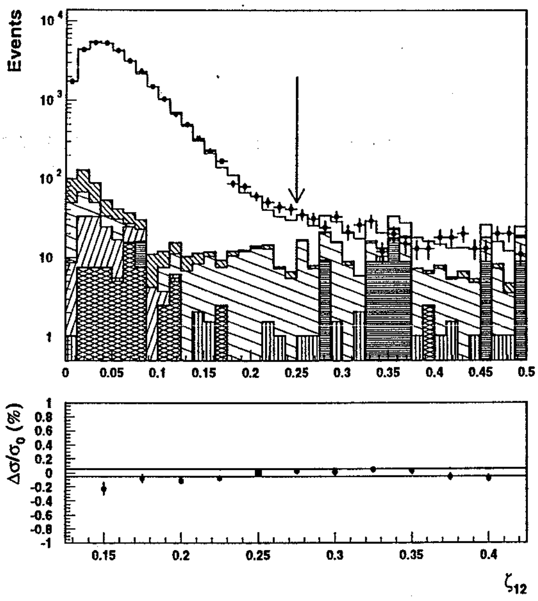

Figure 6.4: Distribution of the acolinearity angle (ζ_{12}). The arrow shows the nominal cut position. The background at large acolinearities arises due to two photon events and Bhabha events. The contribution of systematic error due to this cut is negligible.

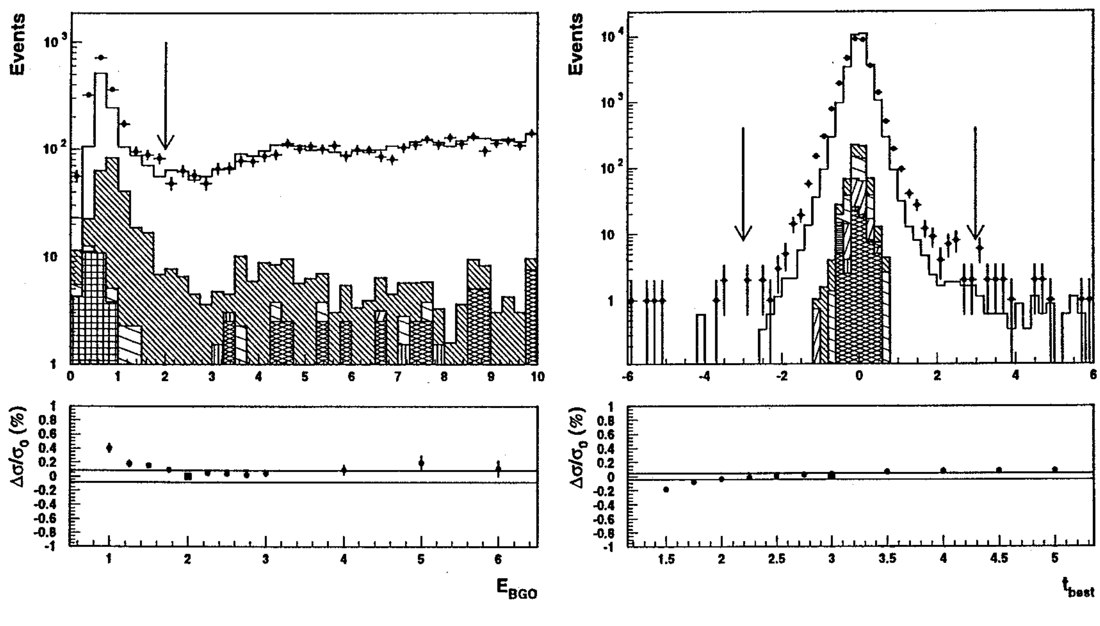

Figure 6.5: Distribution of the BGO barrel energy (left) and the best scintillator time (right) compared to the Monte Carlo predictions. The arrows show the nominal cut positions for these two variables. The dimuon $e^+e^- \to \mu^+\mu^-$ background is dominated in the low BGO energy region. In the best scintillator time distribution the flat part of the distribution for data in the region $|t_{\text{best}}| > 2.0$ arises due to the presence of cosmic rays. The systematic errors are very small for both the selection variables.

Bhabha events ($e^+e^- \rightarrow e^+e^-$) are rejected by requiring that the most and second most energetic bumps should have energies less than 80% and 60% of the beam energy respectively (figure 6.6):

$$E_1 < 0.8\,E_{beam}$$
$$E_2 < 0.6\,E_{beam}$$

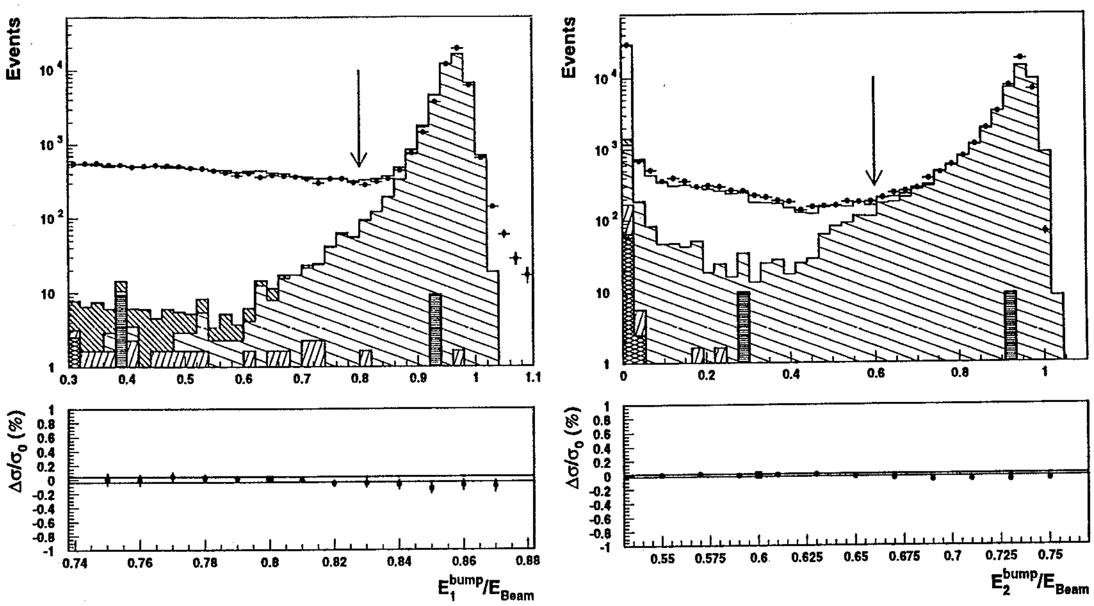

Figure 6.6: Distributions of the scaled most (left) and second most (right) energetic bumps compared with the Monte Carlo predictions. The arrows show the nominal cut positions for these two variables. The background at high energy region comes entirely from Bhabha events.

Dimuon events ($e^+e^- \rightarrow \mu^+\mu^-$) are rejected similarly requiring that the momenta of the most and the second most energetic muons should be less than 80% and 20% of the beam energy (figure 6.7) :

$$P_1^\mu < 0.8\,E_{beam}$$
$$P_2^\mu < 0.2\,E_{beam}$$

Requirement of low particle multiplicity in the final state rejects most of the hadronic events. We require the number of clusters defined in section 6.2.1 to satisfy (figure 6.8):

$$N_{cluster} < 13$$

The rest of the hadronic Z^0 decays can be rejected by imposing the condition that the jets should be narrow. The narrowness of a jet is defined from the difference of the angle

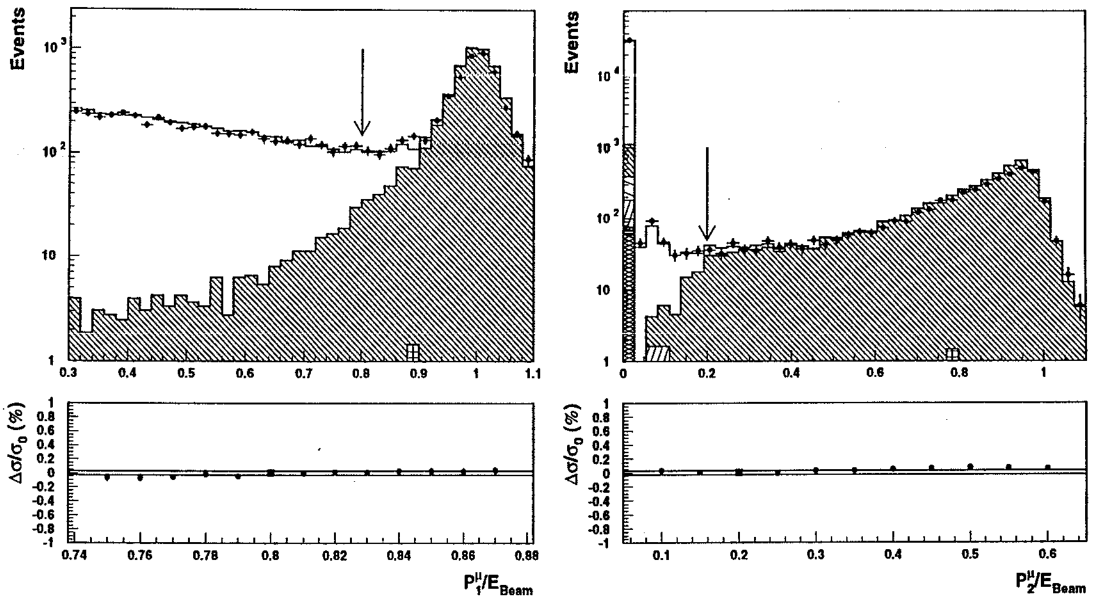

Figure 6.7: Distributions of the scaled momenta of the most and the second most energetic muons. The arrows show the nominal cut positions for these two variables. The background at high momentum region comes entirely from dimuon events.

of a track to its nearest jet axis. We require the maximum azimuthal angle between a track and its nearest jet (figure 6.8) :

$$\Phi_{\mathrm{TEC}} < 0.25 \text{ rad}$$

We require that there should be at least one good track in the event to remove the remaining cosmic ray background. The distribution is shown in figure 6.9.

6.3 Measurement of Cross Section

After selecting the events, we correct the number of observed events for acceptance and background contamination from different processes. We use Monte Carlo simulations for signal ($e^+e^- \to \tau^+\tau^-$) and all possible background channels to estimate acceptance and background contaminations respectively. The remaining small amount of background is subtracted from the selected data sample. The cross section is computed by dividing the background subtracted data by the corresponding luminosity and the acceptance

$$\sigma_\tau = \frac{\mathrm{N_{selected}} - \mathrm{N_{background}}}{\epsilon_\tau \mathcal{L}} \tag{6.4}$$

where $\mathrm{N_{selected}}$ is the number of selected events, $\mathrm{N_{background}}$ is the expected number of background events, ϵ_τ is the acceptance for τ pair events and $\mathcal{L}$ is the luminosity.

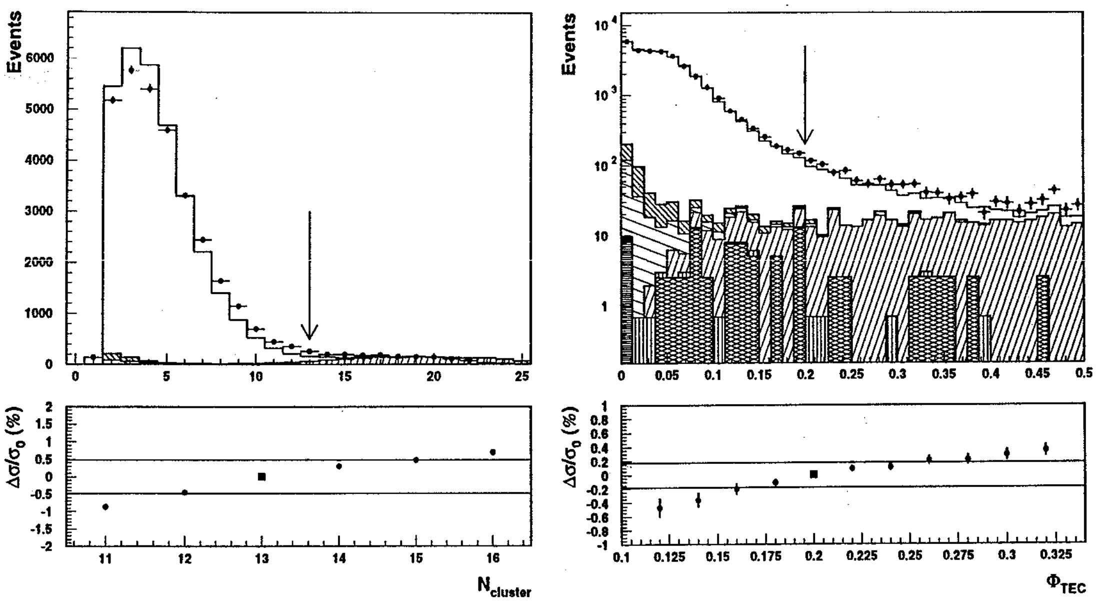

Figure 6.8: Distributions of the number of clusters and Φ_{TEC}. The arrows show the nominal cut positions for these two variables. In these cases, The main background comes from the high multiplicity hadronic events. The agreement between data and Monte Carlo is not very good for the distribution of the number of clusters, which reflects in the systematic error of $\mathrm{N_{cluster}}$.

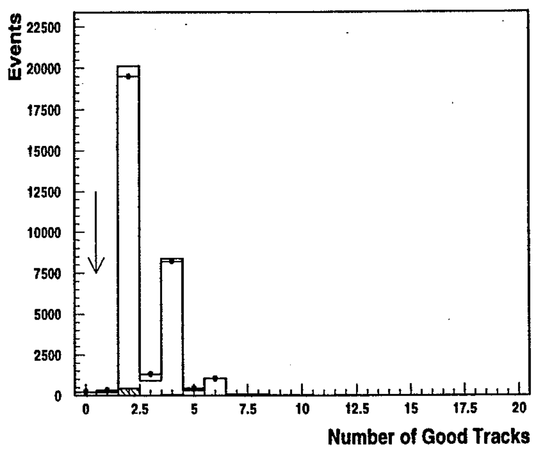

Figure 6.9: Distribution of the number of good tracks

We estimate the selection efficiency to be 75–77% inside the fiducial volume and the overall acceptance to be 48–49% depending on the centre of mass energy. The centre of mass energy at the interaction point is determined from the energy calibration of LEP [64]. We have divided our sample according to the centre of mass energies in different years. The measured cross sections together with the statistical error are summarised in table 6.2. The quoted energy is obtained from the luminosity weighted average over the runs, used in the cross section measurement.

Year	$\sqrt{s}$ (GeV)	Luminosity (nb^{-1})	Events	σ_τ (nb)	Stat. Err.
1992	91.293	20327.400	15026	1.466	0.012
1994	91.218	42260.344	30345	1.472	0.008
1995 prescan	91.160	5135.599	3612	1.464	0.024
1995 scan	89.452	7301.506	1703	0.491	0.012
	91.293	3504.679	2557	1.522	0.030
	92.984	8132.441	2658	0.684	0.013

Table 6.2: Cross sections of $e^+e^- \to \tau^+\tau^-$ for different data sets

6.4 Systematic Errors and Background

The different sources of systematic error in the measurement of cross section of the process $e^+e^- \to \tau^+\tau^-$ can be listed as

- selection criteria,
- background estimation,
- trigger inefficiency,
- acceptance correction,
- modelling of τ decays in the event generator.

6.4.1 Systematic Error from Selection Cuts

The variation of the measured cross section due to the variation of the values of the selection cuts gives a measure of the systematic effects on it. To estimate this error, we vary a particular selection cut while keeping the others fixed to their nominal position and estimate different values of cross sections at different values of that particular cut.

Let σ_o be the cross section obtained with all the cuts at their default values and σ_i (i = 1, 2, 3, ...) be the cross section for the i th value of that particular cut.

$$\sigma_i = \frac{N_i}{\epsilon_i \mathcal{L}} . \tag{6.5}$$

Here N_i is the number of selected event, $\mathcal{L}$ is the luminosity and ϵ_i is the acceptance estimated from signal Monte Carlo. We define systematic error (S) on the cross section for that particular variable by the relative change in cross section with respect to the nominal value as:

$$\begin{aligned} S &= \frac{\Delta\sigma_i}{\sigma_o} \\ &= \frac{\mid \sigma_o - \sigma_i \mid}{\sigma_o} \end{aligned} \tag{6.6}$$

The statistical error associated with the change in the cross section is

$$\Delta S = \frac{\sigma_i}{\sigma_o} \frac{\sqrt{\mid N_0 - N_i \mid}}{N_i} \tag{6.7}$$

The systematic errors on selection cuts are shown in bottom half of figures 6.2-6.8 for corresponding selection cuts. These figures show a good agreement between data and the predictions from Monte Carlo, which is reflected in the systematic errors. The agreement is not very good for E_{Jet2} and $N_{cluster}$ and the contribution of the systematic error from these two variables is higher compared to the rest.

6.4.2 Systematic Error from Backgrounds

The selection criteria select a few background events together with the signal events. They are estimated from Monte Carlo and subtracted on a statistical basis.

The backgrounds for a particular channel x is calculated in the following way,

$$\begin{aligned} N_x^b &= \mathcal{L} \cdot \sigma_x \cdot \epsilon_x \\ &= \mathcal{L} \cdot \sigma_x \cdot \frac{n_x^{sel}}{n_x^{tot}} \end{aligned} \tag{6.8}$$

where $\mathcal{L}$ is the luminosity, σ_x is the generator level cross section for the background channel x and ϵ_x is the selection efficiency calculated from the ratio of total (n_x^{tot}) and selected (n_x^{sel}) number of background events. The error on N_x^b is calculated from the following expression,

$$\Delta N_x^b = \mathcal{L}\, \sigma_x \frac{\sqrt{n_x^{sel}(1-\epsilon_x)}}{n_x^{tot}} \tag{6.9}$$

The estimated background contaminations are summarised in table 6.3. The statistical error on the background estimation gives a systematic effect on the cross section calculation.

The cosmic muons have no correlation with the beam crossing time and hence the best scintillation time for those muons produces a flat distribution shown in figure 6.5. The cosmic background has been estimated from the flat part of the distribution outside the signal region.

Backgrounds	Fraction (%)					
	1992	1994	1995 prescan	1995 peak-2	1995 peak	1995 peak+2
$\mu^+\mu^-$	1.21 ± 0.03	0.74 ± 0.03	0.76 ± 0.06	0.83 ± 0.08	0.83 ± 0.07	0.76 ± 0.07
e^+e^-	1.25 ± 0.03	0.68 ± 0.05	0.62 ± 0.05	1.19 ± 0.10	0.58 ± 0.05	0.59 ± 0.06
$q\bar{q}$	0.40 ± 0.03	0.35 ± 0.03	0.79 ± 0.13	0.85 ± 0.18	1.09 ± 0.17	0.97 ± 0.20
$e^+e^-\tau^+\tau^-$	0.02 ± 0.01	0.02 ± 0.01	0.02 ± 0.01	0.04 ± 0.01	0.03 ± 0.01	0.04 ± 0.01
$e^+e^-\mu^+\mu^-$	< 0.01	< 0.01	< 0.01	< 0.01	< 0.01	< 0.01
$e^+e^-e^+e^-$	0.02 ± 0.02	0.03 ± 0.03	0.09 ± 0.02	0.19 ± 0.05	0.06 ± 0.02	0.13 ± 0.04
$e^+e^-q\bar{q}$	0.01 ± 0.01	0.19 ± 0.04	0.20 ± 0.04	0.50 ± 0.11	0.17 ± 0.05	0.43 ± 0.09
Cosmic	0.08 ± 0.01	0.08 ± 0.01	0.11 ± 0.05	0.40 ± 0.15	0.06 ± 0.04	0.11 ± 0.06

Table 6.3: Estimated background contaminations in the selected sample of $e^+e^- \to \tau^+\tau^-$ from different processes

6.4.3 Systematic Error from Trigger

Trigger system in an experiment decides whether an event should be recorded or not after each beam crossing.

The τ-pair events are triggered requiring a minimum energy in the calorimeters (Energy trigger) or a minimum number of charged particles in the inner tracker (TEC trigger). A muon trigger consisting of at least one muon to reach the muon spectrometer also selects the τ-pair events where one of the τ's decays in the muon mode. The selection cuts which we use to select τ-pair events have been designed to lie within the acceptance of the trigger system. Any inefficiencies in the trigger system affect the selection and hence the measurement.

Level 1

To study the efficiency in level 1, we divide the selected event sample into three categories :

(a) events without any muon, where we consider energy and TEC triggers,

(b) events with only one muon, where energy, TEC, muon triggers are considered,

(c) events with more than one muon , where TEC and muon triggers are considered.

In each of these categories, we estimate the trigger efficiency from the event counts found by only one trigger as compared to those found in more than one trigger.

Let us first consider events without any muon as defined in (a). Let N_E, N_T and N_{ET} are the number of events satisfying only energy (E) trigger, only TEC (T) trigger and both energy and TEC (ET) triggers respectively, and ϵ_E and ϵ_T are the corresponding efficiencies for energy and TEC triggers.

$$\epsilon_E = \frac{N_{ET}}{N_T} \tag{6.10}$$

$$\epsilon_T = \frac{N_{ET}}{N_E} \tag{6.11}$$

The errors on the efficiencies can be calculated as,

$$\Delta\epsilon_E = \frac{\sqrt{N_{ET}(1-\epsilon_E)}}{N_T} \tag{6.12}$$

$$\Delta\epsilon_T = \frac{\sqrt{N_{ET}(1-\epsilon_T)}}{N_E} \tag{6.13}$$

The effective number of events in class (a) can be calculated as,

$$N_a = \frac{N_E N_T}{N_{ET}} \tag{6.14}$$

The trigger efficiency for events in class (a) is calculated from the actual number of events without any muons $N_{\mu=0}$,

$$\epsilon_a = \frac{N_{\mu=0}}{N_a} \tag{6.15}$$

$$\Delta\epsilon_a = \frac{\sqrt{N_{\mu=0}(1-\epsilon_a)}}{N_a} \tag{6.16}$$

For events having at least one muon, the efficiency can be calculated from the number of events satisfying only one trigger (N_E, N_T, N_M), any of the two triggers (N_{ET}, N_{TM}, N_{EM}), and all three triggers (N_{ETM}) and the corresponding efficiencies. In this case to avoid the redundancy of equations we extract the efficiency ϵ_b and effective number of events N_b from a χ^2 minimisation using MINUIT [68].

Similarly for events having more than one muon, the efficiency is calculated considering the number of events satisfying TEC (N_T), muon (N_M) triggers and the corresponding efficiencies ϵ_T, ϵ_M.

The overall efficiency in level 1 is estimated from the three individual efficiencies. The errors of ϵ_a, ϵ_b and ϵ_c are added in quadrature to get the error associated to the levell trigger efficiency. The level 1 trigger efficiency is found to be 99.992 ± 0.006 %.

Level 2

In contrast to level 1, level 2 tries to reject the background events selected by level 1. It becomes operational to those events where only one trigger in level 1 has been satisfied. It mainly rejects non-physical events due to beam-gas and beam-wall interactions and from electronic noise. Events which satisfy more than one trigger in level 1 pass untouched from level 2. Level 2 trigger efficiency has been computed from the flagged level 2 events and is found to be 100% for τ-pair events.

Level 3

Level 3 trigger takes the final decision whether the event should be written to tape or not. The selection criteria used by level 3 are based on the complete digital data of the event from the full detector readout. The digitised data with finer granularity and resolution allow to apply tighter selection criteria and help to decrease the electronic noise. Events with multiple level 1 triggers are passed unhindered through level 3. The efficiency of level 3 triggers has been estimated to be 100%.

The overall trigger inefficiency comes entirely from the level 1. The statistical error in the estimation of the trigger efficiency has been attributed to the systematic error in cross section determination.

6.4.4 Systematic Error from Acceptance

We estimate the geometrical acceptance and the selection efficiency from the Monte Carlo events. The statistical error in the determination of these numbers due to limited statistics results in a systematic error in the cross section measurement.

6.4.5 Systematic Error from Tau Decay Modelling

The selection efficiency of τ-pair events depends on τ decay modes. The τ decay branching ratios are known with certain accuracy. The decay mode averaged efficiency depends on the values of the branching fractions, hence the error in the branching fractions gives the systematic effect on efficiency and so on the cross section. From the generator level information we have calculated the decay mode dependent efficiencies. They are written in the form of a matrix which is known as the efficiency matrix (M). Efficiency matrix is shown in figure 6.10 where the size of each square is proportional to the selection efficiency for that mode of τ decay. The efficiency is zero for those events where both the τ's decay in the muon mode. The branching ratios of different decay modes of τ are listed in table 6.1.

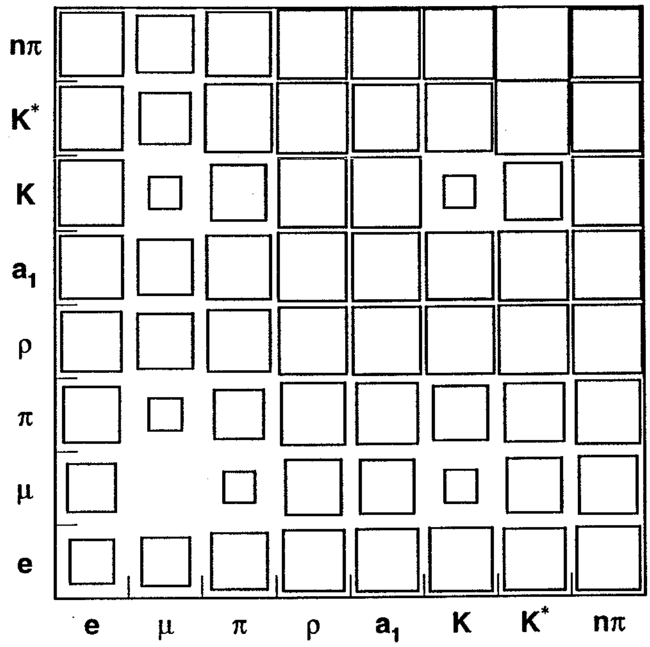

Figure 6.10: Efficiency matrix for different decay modes of τ

Let B_i be the branching fraction of τ in a particular decay mode i and δB_i is the error on it. The B_i's can be arranged to form a vector B, The decay mode averaged efficiency can be calculated in the following way

$$\epsilon = B^{\dagger}MB \tag{6.17}$$

The errors on the branching ratios contribute to the systematic error on cross section measurement through the error on the decay mode averaged efficiency $\delta\epsilon$.

6.4.6 Overall Error

The systematic errors from all the sources described above are summarised in table 6.4 separately for the different event samples. The overall systematic error is obtained by combining the individual errors in quadrature. The systematic error lies within the range 0.54% to 0.88%. In table 6.5, we list the measured values of cross sections at different centre of mass energy points. The statistical and the systematic errors are listed in fourth and fifth columns of the table. The measured cross sections are plotted as a function of the centre of mass energy point in figure 6.11. The solid line represents the Standard Model

Systematic errors	Systematic Errors (%)					
	1992	1994	1995 prescan	1995 peak-2	1995 peak	1995 peak+2
Selection Cuts	0.66	0.61	0.63	0.80	0.47	0.72
Background	0.06	0.08	0.17	0.29	0.20	0.25
Trigger Inefficiency	0.03	<0.01	0.07	< 0.01	< 0.01	< 0.01
MC Statistics	0.10	0.10	0.13	0.11	0.15	0.11
Decay Modelling	0.25	0.20	0.20	0.20	0.20	0.20
Total	0.71	0.65	0.71	0.88	0.57	0.80

Table 6.4: Summary of Systematic Errors

Year	$\sqrt{s}$ (GeV)	σ_τ (nb)	Stat. Err.	Syst. Err. (%)
1992	91.293	1.466	0.012	0.71
1994	91.218	1.472	0.008	0.65
1995 prescan	91.160	1.464	0.024	0.71
1995 scan	89.452	0.491	0.012	0.88
	91.293	1.522	0.030	0.57
	92.984	0.684	0.013	0.80

Table 6.5: Cross sections of the process $e^+e^- \to \tau^+\tau^-$ in different data sets with statistical and systematic errors

predictions calculated using the analytical programme ZFITTER [66], using Z^0 mass of 91.186 GeV, top quark mass of 175 GeV, Higgs mass of 300 GeV and α_s of 0.123. The good agreement between the measured values and the theoretical predictions is evident. In the bottom part of the figure the ratio of measured cross section to its Standard Model prediction is plotted.

6.5 Measurement of Forward Backward Asymmetry

The forward backward asymmetry is defined as

$$A_{FB} = \frac{\sigma_F - \sigma_B}{\sigma_F + \sigma_B} \tag{6.18}$$

where $\sigma_F(\sigma_B)$ is the cross section of the process $e^+e^- \to f\bar{f}$ with the fermion scattered in the forward (backward) hemisphere with respect to the e^- direction. To measure the forward backward asymmetry in $e^+e^- \to \tau^+\tau^-$, we need to measure the scattering angle, i.e the angle of τ^- with respect to e^- direction. The scattering angle of the event is determined from the angle and the charge measurement of the τ jets. There are different conventions to determine the angle of an event: from the polar angle of (a) the thrust axis, (b) the most energetic jet, (c) the negatively charged jet. We used polar angle of

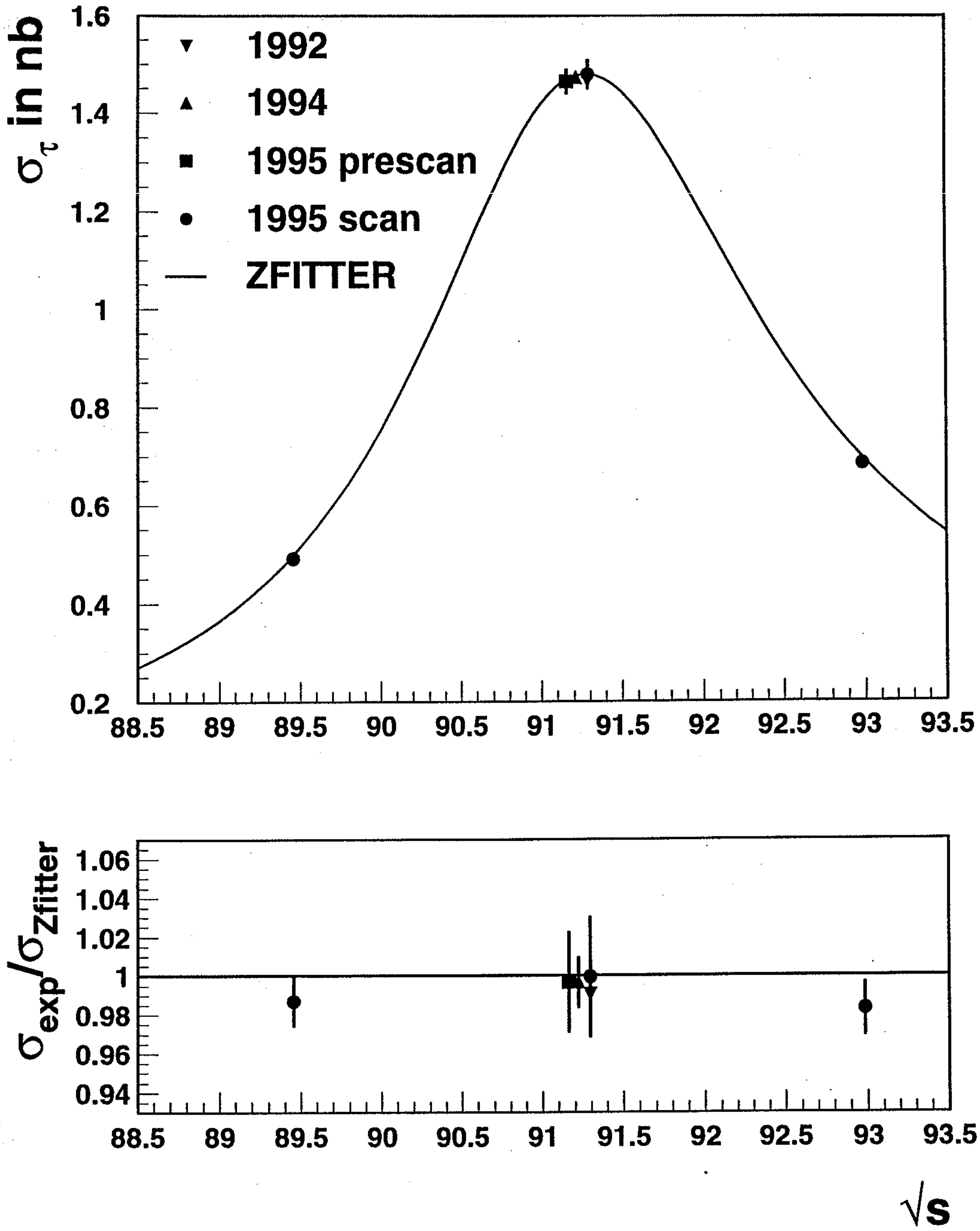

Figure 6.11: The measured cross sections of $e^+e^- \to \tau^+\tau^-$ at different centre of mass energy points. The solid line shows the prediction of the Standard Model. The lower plot shows the ratio of the measured and the Standard Model cross section values.

the thrust axis as the event angle for the analysis. The event angle defined from other conventions are also tested and they give comparable results. The difference is quoted as systematic error.

The charge of τ is determined from the charges of its decay products as measured in the tracking chamber. In case of presence of muons, the charge is measured from muon spectrometer. The sum of all the charges of tracks in a τ jet defines the charge of the jet.

6.5.1 Fitting Procedure

The selected events which are used for the measurement of cross section are also used for the measurement of asymmetry. The requirement that the acolinearity angle should be less than 15° removes most of the events with hard bremsstrahlung photon. We restrict the fiducial volume further. It can be seen from the $\cos\Theta_{\mathrm{thrust}}$ distribution in figure 6.2 that the background events are concentrated in the region $|\cos\Theta_{\mathrm{thrust}}| > 0.7$. We demand that the events should be in the region $|\cos\Theta_{\mathrm{thrust}}| < 0.70$ in order to remove most of the background events. We also demand the two jets in an event to have opposite charges.

The angular distribution is described by,

$$\frac{1}{\sigma}\frac{\mathrm{d}\sigma}{\mathrm{d}\cos\theta} = \frac{3}{8}(1+\cos^2\theta) + \mathrm{A_{FB}}\cos\theta \tag{6.19}$$

So the forward backward asymmetry can be determined from a maximum likelihood fit with the likelihood function defined as

$$\mathrm{L} \equiv \prod_{\mathrm{i}} \left(\frac{3}{8}(1+\cos^2\theta_{\mathrm{i}}) + \mathrm{A_{FB}}\cos\theta_{\mathrm{i}}\right) \tag{6.20}$$

where θ_{i} is the scattering angle for event i .

Before the fit, we have weighted the events by the acceptance correction factors in various angular ranges. Figure 6.12 shows the angular distribution in $\mathrm{e^+e^-} \to \tau^+\tau^-$ together with the fit described above.

6.5.2 Corrections to Forward Backward Asymmetry

The observed forward backward asymmetry is corrected for the charge confusion and the background contamination.

Charge Confusion

There is a non zero probability P to measure the charge of a τ jet with wrong sign. Charge confusion affects number of observed forward and backward events and hence the asymmetry. We need to correct our observed asymmetry for this effect.

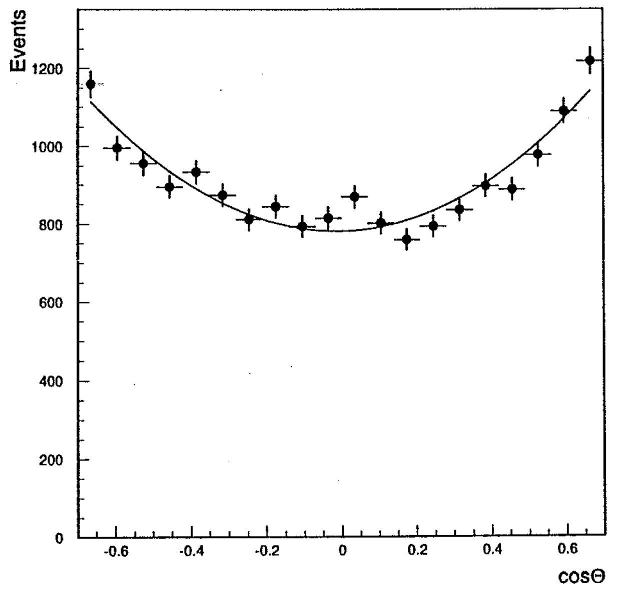

Figure 6.12: Distribution of cosine of the scattering angle θ for τ pair events at Z^0 peak. The dots represent the data and the solid line shows the results of the fit as described in the text.

We require, in our analysis, two jets with opposite charges. We can define the number of observed forward and backward events in terms of true forward (N_f) and true backward (N_b) events and the probability P of measuring wrong charge.

$$N_f^{observed} = (1-P)^2 N_f + P^2 N_b \tag{6.21}$$

$$N_b^{observed} = (1-P)^2 N_b + P^2 N_f$$

$$A_{FB} = A_{FB}^{observed}\left(1+\frac{2P^2}{1-2P}\right) \tag{6.22}$$

The error in the measurement of charge confusion translates into the systematic error of asymmetry measurement,

$$\Delta A_{FB} = A_{FB}^{observed}\frac{4P(1-P)}{(1-2P)^2}\,\delta P \tag{6.23}$$

We determine the charge confusion probability from the events which contain at least one muon and check whether the charge of the muon measured in the muon chamber agrees with that measured in the tracking chamber. Since the large muon chamber has a better momentum resolution, this measurement has negligible charge confusion compared to the corresponding measurement in TEC. From the events where the charge measured in muon chamber does not agree with that in TEC, we determine the charge confusion probability P as (3.12±0.07)%.

Background

For asymmetry measurements, we restrict our fiducial volume $|\cos\Theta_{\text{thrust}}| < 0.70$ to minimise background. The forward backward asymmetry is corrected for the remaining background.

6.5.3 Systematic Errors on A_{FB}

- The systematic error from charge confusion is less than 0.001 A_{FB}^{τ}.
- Background correction introduces a systematic error of 0.003.
- We calculate the forward backward asymmetry by defining the event angle from polar angle of the most energetic jet. The asymmetry determined from this method differs from the original method by 0.001. We attribute this to the systematic error.

The corrected asymmetries together with the statistical and systematic errors are summarised in table 6.6.

Year	$\sqrt{s}$	A_{FB}^{τ}	Stat. Err.	Syst. Err.
1992	91.293	0.013	0.012	0.003
1994	91.218	0.009	0.008	0.003
1995 prescan	91.160	0.003	0.024	0.003
1995 scan	89.452	-0.181	0.033	0.003
	91.293	-0.016	0.028	0.003
	92.984	0.152	0.026	0.003

Table 6.6: Forward Backward Asymmetry for different data sets

The measured forward backward asymmetry is plotted as a function of the centre of mass energy in figure 6.13. The solid line represents the distribution as expected from Standard Model calculated from ZFITTER using Z^0 mass of 91.186 GeV, top quark mass of 175 GeV, Higgs mass of 300 GeV and α_s of 0.123. The difference of the measured value with the predicted values are plotted at the bottom part of the figure.

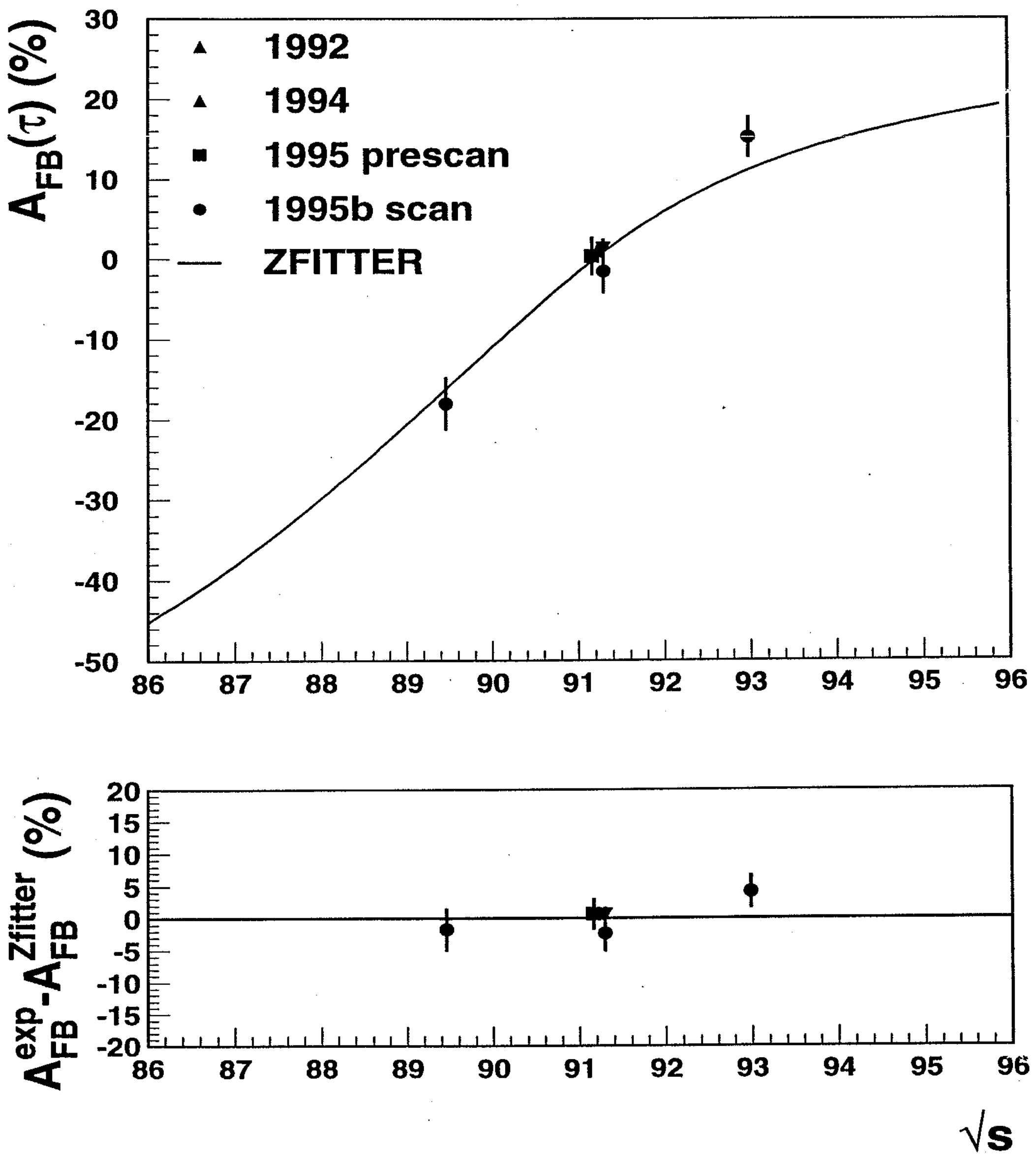

Figure 6.13: The measured forward backward asymmetries at different $\sqrt{s}$ values. The solid line shows the prediction of the Standard Model. The lower plot displays the difference of the measured and the Standard Model asymmetry values in (%).

Chapter 7

Electroweak Parameters Using L3 Data

7.1 Introduction

The Glashow-Salam-Weinberg model of electroweak interaction together with quantum chromodynamics constitutes the Standard Model of particle physics. At LEP, we study the process $e^+e^- \rightarrow f\bar{f}$, which is mediated by the Z^0 and γ as described in the Standard Model. Experimentally we measure the cross sections of hadronic and leptonic final states, leptonic forward backward asymmetries and polarisation as a function of the centre of mass energy. These measurements are used as input for the determination of the electroweak parameters.

For a precise determination of the electroweak parameters higher order corrections to the lowest order processes should be taken into account. The higher order corrections are divided as : (1) QED correction consisting of diagrams with real or virtual photons, (2) Weak corrections consisting of propagator correction, vertex correction and box diagram corrections, and (3) QCD corrections which include emission of gluons in case of hadronic final states. The process $e^+e^- \rightarrow f\bar{f}$ and the aspects of the radiative corrections are described in chapter 2.

Cross section data enable us to determine the mass (M_Z), total (Γ_Z) and partial widths (Γ_f) of Z^0 boson while inclusion of asymmetry and polarisation data provides the knowledge about the vector and axial vector couplings of Z^0 to the fermion pairs. Fit to determine the Z^0 parameters from cross section and asymmetry data is known as *line-shape fit*. We follow two different approaches to determine electroweak parameters from our measurements.

Model Independent Framework : we determine mass, total and partial widths of Z^0 from the data where the Standard Model predictions of the parameters are not imposed in the fit explicitly. The QED corrections and the energy dependent Breit-

Wigner shape of the cross sections as a function of centre of mass energy are considered. The weak corrections are not considered explicitly, but are absorbed in the definition of the parameters, which are interpreted as effective parameters. This is possible because the weak corrections can be separated from the QED corrections. Effective vector and axial vector couplings and effective electroweak mixing angle are also determined here when forward backward asymmetry measurements are used.

Standard Model Framework : we estimate M_Z, M_t, M_H and α_s from the data. In this case QED as well as weak radiative corrections are taken into account.

We use the analytical program ZFITTER [66] for calculating the theoretical predictions for the cross sections and asymmetries. This program takes into account electroweak radiative corrections to order $\mathcal{O}(\alpha)$ and a common exponentiation of initial and final state bremsstrahlung. The corrections to $\mathcal{O}(\alpha^2)$ are taken into account in the leading log approximation and include the production of photons and fermion pairs in the initial state. $\mathcal{O}(\alpha)$ and $\mathcal{O}(\alpha^2)$ corrections are supplemented with $\mathcal{O}(\alpha^2 {M_t}^4)$ corrections in gauge boson self energies. It also includes $\mathcal{O}(\alpha\alpha_s)$ corrections and leading part of $\mathcal{O}(\alpha\alpha_s {M_t}^2)$ corrections. It calculates cross sections and asymmetries in two ways. (a) In the first method cross sections are calculated in terms of the 4 input parameters as M_Z, Γ_Z, Γ_e and Γ_f (where $f(\bar{f})$ denote the final state fermion (antifermion)). For the calculation of the forward backward asymmetries one needs to specify the initial state and final state effective couplings. (b) In the second method if a set of values for M_Z, M_t, M_H, α_s are specified it calculates the weak radiative corrections to widths and the couplings according to Standard Model and then calculates the cross section and asymmetries.

For the process $e^+e^- \to e^+e^-$ we have, in addition to s channel, contributions from t channel and, s and t interference terms. For the calculation of t and s-t interference terms we use another program ALIBABA [67]. This program works within the framework of Standard Model. ALIBABA takes much longer time for the calculation of cross section and asymmetry and is not suitable to use in the fit. We calculate the t-channel and the s–t channel interference contributions at the beginning of the fit from ALIBABA. The contribution from s-channel is calculated using ZFITTER and varied during the fit.

The CERN library package MINUIT [68] is used for minimisation purpose.

(The contribution of the author in this chapter is in the extraction of the electroweak parameters from L3 data.)

7.2 Fitting Method

Experimental measurements have uncertainties from different sources – statistical error, systematic error, luminosity error and error from LEP energy measurement. It is necessary to take into account all these errors and their correlations properly in the lineshape fit. We use error matrix method to define the χ^2 of the fit in the following way,

$$\chi^2 = \Delta^T V^{-1} \Delta \quad , \tag{7.1}$$

where Δ is a column matrix of dimension n containing the differences between measured values and the theoretical predictions corresponding to n measurements and V is the n $\times$ n error correlation matrix containing the uncertainties of the measurements and the correlation between different measurements. The diagonal terms of the correlation matrix contain the quadratic sum of all the errors for a particular measurement and the off diagonal terms contain the correlated systematic errors between different measurements [69].

7.2.1 Measurement Errors

Statistical Error

Statistical error is directly related to the number of selected events and is uncorrelated between individual measurements. The statistical error obtained from number of selected events is scaled by the number of events expected from theory to avoid large fluctuation in data in the following way,

$$\begin{aligned}(\delta^{\mathrm{stat}})_{\mathrm{cross\,section}} &= \delta^{\mathrm{expt}} \frac{\sigma_{\mathrm{expt}}}{\sigma_{\mathrm{theo}}} \sqrt{\frac{N_{\mathrm{expt}}}{N_{\mathrm{theo}}}} \\ &= \delta^{\mathrm{expt}} \sqrt{\frac{\sigma_{\mathrm{theo}}}{\sigma_{\mathrm{expt}}}} \end{aligned} \tag{7.2}$$

$$(\delta^{\mathrm{stat}})_{\mathrm{asymmetry}} \simeq \delta^{\mathrm{expt}} \sqrt{\frac{1-(A_{FB}^{\mathrm{theo}})^2}{1-(A_{FB}^{\mathrm{expt}})^2}} \tag{7.3}$$

where N_{expt} is the number of events found experimentally and N_{theo} is the number of events expected from theory ; σ_{expt} and σ_{theo} are experimental and theoretical cross sections respectively and δ^{expt} is the statistical error from measurements.

Systematic Error

Systematic error in the measurement of cross section arises from different sources like selection criteria, trigger, limited sample of Monte Carlo events etc., as described in chapter 6. Systematic errors in cross section and asymmetry measurements of different decay channels of Z^0 are treated as uncorrelated. For individual channels it is fully correlated between different energy points and data sets of individual years. But the systematic error in cross section and asymmetry is uncorrelated for each decay channels.

Luminosity Error

The systematic error in the luminosity measurement is referred as luminosity error. Measured luminosity is used in the cross section measurement for all the channels in the same way. Hence, the luminosity error is fully correlated between all cross section measurements. Forward backward asymmetry being a ratio of two quantities, is independent of the luminosity. As a result, the luminosity error does not affect the measured asymmetry.

LEP Energy Uncertainty

The uncertainty in the measurement of LEP energy and the correlation between energy points should be translated in the error correlation matrix properly [70]. It has different parts as following

- Absolute energy error $(\frac{\Delta E}{E})_{abs}$: The systematic error in the calibration method is called the absolute energy error. This is estimated by the resonant depolarisation method at the calibration energy E_{cal}. Energy points in a calibration period which are extrapolated from the same reference points are fully correlated and the energy points of different years which are calibrated by the same method are also correlated. In all other cases the absolute energy error is uncorrelated.

- Local Energy Error $(\frac{\Delta E}{E})_{local}$: The local energy E_{loc} is measured by the flux loop method. The systematic error in the local energy scale is the measure of the systematic error in the extrapolation method. This error is always correlated as the extrapolation method is always same and is proportional to the difference between E_{loc} and E_{cal}. Energy points which are on the same side of the reference point are positively correlated whereas points on opposite side are negatively correlated.

- Point to Point Error $(\frac{\Delta E}{E})_{p-t-p}$: This error is uncorrelated between energy points and consists of two parts: setting error and non-reproducibility error. The setting error accounts for the higher order effects in the relation between beam energy and field display. This is zero at the reference point. The non reproducibility error takes into account the tidal effects, reproducibility in the field display, temperature corrections etc. This decreases with the number of fills at the energy point.

The total energy error at an energy point is the quadratic sum of all the errors described above. The error on energy point, ΔE, is converted to the error on cross section and asymmetry in the following [73] way,

$$\delta^{LEP} = \Delta E \frac{\partial X}{\partial E} \tag{7.4}$$

where X denotes the measured quantity, cross section or asymmetry, and $\frac{\partial X}{\partial E}$ is the variation with respect to centre of mass energy.

7.2.2 Effect of Beam Energy Spread

The measured LEP beam energy has a Gaussian distribution with a certain standard deviation duc to synchrotron radiation. This spread affects the measured cross sections. The non-vanishing contribution comes due to the non-linearity of cross section with energy. The effect of the energy spread on the cross section is calculated by convoluting the cross section over a Gaussian around the given energy point. The change in the cross section is estimated as (detailed calculations are given in Appendix A),

$$\delta\sigma \cong -\frac{1}{2}\frac{\mathrm{d}^2\,\sigma}{\mathrm{dE}^2}\omega^2 \tag{7.5}$$

Where ω is the standard deviation of the beam energy spread. The effect of convolution is different for peak and off peak points. Peak cross sections are lowered and the off peak ones are raised. Hence the overall shape of the lineshape curve changes. This affects the total width but mass is not affected as it is symmetric with respect to the peak position.

The theoretical predictions are corrected for this effect by a factor known as *Beam Spread Factor*. If σ is the cross section at a particular centre of mass energy point and $\sigma_{\text{convoluted}}$ is the convoluted cross section for the energy spread then we define

$$\text{Beam Spread Factor} = \frac{\sigma}{\sigma_{\text{convoluted}}} \tag{7.6}$$

The effect on hadronic cross section due to beam spread is 0.15%. The beam spread does not affect the forward backward asymmetry as it is a ratio of cross sections.

The beam energy spread has an uncertainty which is correlated among the energy points and gives rise to error on the beam spread factors. This is also taken care of in the error correlation matrix. The beam energy spread for different years and the corresponding beam spread factors are listed in Table 7.1.

7.2.3 Special Treatment of $\mathrm{e^+e^-} \to \mathrm{e^+e^-}$

The process $\mathrm{e^+e^-} \to \mathrm{e^+e^-}$ has contributions coming from γ and $\mathrm{Z^0}$ exchanges in s-channel, t-channel and the s–t interference. The theoretical prediction for the s-channel exchange is estimated using the program ZFITTER as it takes much less time compared to ALIBABA. The contributions from the t-channel and s–t interference terms are calculated using the program ALIBABA. ALIBABA uses Monte Carlo integration which is extremely time consuming and hence difficult to use in the fitting process. So calculation of t and s–t interference terms are performed only once at the beginning of the fit. We define the total cross section for the process under consideration as [71, 72]

$$\sigma^{\text{tot}}_{\mathrm{e^+e^-}} = \sigma^{\text{t+i}}_{\text{ALI}} + \mathrm{R}\cdot\sigma^{\text{s}}_{\text{ZF}} \tag{7.7}$$

period	$\sqrt{s}$	Energy Spread (MeV)	Beam Spread Factors			
			hadrons	e^+e^-	$\mu^+\mu^-$	$\tau^+\tau^-$
1990	88.232	51 ± 5	0.9994233	0.9997595	0.9994690	0.9994579
	89.236	51 ± 5	0.9991369	0.9995670	0.9991737	0.9991649
	90.237	51 ± 5	0.9994520	0.9998392	0.9994643	0.9994598
	91.230	51 ± 5	1.0014177	1.0012249	1.0014009	1.0014051
	92.226	51 ± 5	0.9997446	0.9994977	0.9997495	0.9997537
	93.228	51 ± 5	0.9995165	0.9994690	0.9995304	0.9992837
	94.223	51 ± 5	0.9996811	0.9996628	0.9996921	0.9996889
1991	91.253	51 ± 5	1.0014120	1.0012174	1.0013949	1.0013991
	88.480	51 ± 5	0.9993570	0.9997213	0.9994013	0.9993907
	89.470	51 ± 5	0.9990893	0.9995480	0.9991225	0.9991144
	90.228	51 ± 5	0.9994388	0.9998304	0.9994500	0.9994469
	91.222	51 ± 5	1.0014187	1.0012263	1.0014018	1.0014061
	91.967	51 ± 5	1.0001025	0.9998357	1.0001066	1.0001063
	92.966	51 ± 5	0.9994874	0.9994229	0.9994998	0.9994967
	93.716	51 ± 5	0.9995969	0.9996467	0.9996104	0.9996073
1992	91.294	51 ± 5	1.0013907	1.0011603	1.0013742	1.0013791
1993	91.316	55 ± 1.1	1.0015993	1.0014118	1.0015805	1.0015819
	89.449	55 ± 1.1	0.9989593	0.9992175	0.9989970	0.9989879
	91.203	55 ± 1.1	1.0016737	1.0016671	1.0016541	1.0016589
	93.033	55 ± 1.1	0.9993883	0.9993898	0.9994114	0.9994070
1994	91.218	55 ± 1.1	1.0016439	1.0015187	1.0016248	1.0016294
1995	89.452	55 ± 1.3	0.9989435	0.9989914	0.9989817	0.9989726
	91.293	55 ± 1.3	1.0016499	1.0012441	1.0016350	1.0016382
	92.984	55 ± 1.3	0.9993820	0.9991468	0.9993986	0.9993921

Table 7.1: The beam energy spreads with their uncertainties and the corresponding beam spread factors for different final states.

where σ^{t+i}_{ALI} is the contribution to cross section from t and s-t interference terms calculated using ALIBABA, σ^{s}_{ZF} is the contribution from s-channel calculated using ZFITTER.

R Factor : Experimentally we measure the total cross section $\sigma_{e^+e^-}$, where we restrict both e^+ and e^- within the polar angular range $44^\circ - 136^\circ$. The programme ALIBABA is able to calculate cross section with polar angular cuts on both e^+ and e^-, while the programme ZFITTER calculates s-channel cross section with polar angular cut only on e^-. To make s-channel cross section compatible with experimental cuts on both e^+ and e^-, we multiply σ^{s}_{ZF} by a factor R which is calculated using the programme ALIBABA and is defined as,

$$R = \frac{\sigma^{s}_{ALI}(e^+e^- \text{both in } 44^\circ - 136^\circ)}{\sigma^{s}_{ALI}(e^- \text{ in } 44^\circ - 136^\circ, e^+ \text{ in } 0^\circ - 180^\circ)} \tag{7.8}$$

Similar treatment is done for the forward backward asymmetry and details are given in Appendix B.

These factors R, σ^{t+i}_{ALI} are calculated at different centre of mass energy points using ALIBABA. The systematic difference of the two programs ZFITTER and ALIBABA are also studied. The statistical fluctuation in the Monte Carlo calculation in ALIBABA and the systematic difference between these two programs are taken into account introducing additional systematic error of 0.2% on electron cross section and 0.002 on Asymmetry. For other processes this complication does not arise as they have only s-channel contribution.

7.3 Experimental Data

Experimental data used for the determination of Z-parameters are :

(a) cross section measurements for the following,

$$\begin{aligned} e^+e^- &\longrightarrow \text{hadrons} \\ &\longrightarrow e^+e^- \\ &\longrightarrow \mu^+\mu^- \\ &\longrightarrow \tau^+\tau^- \end{aligned} \tag{7.9}$$

(b) forward backward asymmetry measurements for the leptonic final states,

$$\begin{aligned} e^+e^- &\longrightarrow e^+e^- \\ &\longrightarrow \mu^+\mu^- \\ &\longrightarrow \tau^+\tau^- \end{aligned} \tag{7.10}$$

Detailed procedure for event selection of $e^+e^- \to \tau^+\tau^-$, calculation of cross section and measurement of asymmetry are described in Chapter 6. Similar procedure was used by the

L3 collaboration for the determination of cross section and asymmetries for other channels. (The contribution of the author is in the determination of cross section and asymmetry for $e^+e^- \rightarrow \tau^+\tau^-$ using 1995 data; rest of the numbers are taken from L3 collaboration.) The measured values of the cross sections and asymmetries are summarised in tables 7.2, 7.3 and 7.4 for different years. The measurements from 1990–1992 are already published [61] whereas the results for the years 1993, 1994 and 1995 are *preliminary.* The quoted cross sections are the total cross sections extrapolated to the full solid angle of 4π except for the process $e^+e^- \rightarrow e^+e^-$. These numbers are used as inputs to the analysis described in Section 7.4.

Period	$\sqrt{s}$ (GeV)	σ_{had} (nb)	Stat. Err. (nb)	Syst. Err. (nb)	σ_e (nb)	Stat. Err. (nb)	Syst. Err. (nb)
1990	88.232	4.455	0.118	0.013	0.334	0.030	0.001
	89.236	8.523	0.149	0.026	0.533	0.034	0.002
	90.237	18.689	0.261	0.056	0.896	0.050	0.004
	91.230	30.405	0.125	0.091	1.052	0.019	0.004
	92.226	22.014	0.272	0.066	0.716	0.043	0.003
	93.228	12.383	0.172	0.037	0.406	0.029	0.002
	94.223	8.058	0.138	0.024	0.223	0.022	0.001
1991	91.253	30.410	0.097	0.046	1.032	0.014	0.003
	88.480	5.223	0.086	0.008	0.405	0.023	0.001
	89.470	10.157	0.121	0.015	0.575	0.026	0.002
	90.228	18.225	0.179	0.027	0.794	0.032	0.002
	91.222	30.286	0.129	0.045	1.067	0.019	0.003
	91.967	24.636	0.242	0.037	0.800	0.033	0.002
	92.966	14.451	0.160	0.022	0.423	0.024	0.001
	93.716	10.103	0.126	0.015	0.304	0.019	0.001
1992	91.294	30.408	0.047	0.046	1.054	0.007	0.003
1993	91.316	30.544	0.092	0.016	1.015	0.014	0.003
	89.449	10.076	0.037	0.006	0.567	0.008	0.002
	91.203	30.182	0.069	0.016	1.075	0.011	0.003
	93.033	13.886	0.044	0.008	0.432	0.007	0.002
1994	91.218	30.391	0.032	0.016	1.072	0.005	0.002
1995	89.452	10.077	0.039	0.011	0.560	0.009	0.006
	91.293	30.380	0.102	0.031	1.064	0.016	0.011
	92.984	14.202	0.047	0.015	0.429	0.008	0.004

Table 7.2: Measured values of the Cross sections of $e^+e^- \rightarrow$ hadrons and $e^+e^- \rightarrow e^+e^-$ with statistical and systematic errors. The measurements from 1990-1992 are published and 1993-1995 are *preliminary.*

Period	$\sqrt{s}$ (GeV)	σ_μ (nb)	Stat. Err. (nb)	Syst. Err. (nb)	σ_τ (nb)	Stat. Err. (nb)	Syst. Err. (nb)
1990	88.232	0.268	0.033	0.002	0.219	0.036	0.002
	89.236	0.388	0.038	0.003	0.445	0.048	0.004
	90.237	0.931	0.063	0.007	0.912	0.078	0.008
	91.230	1.476	0.028	0.012	1.470	0.034	0.013
	92.226	1.116	0.066	0.009	1.097	0.080	0.010
	93.228	0.506	0.040	0.004	0.592	0.051	0.005
	94.223	0.405	0.036	0.003	0.411	0.042	0.004
1991	91.253	1.508	0.021	0.008	1.505	0.025	0.011
	88.480	0.259	0.022	0.001	0.236	0.024	0.002
	89.470	0.486	0.029	0.002	0.532	0.035	0.004
	90.228	0.871	0.040	0.004	0.886	0.047	0.006
	91.222	1.391	0.026	0.007	1.447	0.032	0.010
	91.967	1.190	0.050	0.006	1.226	0.059	0.009
	92.966	0.718	0.037	0.004	0.642	0.041	0.004
	93.716	0.478	0.029	0.002	0.535	0.036	0.004
1992	91.294	1.464	0.010	0.007	1.470	0.012	0.010
1993	91.316	1.498	0.021	0.005	1.486	0.021	0.009
	89.449	0.503	0.010	0.002	0.508	0.010	0.005
	91.203	1.476	0.016	0.005	1.468	0.017	0.010
	93.033	0.682	0.012	0.002	0.716	0.012	0.005
1994	91.218	1.478	0.007	0.005	1.466	0.007	0.010
1995	89.452	0.494	0.011	0.005	0.489	0.012	0.004
	91.293	1.474	0.027	0.015	1.517	0.030	0.009
	92.984	0.710	0.012	0.007	0.682	0.013	0.005

Table 7.3: Measured values of the Cross sections of $e^+e^- \to \mu^+\mu^-$ and $e^+e^- \to \tau^+\tau^-$ with statistical and systematic errors. The measurements from 1990-1992 are published and 1993-1995 are *preliminary.*

Period	$\sqrt{s}$ (GeV)	A^e_{FB}	Stat. Err.	Syst. Err.	A^μ_{FB}	Stat. Err.	Syst. Err.	A^τ_{FB}	Stat. Err.	Syst. Err.
1990	88.232	0.520	0.095	0.004	-0.391	0.117	0.005	-0.356	0.199	0.005
	89.236	0.296	0.070	0.004	-0.044	0.109	0.005	-0.004	0.146	0.005
	90.237	0.155	0.064	0.004	-0.184	0.074	0.005	-0.126	0.106	0.005
	91.230	0.101	0.021	0.004	0.006	0.021	0.005	0.077	0.028	0.005
	92.226	0.040	0.069	0.004	0.110	0.066	0.005	0.091	0.089	0.005
	93.228	0.083	0.081	0.004	0.095	0.091	0.005	0.073	0.106	0.005
	94.223	0.144	0.118	0.004	0.134	0.099	0.005	0.043	0.134	0.005
1991	91.253	0.110	0.016	0.004	0.028	0.014	0.002	0.037	0.021	0.005
	88.480	0.384	0.063	0.004	-0.197	0.097	0.002	-0.106	0.128	0.005
	89.470	0.333	0.051	0.004	-0.191	0.063	0.002	-0.152	0.084	0.005
	90.228	0.253	0.046	0.004	-0.101	0.050	0.002	-0.137	0.070	0.005
	91.222	0.125	0.022	0.004	-0.002	0.020	0.002	-0.032	0.029	0.005
	91.967	0.167	0.048	0.004	0.058	0.043	0.002	0.042	0.063	0.005
	92.966	0.070	0.066	0.004	0.117	0.056	0.002	0.161	0.079	0.005
	93.716	0.150	0.074	0.004	0.089	0.065	0.002	0.058	0.082	0.005
1992	91.294	0.104	0.007	0.023	0.007	0.007	0.002	0.015	0.010	0.003
1993	91.316	0.083	0.016	0.003	0.009	0.015	0.001	-0.003	0.017	0.003
	89.449	0.316	0.016	0.003	-0.182	0.020	0.001	-0.138	0.022	0.003
	91.203	0.111	0.012	0.003	-0.001	0.011	0.001	0.020	0.013	0.003
	93.033	0.101	0.019	0.003	0.119	0.017	0.001	0.133	0.019	0.003
1994	91.218	0.122	0.005	0.003	0.008	0.005	0.001	0.008	0.005	0.003
1995	89.452	0.298	0.017	0.010	-0.201	0.024	0.005	-0.181	0.033	0.003
	91.293	0.105	0.018	0.010	0.015	0.020	0.005	-0.016	0.028	0.003
	92.984	0.061	0.021	0.010	0.112	0.019	0.005	0.152	0.027	0.003

Table 7.4: Measured values of the forward backward asymmetries for leptonic decays of Z^0. The statistical and systematic errors are given in the table for individual channels. The measurements from 1990-1992 are published and 1993-1995 are *preliminary*.

7.4 Determination of Z^0 parameters in Model Independent Method

In the model independent method, fits are performed with minimum assumptions of the Standard Model. In this method initial and final state QED corrections and the energy dependent Breit-Wigner shape of the Z^0 resonance are taken into account. At the Z^0 peak it is possible to separate out the QED corrections from the weak corrections and the model independent method utilises this fact. In this method weak corrections are not applied directly. The vector and axial vector couplings of Z^0 to fermions are redefined in order to absorb the weak corrections in the definition itself. The couplings, which are determined from the fit, are the effective couplings as described in Section 2.3.2. The γZ interference term is fixed to its standard model prediction in this method.

7.4.1 Mass and Decay Widths of Z^0 Boson

Mass of Z^0 boson, its total width and the partial widths are determined from the measurements of cross sections of different final states given in equations (7.9).

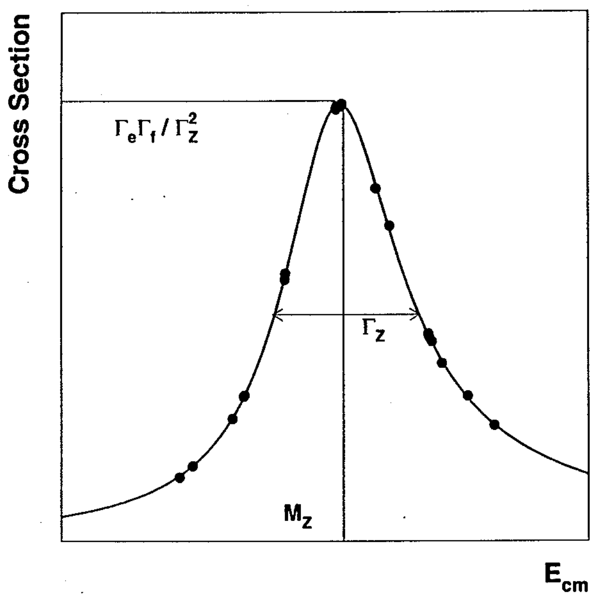

Figure 7.1: Schematic diagram of lineshape fit

The values of cross sections as a function of centre of mass energies give rise to the well known Z^0 lineshape distribution as shown schematically in fig 7.1. The position of the peak determines the mass of the Z^0 boson (M_Z). The height is proportional to the product of initial and final state partial widths ($\frac{12\pi}{M_Z{}^2}\frac{\Gamma_e\Gamma_f}{\Gamma_Z{}^2}$) and the full width at half maximum determines the total width of Z^0 (Γ_Z).

Parameter	Treatment of Leptons		Standard Model
	non-universality	universality	
M_Z (MeV)	91 188.1±2.9	91 188.1±2.9	—
Γ_Z (MeV)	2 499.8±4.3	2 499.8±4.3	2 495.7
Γ_{had} (MeV)	1 745.2±5.5	1 745.6±4.2	1 742.8
Γ_e (MeV)	83.99±0.26	—	
Γ_μ (MeV)	83.78±0.47	—	
Γ_τ (MeV)	84.10±0.62	—	
Γ_{lept} (MeV)	—	83.98±0.19	83.92
χ^2/DOF	88/90	89/92	—
Γ_{inv} (MeV)		502.5±3.4	501.4
N_ν		3.001±0.017	3

Table 7.5: Results of the fits to the 1990-95 cross section data with and without assuming lepton universality. The Z^0 resonance is parametrised using a Breit-Wigner with constant γZ interference term. The last column of the table contains the predictions for the widths using M_t = 175 GeV, M_H = 300 GeV and α_s = 0.123. DOF stands for the degrees of freedom.

Performing a simultaneous fit to all the four cross sections, one can determine 6 parameters which are mass, total width and the four partial widths of Z^0. The results of the fit are listed in the second column of table 7.5. The measured values of cross sections as a function of the centre of mass energy is shown in figures 7.2–7.5. The result of the fit is shown by the solid line in each figures. Quality of the fit can be gauged in two ways: (a) from the ratio of measured cross sections to the fitted values ($\sigma_{meas}/\sigma_{fit}$) for all the points as a function of centre of mass energy and is shown in the bottom part of the figures 7.2–7.5 and (b) from the value of χ^2/(degrees of freedom), listed in table 7.5, which is ≈ 1.

It is seen from the table 7.5 that three leptonic partial widths are the same within error. It may be mentioned that the phase space effect on $Z^0 \to \tau^+\tau^-$ due to the heavy mass of τ lepton compared to the mass of μ/e is to decrease Γ_τ by 0.2 MeV ($\delta\Gamma_\tau$).

One can improve upon the leptonic partial width assuming lepton universality (i.e assuming $\Gamma_e = \Gamma_\mu = \Gamma_\tau$). The results of the fit assuming lepton universality is listed in the third column for table 7.5 where Γ_{lept} refers to the partial width of Z^0 to a pair of massless leptons. The last column of the table gives the expected values of the widths from the Standard Model which is calculated using M_t= 175 GeV, M_H = 300 GeV and α_s= 0.123. The values in good agreement with our results.

The mass and total width of Z^0 are obtained as

$$\begin{aligned} M_Z &= 91188.1 \pm 2.9 \text{ MeV} \\ \Gamma_Z &= 2499.8 \pm 4.3 \text{ MeV} \end{aligned}$$

The error on M_Z and Γ_Z has significant contribution from LEP energy error. This is estimated by performing lepton universality fit to the data with and without LEP energy uncertainty. The two sets of errors obtained this way are subtracted in quadrature to get the contribution of LEP energy error on these two parameters. The errors on M_Z and Γ_Z due to LEP energy uncertainty is given by

$$\begin{aligned}\Delta M_Z(\mathrm{LEP}) &= 1.5\ \mathrm{MeV}\\ \Delta\Gamma_Z(\mathrm{LEP}) &= 1.4\ \mathrm{MeV}\end{aligned}$$

The error on Γ_Z due to the uncertainty on beam energy spread is negligible.

7.4.2 Invisible Width and Number of Neutrinos

Z^0 also decays to light neutrinos which go undetected in the detector. The partial width of Z^0 due to the decay into this invisible mode is denoted by Γ_{inv} and is determined from the measured total and partial widths of Z^0 using the relation $\Gamma_{inv} = \Gamma_Z - \Gamma_{had} - \Gamma_e - \Gamma_\mu - \Gamma_\tau$. One can improve upon the Γ_{inv} assuming lepton universality. The invisible width is obtained in the following way,

$$\Gamma_{inv} = \Gamma_Z - \Gamma_{had} - 3\Gamma_{lept} + \delta\Gamma_\tau \tag{7.11}$$

From the parameters of the fit under the assumption of lepton universality listed in table 7.5, the invisible width is calculated taking into account the small correction of $\delta\Gamma_\tau$ due to tau mass in the universal lepton width and is given by,

$$\Gamma_{inv} = 502.5 \pm 3.4\ \mathrm{MeV} \tag{7.12}$$

The error on Γ_{inv} is calculated by propagating the errors in the Γ_Z, Γ_{had} and Γ_{lept} taking into account correlations between them. The correlation matrix is given in table 7.6.

	Γ_Z	Γ_{lept}	Γ_{had}
Γ_Z	1.000	0.663	0.609
Γ_{lept}	0.663	1.000	0.073
Γ_{had}	0.609	0.073	1.000

Table 7.6: Correlation matrix of Γ_Z, Γ_{lept} and Γ_τ

The number of light neutrino species is determined from the relation

$$N_\nu = \left(\frac{\Gamma_{inv}}{\Gamma_{lept}}\right) \cdot \left(\frac{\Gamma_{lept}}{\Gamma_\nu}\right)_{SM} \tag{7.13}$$

where Γ_ν is the partial width of Z^0 to neutrinos. The ratio $\frac{\Gamma_{lept}}{\Gamma_\nu}$ is taken from the Standard Model. One can also determine the number of neutrinos from the ratio $\frac{\Gamma_{inv}}{(\Gamma_\nu)_{SM}}$. But the

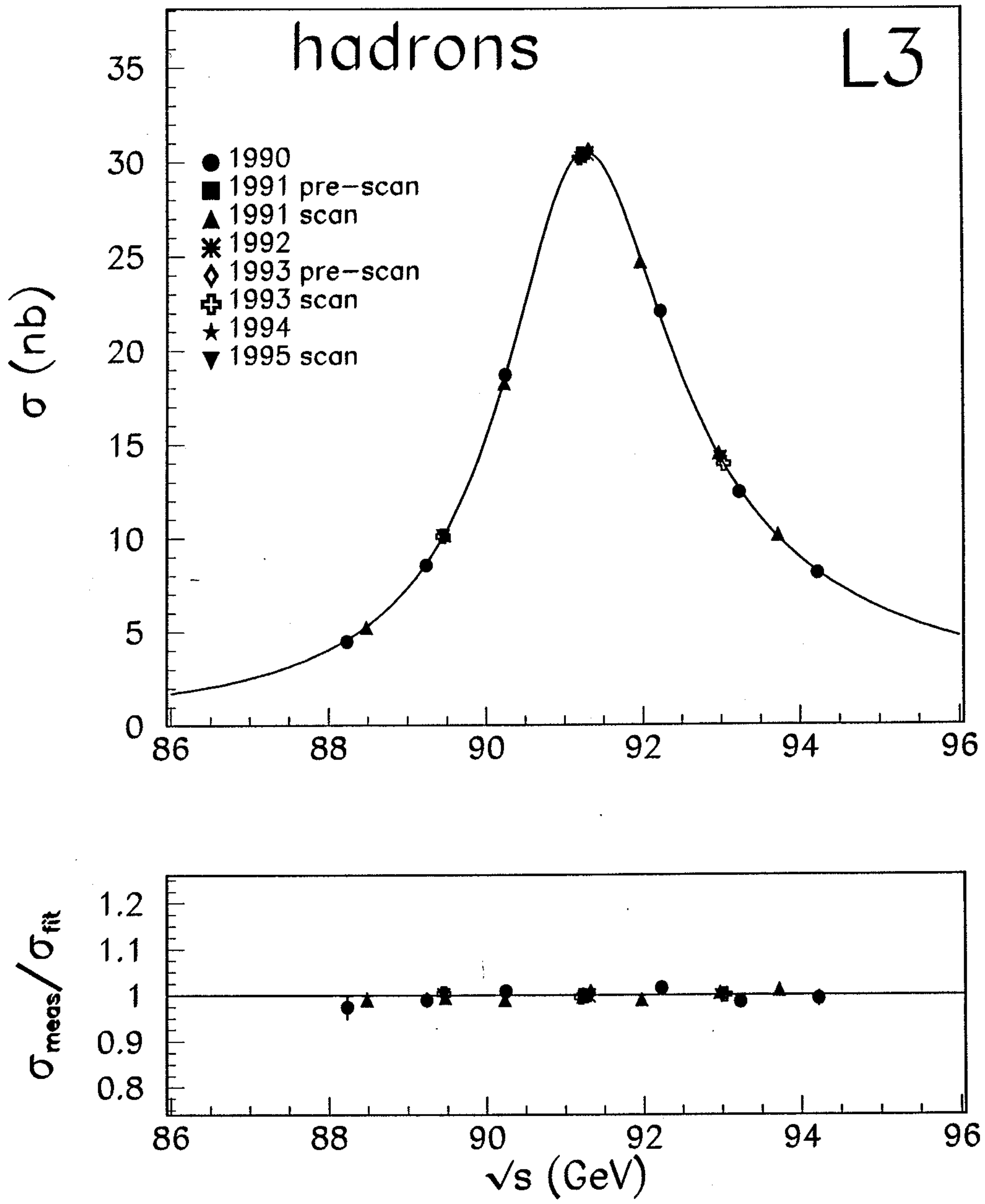

Figure 7.2: The measured cross section for $e^+e^- \rightarrow$ hadrons as a function of the centre of mass energy. The solid line shows the result of the fit. The bottom figure shows the ratio of the measured cross sections to the fitted values.

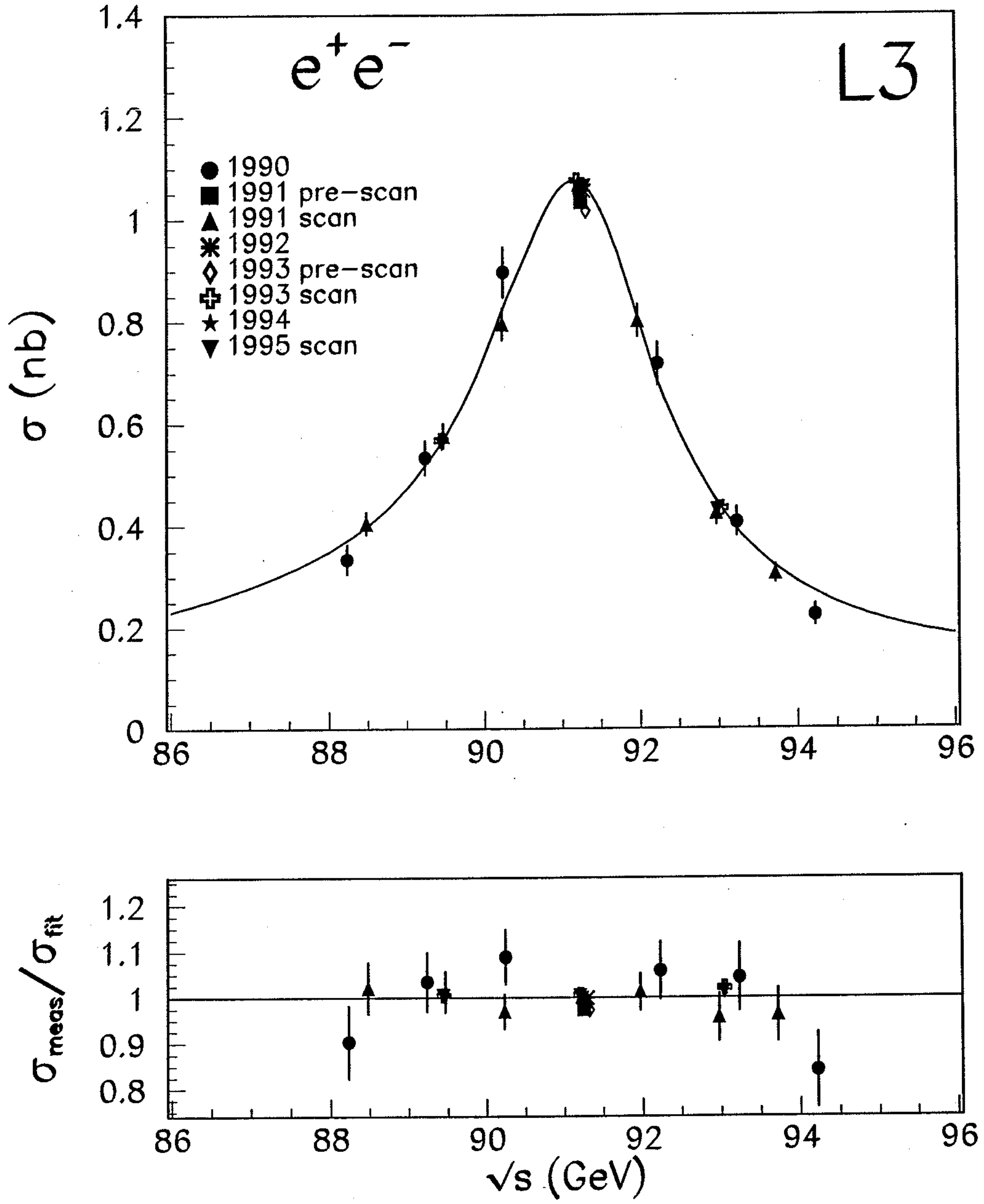

Figure 7.3: The measured cross section for $e^+e^- \to e^+e^-$ as a function of the centre of mass energy. The solid line shows the result of the fit. The bottom figure shows the ratio of the measured cross sections to the fitted values.

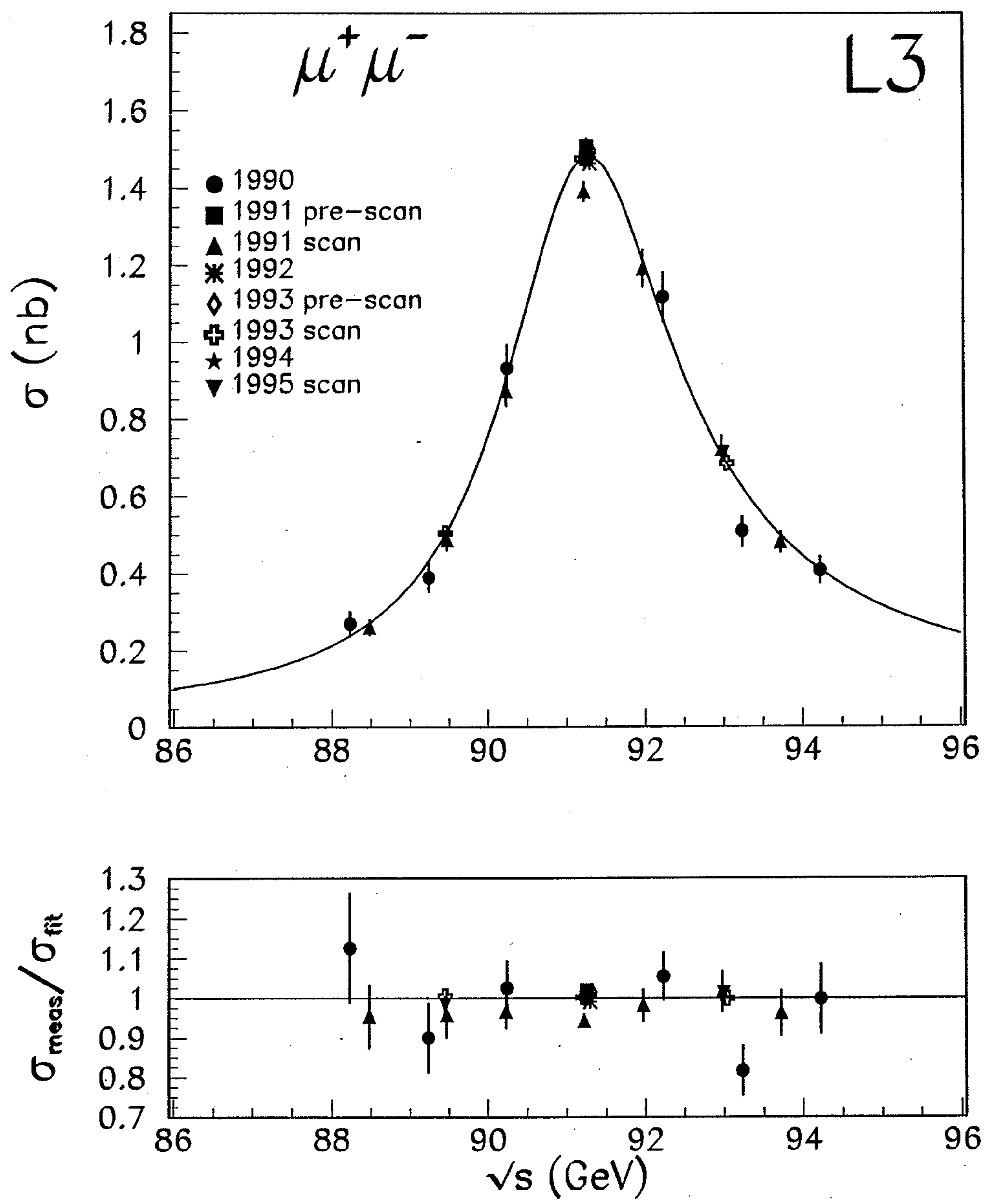

Figure 7.4: The measured cross sections for $e^+e^- \to \mu^+\mu^-$ as a function of the centre of mass energy. The solid line shows the result of the fit. The bottom figure shows the ratio of the measured cross sections to the fitted values.

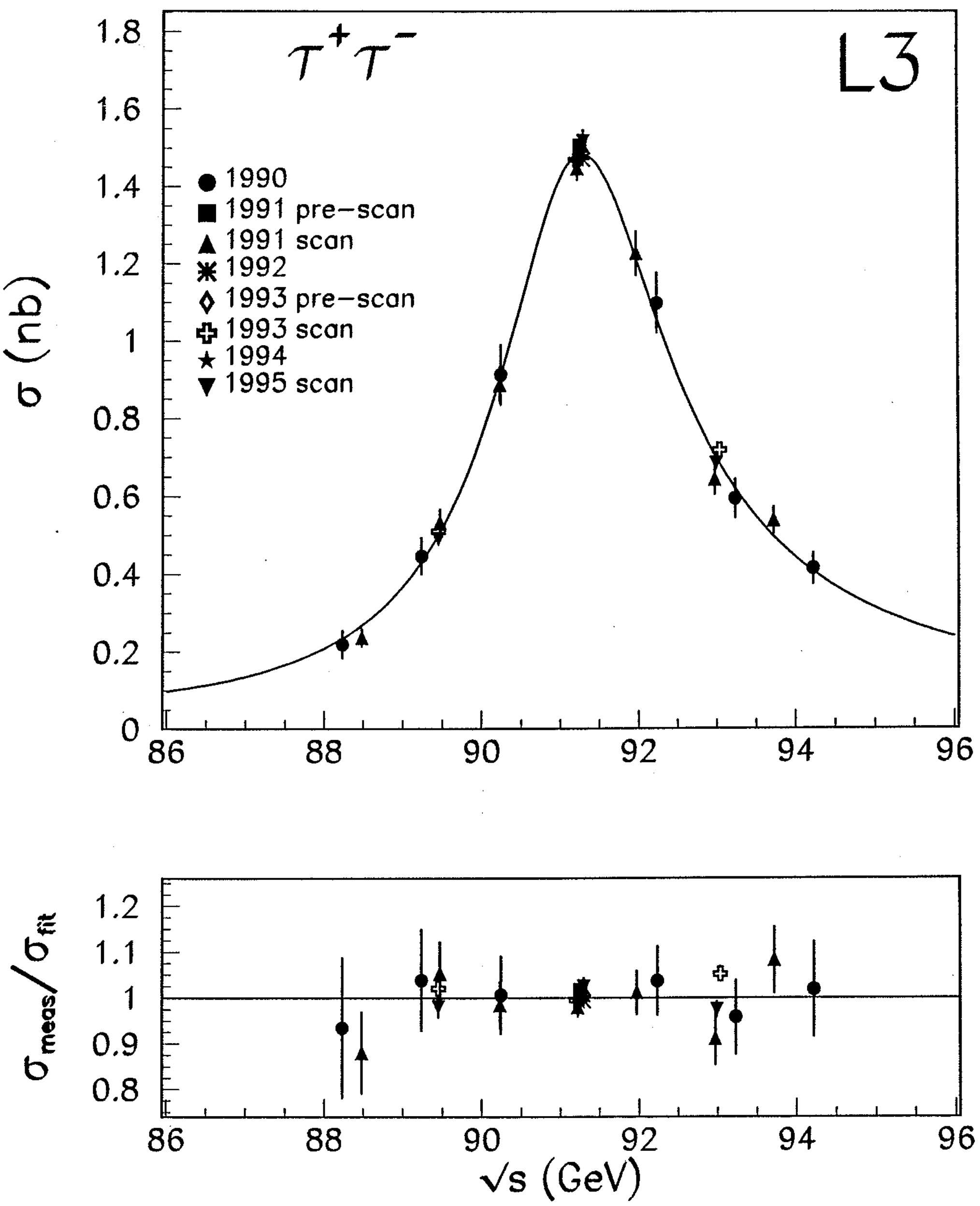

Figure 7.5: The measured cross section of $e^+e^- \to \tau^+\tau^-$ as a function of the centre of mass energy. The solid line shows the result of the fit. The bottom figure shows the ratio of the measured cross sections to the fitted values.

above relation (7.13) is used to minimise the dependence on the masses of top quark (M_t) and Higgs (M_H). The value of the ratio for top mass of 175 GeV and Higgs mass of 300 GeV is

$$\left(\frac{\Gamma_{\rm lept}}{\Gamma_\nu}\right)_{\rm SM} = 0.5018 \pm 0.0002 \qquad (7.14)$$

where the error accounts for the uncertainty of 6 GeV on M_t and the variation of M_H between 60−1000 GeV. Using this ratio from the Standard Model and the experimental measurements of $\Gamma_{\rm inv}$ and Γ_{lept}, the number of neutrinos is determined to be,

$$N_\nu = 3.001 \pm 0.017 \qquad (7.15)$$

Figure 7.6 shows the experimental data which is in agreement with the Standard Model prediction of three light neutrino generations. It may be mentioned that the experimental value of N_ν refers to the number of light neutrinos with masses less than $M_Z/2$.

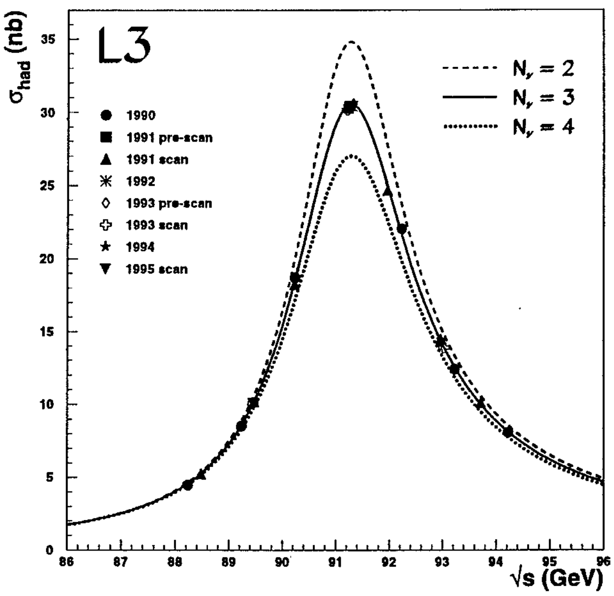

Figure 7.6: Measured hadronic cross sections are plotted with Standard Model predictions assuming 2,3 and 4 generations of light neutrino. The measurements are in excellent agreement with the prediction of three light neutrino generations.

7.4.3 9 and 5 Parameter Fits with $A_{FB}^{0,l}$ and R_l

Simultaneous fits are performed to the measured cross sections and leptonic forward backward asymmetries with the following parameters : the ratio of hadronic and leptonic partial widths $R_l(=\Gamma_{\rm had}/\Gamma_{lept})$, the hadronic pole cross section $\sigma^0_{\rm had}$ $(= \frac{12\pi}{M_Z{}^2}\frac{\Gamma_e\Gamma_{\rm had}}{\Gamma_Z{}^2})$, forward backward pole asymmetry $A_{FB}^{0,l}$. This set of parameters is sometimes preferred because the correlation between the parameters is small. These parameters are used for the combination of results from 4 LEP experiments. Results of fits with 9-parameters (lepton non universality) and with 5-parameters (lepton universality) are listed in table 7.7. Distributions of measured leptonic forward backward asymmetries as a function of the

Parameter	Treatment of Leptons		Standard Model
	non-universality	universality	
M_Z (MeV)	91 188.3±2.9	91 188.3±2.9	—
Γ_Z (MeV)	2 499.6±4.3	2 499.6±4.3	2 495.7
σ^0_{had} (nb)	41.411±0.074	41.411±0.074	41.453
R_e	20.78±0.11	—	
R_μ	20.84±0.10	—	
R_τ	20.75±0.14	—	
R_l	—	20.788±0.066	20.768
$A_{FB}^{0,e}$	0.0148±0.0063	—	
$A_{FB}^{0,\mu}$	0.0176±0.0035	—	
$A_{FB}^{0,\tau}$	0.0233±0.0049	—	
$A_{FB}^{0,l}$	—	0.0187±0.0026	0.0154
χ^2/DOF	142/159	144/163	

Table 7.7: Results of the fits to the 1990-95 cross section and forward-backward asymmetry measurements with and without assuming lepton universality. The last column represents the Standard Model predictions of these parameters using M_t = 175 GeV, M_H = 300 GeV and α_s = 0.123

centre of mass energy are given in figures 7.7–7.9 along with the fit results. The solid line represents the fit result. In the bottom part of each figure the difference between measured values of the asymmetry and the fitted values are plotted in percentage as a function of the centre of mass energy.

7.4.4 Strong Coupling Constant α_s

From the ratio $R_l = \Gamma_{had}/\Gamma_{lept}$ we can determine the strong coupling constant α_s. R_l can be written as,

$$R_l = R_l^0(1 + \delta_{QCD}) \qquad (7.16)$$

where R_l^0 is the value of the ratio R_l at $\alpha_s = 0$ and is calculated in the framework of the Standard Model.

The use of this ratio to estimate the strong coupling constant α_s has the advantage that weak corrections cancel out as they are same for leptons and hadrons but the QCD

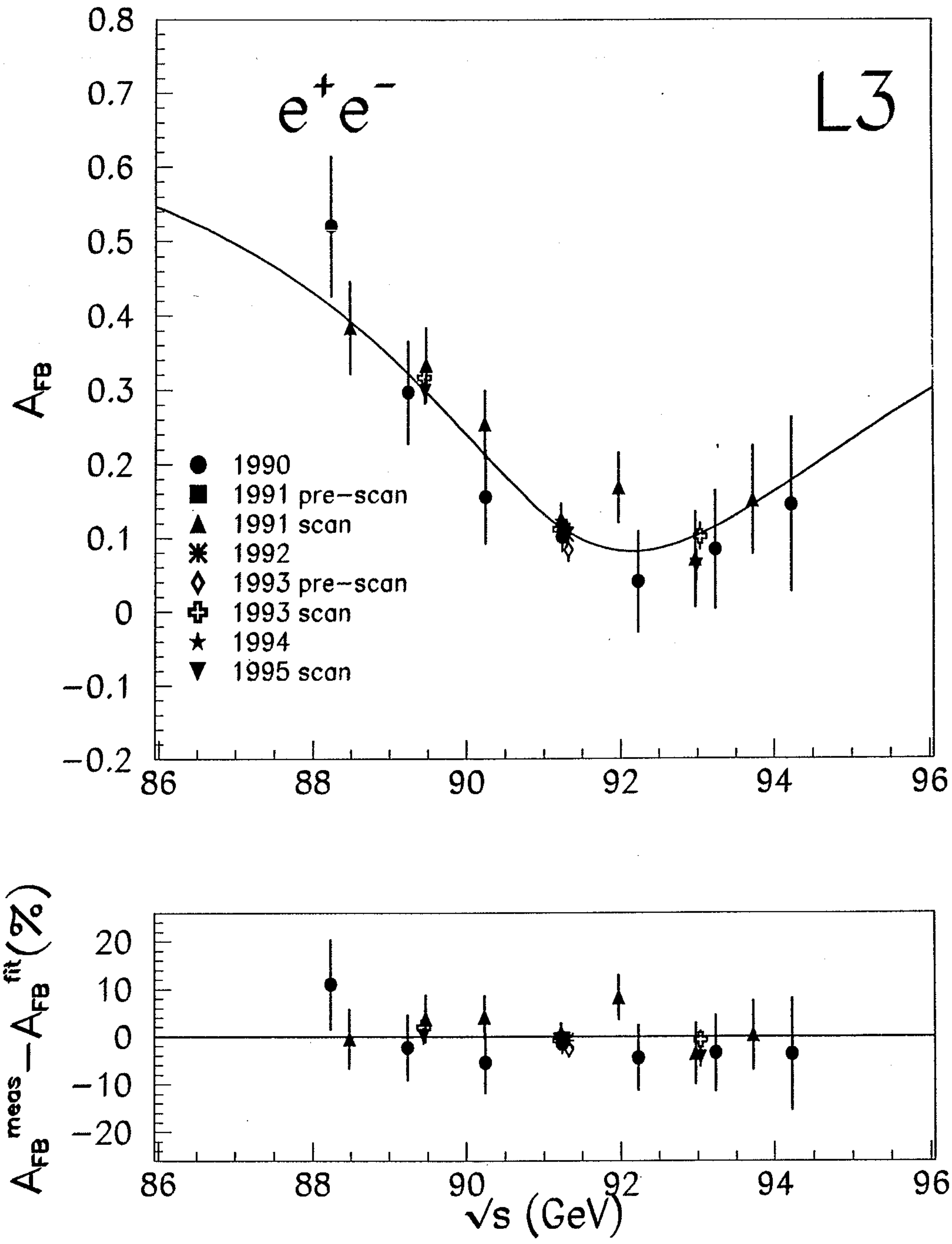

Figure 7.7: The measured forward backward asymmetries of the process $e^+e^- \rightarrow e^+e^-$ as function of centre of mass energy are shown in the figure, where the solid line shows the result of the fit. The bottom half of the figure shows the differences of the measured asymmetries and the fitted values is shown in (%) as a function of centre of mass energy.

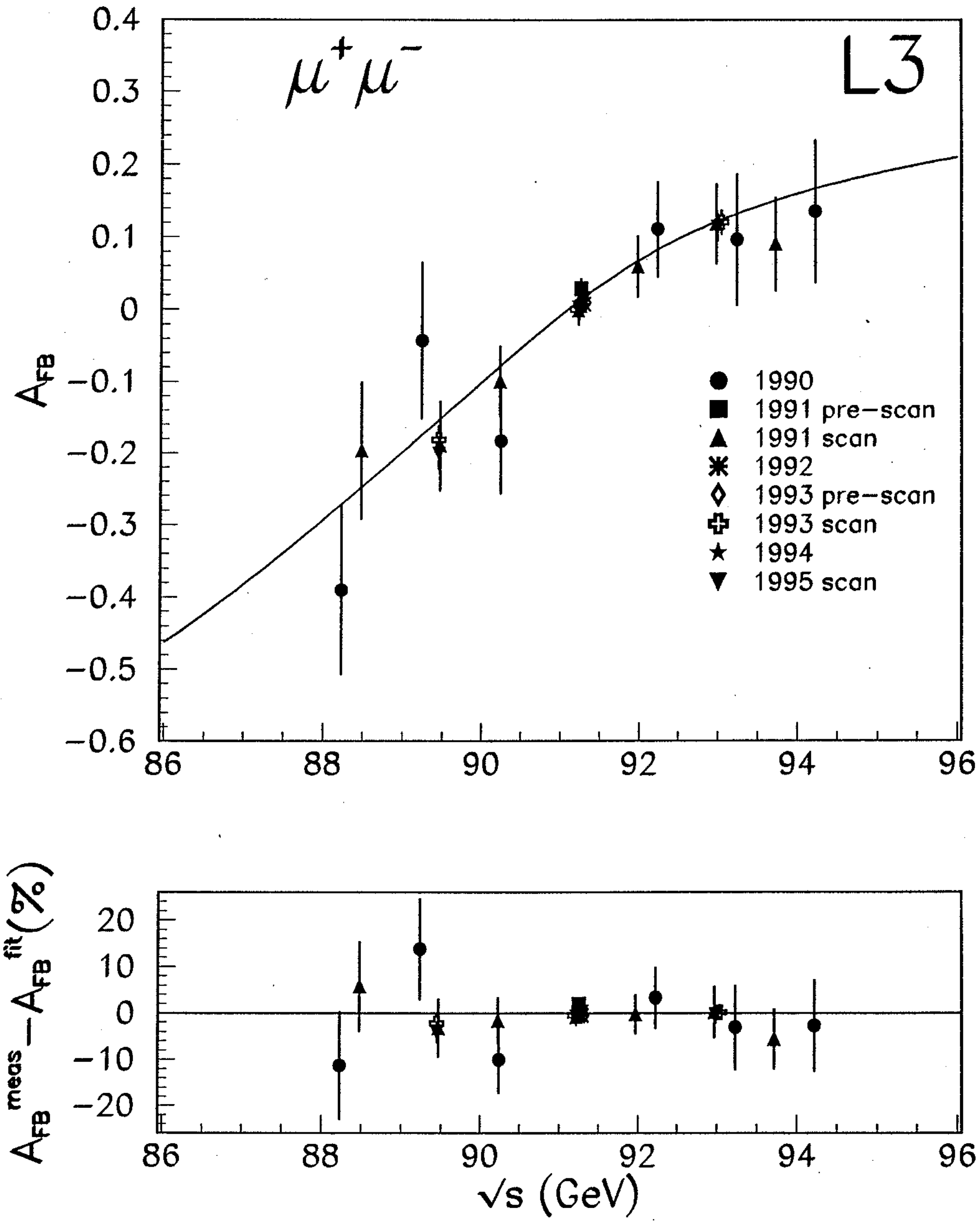

Figure 7.8: The measured forward backward asymmetries of the process $e^+e^- \rightarrow \mu^+\mu^-$ as function of centre of mass energy are shown in the figure, where the solid line shows the result of the fit. The bottom half of the figure shows the differences of the measured asymmetries and the fitted values is shown in (%) as a function of centre of mass energy.

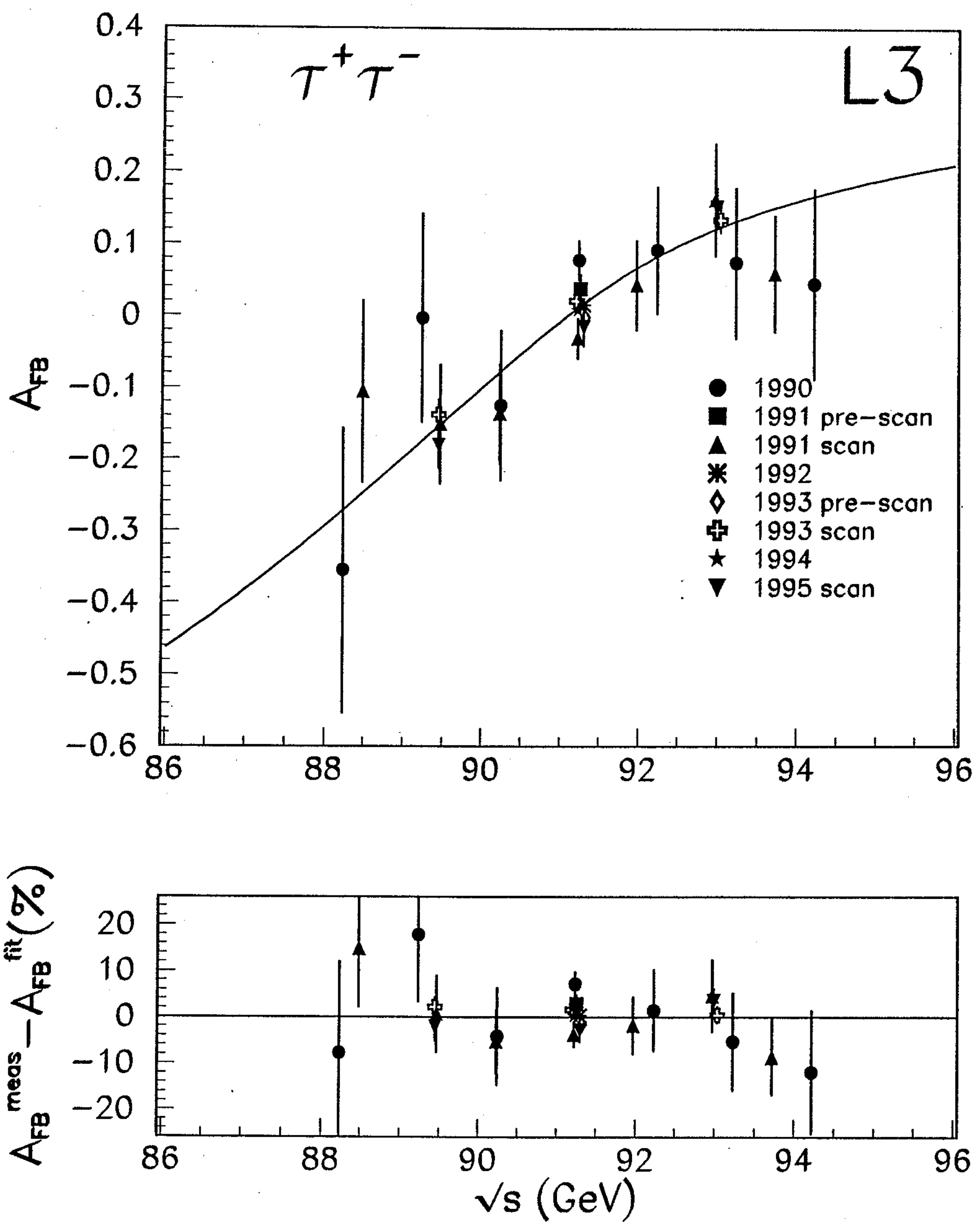

Figure 7.9: The measured forward backward asymmetries of the process $e^+e^- \rightarrow \tau^+\tau^-$ as function of centre of mass energy are shown in the figure, where the solid line shows the result of the fit. The bottom half of the figure shows the differences of the measured asymmetries and the fitted values is shown in (%) as a function of centre of mass energy.

correction for hadron remains (it is zero for leptons). δ_{QCD} is parametrised in terms of $\frac{\alpha_s}{\pi}$ as [17],

$$R_l = R_l^0\,[1 + 1.06\left(\frac{\alpha_s}{\pi}\right) + 0.90\left(\frac{\alpha_s}{\pi}\right)^2 - 15\left(\frac{\alpha_s}{\pi}\right)^3]. \tag{7.17}$$

Using the experimental value of $R_l = 20.788 \pm 0.066$ and the calculated value of $R_l^0 = 19.946$ from the Standard Model, the value of the strong coupling constant is determined to be,

$$\alpha_s = 0.124 \pm 0.010^{+0.005}_{-0.004} \tag{7.18}$$

where the first part of the error on α_s corresponds to the experimental uncertainty in R_l measurement. The second part of the error corresponds to the theoretical uncertainty on α_s.

7.4.5 Effective Vector and Axial Vector Couplings of Z^0 Boson

The effective vector and axial vector couplings of Z^0 boson to leptons is determined from the measurement of forward backward asymmetry of leptons together with the cross section measurements. The forward backward asymmetry can be defined in terms of the couplings in the following way,

$$\begin{aligned} A_{FB}^0 &= \frac{3}{4}A_e A_f \\ &= \frac{3}{4}\frac{2g_V^e g_A^e}{(g_V^e)^2 + (g_A^e)^2}\frac{2g_V^f g_A^f}{(g_V^f)^2 + (g_A^f)^2} \end{aligned} \tag{7.19}$$

The partial widths which are determined from cross section also depend on the couplings [equation (2.40)] as

$$\Gamma_f \propto (g_V^f)^2 + (g_A^f)^2 \tag{7.20}$$

A simultaneous fit to the cross section and forward backward asymmetry data enables us to determine the effective couplings of Z^0 to the leptons.

Measurement of tau polarisation A_{pol} and forward backward polarisation asymmetry A_{pol}^{fb} [87] are also used in addition to the lineshape data to determine the couplings,

$$A_{pol} = -A_\tau = -\frac{2g_V^\tau g_A^\tau}{(g_V^\tau)^2 + (g_A^\tau)^2} \tag{7.21}$$

$$A_{pol}^{fb} = -\frac{3}{4}A_e = -\frac{2g_V^e g_A^e}{(g_V^e)^2 + (g_A^e)^2}. \tag{7.22}$$

Inclusion of tau polarisation data significantly improves the errors on the couplings and determines the relative sign of these couplings. The individual signs of the couplings

Parameter	Treatment of Leptons		Standard
	non-universality	universality	Model
M_Z (MeV)	91 188.3±2.9	91 188.3±2.9	—
Γ_Z (MeV)	2 499.6±4.3	2 499.6±4.3	2 495.7
Γ_{had} (MeV)	1 745.2±5.4	1 745.5±4.2	1 742.8
g_A^e	−0.5011±0.0008	—	
g_A^μ	−0.5006±0.0015	—	
g_A^τ	−0.5015±0.0019	—	
g_A^l	—	−0.5010±0.0006	−0.5012
g_V^e	−0.0396±0.0034	—	
g_V^μ	$-0.0374^{+0.0085}_{-0.0079}$	—	
g_V^τ	−0.0394±0.0032	—	
g_V^l	—	$-0.0398^{+0.0027}_{-0.0029}$	−0.0361
χ^2/DOF	143/161	144/165	—

Table 7.8: Results for the effective vector and axial vector couplings of Z^0 to the charged leptons as obtained from fits to the total cross sections and forward backward asymmetries including measurements of tau polarisation asymmetries. In the last column the Standard Model predictions of these parameters are listed. They are calculated using $M_t = 175$ GeV, $M_H = 300$ GeV and $\alpha_s = 0.123$.

which can not be determined from this fit are assumed to be negative as per expection from the Standard Model. Nine parameter fits to the data are performed and the results are listed in table 7.8. The χ^2 per degrees of freedom is 143/161.

It is seen from the table that the couplings of Z^0 to e, μ and τ are same within errors. To determine the couplings with better precision we assume lepton universality and the results of 5-parameter fit are shown in third column of table 7.8. The expected values of vector and axial vector couplings in the Standard Model are listed in the last column of the table and they are seen to be in good agreement with the measurements.

In fig 7.10 the contour plot of the couplings g_V^f and g_A^f is shown at 68% confidence level. The dotted lines represent the couplings of individual leptons and the solid line shows the couplings assuming lepton universality.

7.4.6 Effective Electroweak Mixing Angle

The effective electroweak mixing angle from the leptonic final states can be defined in terms of the vector and axial vector couplings as

$$\sin^2\overline{\theta}_W^{\,l} = \frac{1}{4}\left(1 - \frac{g_V^l}{g_A^l}\right) \tag{7.23}$$

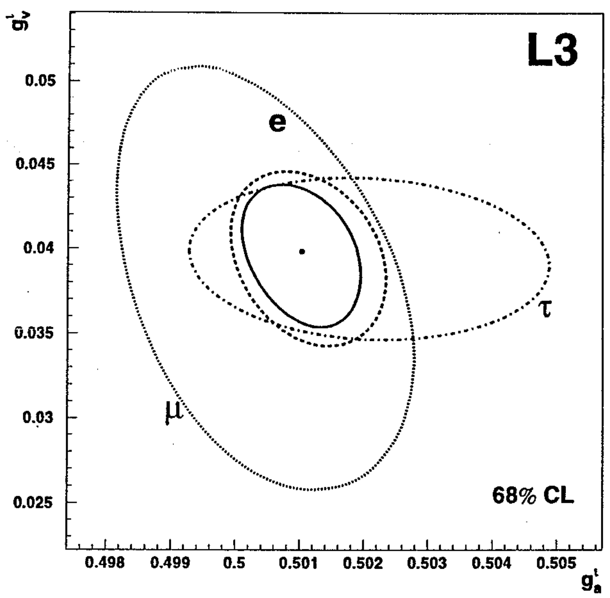

Figure 7.10: Contour plot g_V and g_A for leptons. The solid line shows the couplings assuming lepton universality. The dotted lines represent the couplings of individual leptons assuming lepton non universality.

It can be determined in several ways: from the forward backward asymmetry, the tau polarisation and tau polarisation asymmetries,

$$A^0_{FB} = 3\,\frac{(1-4\sin^2\overline{\theta}_w{}^l)^2}{[1+(1-4\sin^2\overline{\theta}_w{}^l)^2]^2} \tag{7.24}$$

$$A_{pol} = -2\,\frac{(1-4\sin^2\overline{\theta}_w{}^l)}{1+(1-4\sin^2\overline{\theta}_w{}^l)^2} \tag{7.25}$$

$$A^{fb}_{pol} = -\frac{3}{4}\,\frac{(1-4\sin^2\overline{\theta}_w{}^l)}{[1+(1-4\sin^2\overline{\theta}_w{}^l)^2]} \tag{7.26}$$

The electroweak mixing angle has also been determined using the measurement of forward backward asymmetry of the b-quark in $Z^0 \longrightarrow b\overline{b}$ [74].

From the measured values of A_{pol}, A^{fb}_{pol} [87], $A^{0,b}_{FB}$ [98] and the measurement of A_{FB} as mentioned in Section 7.4, we calculate the electroweak mixing angle and the values are given in table 7.9.

The combined value of $\sin^2\overline{\theta}_w{}^l$ from these measurements is,

$$\sin^2\overline{\theta}_w{}^l = 0.2304 \pm 0.0009 \tag{7.27}$$

Input data	$\sin^2\overline{\theta}_w^{\,l}$
$A_{FB}^{0,l}$	0.2301 ± 0.0014
$A_{pol} + A_{pol}^{fb}$	0.2307 ± 0.0013
$A_{FB}^{0,b}$	0.2304 ± 0.0020

Table 7.9: Determination of the effective weak mixing angle $\sin^2\overline{\theta}_w^{\,l}$ from different sources.

7.5 Results Within the Framework of Standard Model

The precise electroweak measurements presented in the previous section 7.4 can be used to check the validity of the Standard Model. One can also infer valuable informations, within the framework of Standard Model, about the effects of the top-quark mass (M_t) and the Higgs mass (M_H) through loop corrections on the electroweak measurements at LEP. The dependence on top-quark mass is quadratic and hence it is possible to estimate the value of M_t from fits to the electroweak measurements. On the other hand the dependence on M_H is logarithmic and therefore within the present accuracy of the data the constraints on M_H are still weak.

A simultaneous fit is performed to all the measurements within the framework of the Standard Model with M_Z, M_t, M_H and α_s as free parameters. The measurements used as input for this fit are listed in table 7.10.

Parameters	Values
M_Z (MeV)	$91\,188.3\pm2.9$
Γ_Z (MeV)	$2\,499.6\pm4.3$
σ^0_{had} (nb)	41.411 ± 0.074
R_l	20.788 ± 0.066
$A_{FB}^{0,l}$	0.0187 ± 0.0026
A_{pol} [87]	0.152 ± 0.013
A_{pol}^{fb}	0.156 ± 0.017
$A_{FB}^{0,b}$ [98]	0.107 ± 0.011
$R_b=(\Gamma_b/\Gamma_{had})$ [106]	0.2185 ± 0.0043

Table 7.10: Measured values of the parameters used as input for the fit in the Standard Model framework.

We need to use the electromagnetic fine structure constant α at $\sqrt{s} = M_Z$. There have been several re-evaluations of this constant [75] – [78]. For this analysis the value of $\alpha(M_Z)$ is taken from [78]:

$$1/\alpha\,(M_Z) = 128.896 \pm 0.090 \qquad (7.28)$$

As the sensitivity of the Higgs mass to the data is weak, we fix the value of M_H to 300 GeV for the fit. The effect of Higgs mass is studied by varying M_H in thc range 60−1000 GeV which is quoted as an extra error in the fitted parameters.

The value of top mass M_t and the strong coupling constant α_s estimated from the fit are given by,

$$M_t = 189^{+14}_{-15} \pm 16 \ (M_H) \ \text{GeV} \tag{7.29}$$

$$\alpha_s = 0.126 \pm 0.007 \pm 0.002 \ (M_H) \tag{7.30}$$

The second errors indicates the shift of the central values when Higgs mass is varied between 60 to 1000 GeV.

The value estimated for the strong coupling constant (α_s) is in good agreement with the measurement from hadronic event topologies and tau decays which is $\alpha_s = 0.123 \pm 0.006$ [60]. Constraining α_s to this independent measurement the fit result for the top quark mass improves to:

$$M_t = 191^{+13}_{-14} \pm 17\text{GeV} \tag{7.31}$$

The above estimate of top quark mass from the L3 data is in agreement with the recent direct measurement from CDF and DØ experiments at Tevatron which is 175 ± 6 GeV [120–122].

Chapter 8

Combination of Electroweak Results from Four LEP Experiments

8.1 Introduction

Electroweak parameters obtained by individual experiments ALEPH, DELPHI, L3 and OPAL at LEP are in good agreement among themselves. A global set of electroweak parameters can be obtained by averaging the four sets of results from four LEP experiments. The average set of parameters thus obtained is statistically much more precise. Results obtained from cross section and forward backward asymmetry in a model independent way are combined considering the proper correlation between the experiments. The results from the tau polarisation measurement and the heavy flavour results – $b\bar{b}$ and $c\bar{c}$ partial widths, and forward backward asymmetry – are also combined. Finally all these results are used to get the best constraint on the top quark mass and Higgs mass within the framework of the Standard Model. (Contribution of the author, who is also a member of the LEP Electroweak Working Group, in this chapter is in the combination of results from four LEP experiments [129])

8.2 Data from Four LEP Experiments

The four LEP experiments – ALEPH, DELPHI, L3 and OPAL – provided fit results to cross section and asymmetry measurements using data collected during 1990–1995. Two sets of fitted parameters are given out: (a) *9–parameter set* without any assumption of lepton universality and (b) *5–parameter* set with the assumption of lepton universality. (The procedure to determine these parameter sets are described in Chapter 7 for L3.) The details of the parameters are as follows,

- The Mass (M_Z) and total width (Γ_Z) of Z^0.

- The hadronic pole cross section :

$$\sigma^0_{had} = \frac{12\pi}{M_Z{}^2}\frac{\Gamma_e\Gamma_{had}}{\Gamma_Z{}^2} \tag{8.1}$$

here Γ_e and Γ_{had} are the partial widths of Z^0 decays into electron and hadrons respectively.

- The ratios of the hadronic partial width to the partial widths of individual leptons (Γ_e, Γ_μ, Γ_τ):

$$R_e = \frac{\Gamma_{had}}{\Gamma_e} \qquad R_\mu = \frac{\Gamma_{had}}{\Gamma_\mu} \qquad R_\tau = \frac{\Gamma_{had}}{\Gamma_\tau} \tag{8.2}$$

- The pole forward backward asymmetries of the leptonic final states which is defined in terms of the effective vector and axial vector couplings in the following way,

$$A^{0,e}_{FB} = \frac{3}{4}A_eA_e \qquad A^{0,\mu}_{FB} = \frac{3}{4}A_eA_\mu \qquad A^{0,\tau}_{FB} = \frac{3}{4}A_eA_\tau \tag{8.3}$$

where,

$$A_f = \frac{2\,g^f_V g^f_A}{g^f_V{}^2 + g^f_A{}^2} \tag{8.4}$$

This 9 parameter set reduces to a 5 parameter set (M_Z, Γ_Z, σ^0_{had}, R_l and $A^{0,l}_{FB}$), if lepton universality is assumed. R_l is defined as $R_l = \frac{\Gamma_{had}}{\Gamma_{lept}}$ where Γ_{lept} refers to the partial width of Z^0 to a pair of massless leptons. Similarly $A^{0,l}_{FB}$ is defined in terms of g^l_V and g^l_A.

The analysis details of individual experiments can be found in references [80, 82] for ALEPH, DELPHI, OPAL and [59–61, 83] for L3. Table 8.2 lists the 5 parameter results and 8.1 lists 9 parameter results obtained from individual experiments alongwith the χ^2 in each case.

Each experiment also provides 9×9 and 5×5 correlation matrices for these 9 and 5 parameter sets.

These parameter sets from individual experiments are correlated in the following way.

- The uncertainty in the LEP energy calibration correlates individual measurement. It causes errors of $\Delta M_Z \approx 1.5$ MeV and $\Delta\Gamma_Z \approx 1.7$ MeV and $\Delta A^{0,l}_{FB} \approx 0.0005$ for all lepton species. The uncertainty in the beam energy spread of about 1 MeV introduces an error of 0.1 MeV on total width.

- $A^{0,e}_{FB}$ is anti-correlated to $A^{0,\mu}_{FB}$ and $A^{0,\tau}_{FB}$. $A^{0,\mu}_{FB}$ and $A^{0,\tau}_{FB}$ are correlated fully.

- All the four experiments measure integrated luminosity using small angle Bhabha events and use the same generator [48] for theoretical cross section. The theoretical uncertainty in the cross section thus introduces correlation between the experiments.

	ALEPH	DELPHI	L3	OPAL
M_Z(GeV)	91.1873±0.0030	91.1859±0.0028	91.1883±0.0029	91.1824±0.0039
Γ_Z (GeV)	2.4950±0.0047	2.4896±0.0042	2.4996±0.0043	2.4956±0.0053
$\sigma^0_{\rm had}$ (nb)	41.576±0.083	41.566±0.079	41.411±0.074	41.53±0.09
R_e	20.64±0.09	20.93±0.14	20.78±0.11	20.82±0.14
R_μ	20.88±0.07	20.70±0.09	20.84±0.10	20.79±0.07
Rt	20.78±0.08	20.78±0.15	20.75±0.14	20.99±0.12
$A^{0,e}_{\rm FB}$	0.0187±0.0039	0.0179±0.0051	0.0148±0.0063	0.0104±0.0052
$A^{0,\mu}_{\rm FB}$	0.0179±0.0025	0.0153±0.0026	0.0176±0.0035	0.0146±0.0025
$A^{0,\tau}_{\rm FB}$	0.0196±0.0028	0.0223±0.0039	0.0233±0.0049	0.0178±0.0034
χ^2/DOF	195/217	174/157	142/159	12/6$^{(a)}$

Table 8.1: Values of 9-parameter sets from four LEP experiments. This is obtained from a simultaneous fit to cross section and asymmetry data assuming lepton non universality. The χ^2 for all four sets are also listed. $^{(a)}$This parameter set has been obtained from a parameter transformation applied to the 15 parameters of the OPAL fit [82].

	ALEPH	DELPHI	L3	OPAL
M_Z (GeV)	91.1874±0.0030	91.1859±0.0028	91.1883±0.0029	91.1822±0.0039
Γ_Z (GeV)	2.4948±0.0047	2.4896±0.0042	2.4996±0.0043	2.4955±0.0053
$\sigma^0_{\rm had}$ (nb)	41.578±0.083	41.566±0.079	41.411±0.074	41.53±0.09
R_l	20.766±0.049	20.754±0.068	20.788±0.066	20.83±0.06
$A^{0,l}_{\rm FB}$	0.0187±0.0017	0.0175±0.0020	0.0187±0.0026	0.0150±0.0019
χ^2/DOF	200/221	178/161	144/163	15/10$^{(a)}$

Table 8.2: Values of 5-parameter sets from four LEP experiments. This is obtained from a simultaneous fit to cross section and asymmetry data assuming lepton universality. The χ^2 for all four sets are also listed. $^{(a)}$This parameter set has been obtained from a parameter transformation applied to the 15 parameters of the OPAL fit [82].

8.3 Combined Results from LEP

In this section we present the combined results from the four LEP experiments based on two sets of parameters presented in section 8.2. Average sets of parameters are obtained by minimising the χ^2, which is defined as,

$$\chi^2 = \Delta^T V^{-1} \Delta \tag{8.5}$$

Here Δ is the vector containing the residuals of the combined parameter set to the results of the individual experiments. V is the full covariance matrix constructed [79] from the covariance matrices of individual experiments, considering the common errors from LEP energy calibration and the luminosity, and taking into account appropriately correlations between the experiments.

The combined results of 9 and 5 parameter sets are given in tables 8.3 and 8.4.

Parameter	Average Value
M_Z (GeV)	91.1863±0.0020
Γ_Z (GeV)	2.4946±0.0027
σ^0_{had} (nb)	41.508±0.056
R_e	20.754±0.057
R_μ	20.796±0.040
R_τ	20.814±0.055
$A^{0,e}_{FB}$	0.0160±0.0024
$A^{0,\mu}_{FB}$	0.0162±0.0013
$A^{0,\tau}_{FB}$	0.0201±0.0018
χ^2/DOF	22/27

Table 8.3: Average line shape and asymmetry parameters from the data of the four LEP experiments given in table 8.1, without the assumption of lepton universality.

Parameter	Average Value
M_Z (GeV)	91.1863±0.0020
Γ_Z (GeV)	2.4946±0.0027
σ^0_{had} (nb)	41.508±0.056
R_l	20.778±0.029
$A^{0,l}_{FB}$	0.0174±0.0010

Table 8.4: Average line shape and asymmetry parameters from the results of the four LEP experiments given in Table 8.2, assuming lepton universality. The value of χ^2 per degrees of freedom is 1.2.

8.3.1 Mass of Z^0 Boson

The mass of Z^0 obtained by the four experiments are in good agreement. Figure 8.1 shows the comparison of Z^0 boson mass obtained by individual measurements together with the value obtained after combination. The value of M_Z obtained after combining the values from the four experiments is given by,

$$M_Z = 91186.3 \pm 1.3 \pm 1.5 \text{ MeV} \tag{8.6}$$

where the first part in the error represents the error coming from experimental uncertainties and the second part is due to the uncertainty in the LEP energy calibration.

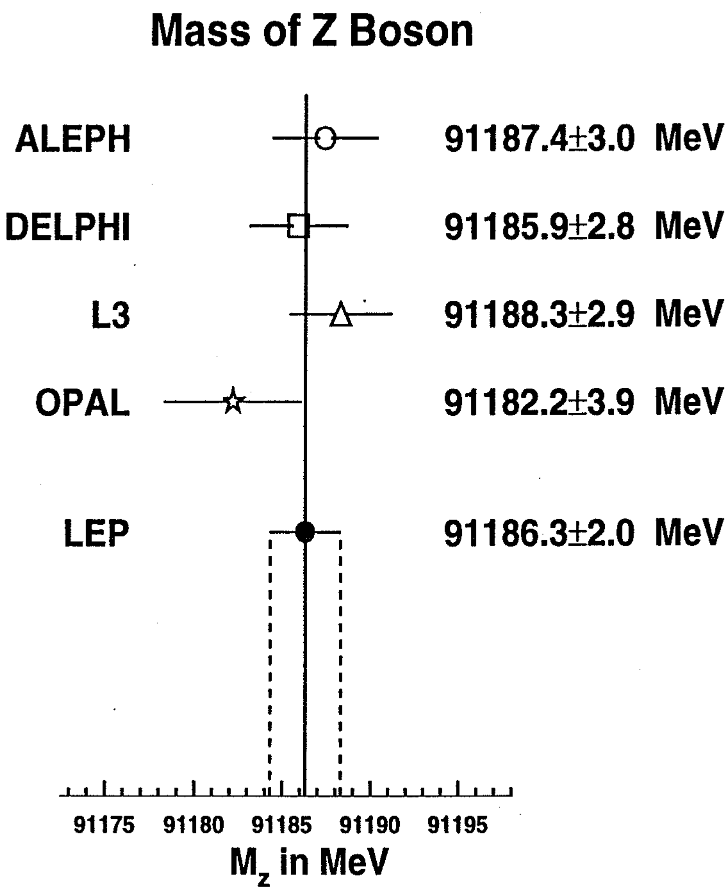

Figure 8.1: Comparison of the values of M_Z obtained by the four LEP experiments. The average of the four measurements is shown with error bar at the bottom.

8.3.2 Total Width of Z^0 Boson

Total width of the Z^0 boson depend on the top quark and the Higgs masses in the Standard Model. A precise measurement of the total width thus constrains these parameters. The value of the width obtained from combination of the results from the four LEP experiments is given by

$$\Gamma_Z = 2494.6 \pm 2.1 \pm 1.7 \text{ MeV} \tag{8.7}$$

where the first error is the experimental uncertainty and the second error represents the contribution coming from LEP energy calibration. The values of the total width together with the combined results are given in fig 8.2.

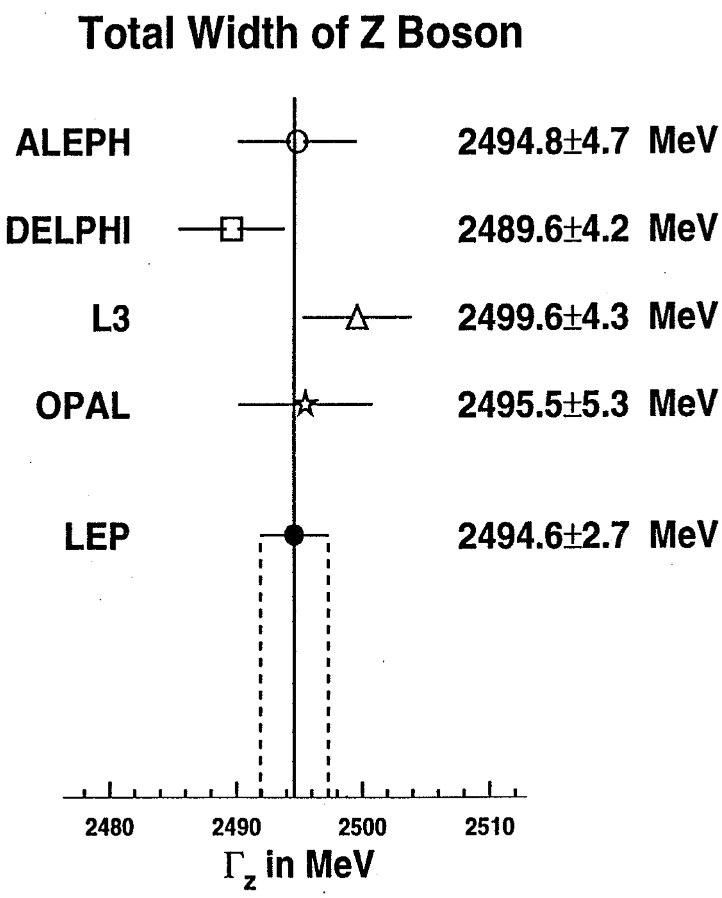

Figure 8.2: Comparison of the values of the total width of Z^0 obtained by different experiments. The average of the four measurements is shown with error at the bottom.

8.3.3 Partial Widths of Z^0 Boson

The partial decay widths of Z^0 to hadronic and leptonic channels are derived from 9 parameter fit result. The results are listed in table 8.5, where the leptonic width Γ_{lept} (assuming lepton universality i.e. $\Gamma_e = \Gamma_\mu = \Gamma_\tau \equiv \Gamma_{lept}$) is also listed. The invisible width due to Z^0 decays into neutrino pairs is obtained from the measured values of the total and partial widths of Z^0.

Parameter	Treatment of Leptons	
(MeV)	Non-universality	Universality
Γ_{had}	—	1 743.6±2.5
Γ_e	83.96±0.15	—
Γ_μ	83.79±0.22	—
Γ_τ	83.72±0.26	—
Γ_{lept}	—	83.91±0.11
Γ_{inv}		499.5±2.0

Table 8.5: Average values of the partial widths of Z^0

8.3.4 Number of Neutrino Species

A precise estimate of the number of light neutrino species is obtained from a combination of results from the four LEP experiments. The invisible width is measured with a precision of 2 MeV. The ratio of invisible width to the leptonic width is obtained as,

$$\Gamma_{inv}/\Gamma_{lept} = 5.952 \pm 0.023 \tag{8.8}$$

and the Standard Model value for the ratio of the neutrino width to the leptonic width is

$$(\Gamma_\nu/\Gamma_{lept})_{SM} = 1.991 \pm 0.001 \tag{8.9}$$

The central value is evaluated for $M_Z = 91.1836$ GeV, $M_t = 175$ GeV, $M_H = 300$ GeV and the error quoted here accounts for the variation of M_t in the range 169-181 GeV and M_H in the range 60-1000 GeV. The number of light neutrino species is obtained as,

$$\begin{aligned} N_\nu &= \left(\frac{\Gamma_{inv}}{\Gamma_{lept}}\right) \cdot \left(\frac{\Gamma_{lept}}{\Gamma_\nu}\right)_{SM} \\ &= 2.989 \pm 0.012 \end{aligned} \tag{8.10}$$

8.3.5 Effective Couplings

The effective vector and axial vector couplings of Z^0 to the leptons can be determined in several ways: (i) forward backward asymmetry of the charged leptons which is a function of g_V^l/g_A^l, (ii) tau polarisation A_{pol}, which is a function of g_V^τ/g_A^τ and (iii) tau polarisation asymmetry A_{pol}^{fb}, which is a function of g_V^e/g_A^e.

The tau polarisation and polarisation asymmetry results from individual experiments and the global LEP average are listed in table 8.6. Nine parameter fit results listed in

	A_τ	A_e
ALEPH [84]	$0.136 \pm 0.012 \pm 0.009$	$0.129 \pm 0.016 \pm 0.005$
DELPHI [85]	$0.138 \pm 0.009 \pm 0.008$	$0.140 \pm 0.013 \pm 0.003$
L3 [86, 87]	$0.152 \pm 0.010 \pm 0.009$	$0.156 \pm 0.016 \pm 0.005$
OPAL [88]	$0.134 \pm 0.009 \pm 0.010$	$0.129 \pm 0.014 \pm 0.005$
LEP Average	0.1401 ± 0.0067	0.1382 ± 0.0076

Table 8.6: Results of A_τ and A_e from tau polarisation measurements from four LEP experiments and the average value. The first error for experimental measurements corresponds to the statistical error and the second error corresponds to the systematic error.

table 8.3 together with the average value of tau polarisation and polarisation asymmetry listed in table 8.6 are used to derive effective vector and axial vector couplings of Z^0 to leptons. The values of couplings thus obtained with and without the assumption of lepton universality are listed in table 8.7. The values of the couplings g_V^l and g_A^l assuming lepton universality are in good agreement with the expected values from the Standard Model.

Parameter	Treatment of Leptons		Standard Model
	non-universality	universality	
g_A^e	−0.50130±0.00046	—	
g_A^μ	−0.50076±0.00069	—	
g_A^τ	−0.50116±0.00079	—	
g_A^l	—	−0.50115±0.00034	−0.5012
g_V^e	−0.0368±0.0015	—	
g_V^μ	−0.0372±0.0034	—	
g_V^τ	−0.0369±0.0016	—	
g_V^l	—	−0.03688±0.00085	−0.0361

Table 8.7: Results for the effective axial-vector and vector couplings derived from the combined LEP data with and without the assumption of lepton universality.

8.3.6 Effective Electroweak Mixing Angle

The effective electroweak mixing angle is defined as,

$$\sin^2\overline{\theta}_w^{\,l} = \frac{1}{4}\left(1 - g_V^l/g_A^l\right) \tag{8.11}$$

and can be determined from various asymmetry measurements mentioned in section 7.4.6. The mixing angle is also determined from forward-backward asymmetry of b and c quarks $A_{FB}^{0,b}$ and $A_{FB}^{0,c}$ [92–100], and measurement of quark charge asymmetry [89–91]. We have summarised the results from all sources in table 8.8. The average of all the measurements is,

$$\sin^2\overline{\theta}_w^{\,l} = 0.2320 \pm 0.0003 \tag{8.12}$$

	$\sin^2\overline{\theta}_w^{\,l}$
$A_{FB}^{0,l}$	0.23085±0.00056
A_τ	0.23240±0.00085
A_e	0.23264±0.00096
$A_{FB}^{0,b}$	0.23246±0.00041
$A_{FB}^{0,c}$	0.23155±0.00112
$\langle Q_{FB}\rangle$	0.2320±0.0010

Table 8.8: Values of effective electroweak mixing angle $\sin^2\overline{\theta}_w^{\,l}$ from different sources

8.4 Constraints on the Top quark and Higgs Mass

In the previous section 8.2 we have summarised results from the four LEP experiments and the combined results from these experiments are presented in section 8.3. The accuracy of these measurements have become sensitive to test the Standard Model.

Before the start-up of LEP in 1989, there were four unknown parameters in the Standard Model: the mass of Z^0 (M_Z was measured at the $p\overline{p}$ collider at CERN and Tevatron but with a large error), mass of the top quark (M_t), mass of Higgs boson (M_H) and the strong coupling constant (α_s) at M_Z.

At LEP one has determined the mass of Z^0 with a very high precision of $\Delta M_Z/M_Z = 2.2 \times 10^{-5}$ and strong coupling constant has been measured from lineshape measurement (see section 7.4.4) and from various event shape variables [127, 128].

The mass of the top-quark and the Higgs boson is estimated from a fit to the measurements performed at LEP, inside the framework of the Standard Model. The measurements which are used as input to this fit are: combined 5-parameter results, tau polarisation and heavy flavour results which include results from b and c quark asymmetry and partial widths in terms of $R_b(=\Gamma_b/\Gamma_{had})$ [101–108] and $R_c(=\Gamma_c/\Gamma_{had})$ [109–111]. All these values are listed in the second column of table 8.9, under sub-heading LEP.

The measured quantities depend quadratically on the top-quark mass and logarithmically on Higgs mass. Hence the effect of M_H is weaker. We perform the fit in two ways.

	Measurement with Total Error	Standard Model	Pull
a) LEP			
lineshape and lepton asymmetries:			
M_Z [GeV]	91.1863$\pm$ 0.0020	91.1861	0.1
g_A^μ [GeV]	2.4946 $\pm$ 0.0027	2.4960	-0.5
σ^0_{had} [nb]	41.508 $\pm$ 0.056	41.465	0.8
R_l	20.778 $\pm$ 0.029	20.757	0.7
$A_{FB}^{0,l}$	0.0174 $\pm$ 0.0010	0.0159	1.4
+ correlation matrix			
τ polarisation:			
A_τ	0.1401 $\pm$ 0.0067	0.1458	-0.9
A_e	0.1382 $\pm$ 0.0076	0.1458	-1.0
b and c quark results:			
R_b	0.2179 $\pm$ 0.0012	0.2158	1.8
R_c	0.1715 $\pm$ 0.0056	0.1723	-0.1
$A_{FB}^{0,b}$	0.0979 $\pm$ 0.0023	0.1022	-1.8
$A_{FB}^{0,c}$	0.0733 $\pm$ 0.0049	0.0730	0.1
+ correlation matrix			
$q\overline{q}$ charge asymmetry:			
$\sin^2\overline{\theta}_w^l$ $\langle Q_{FB}\rangle$)	0.2320 $\pm$ 0.0010	0.23167	0.3
b) SLD			
$\sin^2\overline{\theta}_w^l$ (ALR [112, 113])	0.23061 $\pm$ 0.00047	0.23167	-2.2
R_b [114]	0.2149 $\pm$ 0.0038	0.2158	-0.2
A_b [115]	0.863 $\pm$ 0.049	0.935	-1.4
A_c [115]	0.625 $\pm$ 0.084	0.667	-0.5
c) $p\overline{p}$ and νN			
M_W [GeV] ($p\overline{p}$ [116, 119])	80.356 $\pm$ 0.125	80.353	0.0
$1 - {M_W}^2/{M_Z}^2$ (νN [123–125])	0.2244 $\pm$ 0.0042	0.2235	0.2
M_t [GeV] ($p\overline{p}$ [120–122])	175 $\pm$ 6	172	0.5

Table 8.9: Summary of measurements included in the combined analysis of Standard Model parameters. The measured values of the parameters are given in column 2. The Standard Model values of these parameters obtained from the fit to all data in the Standard Model framework are listed in column 3 and the difference between the measurement and the fit in terms of measurement errors, pulls are given in column 4.

In the first case we fix M_H to 300 GeV and do the fit with M_t and α_s as free parameters. The results are given in the second column of table 8.10. The effect of the Higgs mass on the fitted quantities are calculated by varying M_H in the range 60–100 GeV and is quoted as second error. In the other case all three parameters M_t, M_H and α_s are treated as free parameters. The result of the fit is listed in the last column of table 8.10. It is seen that the value of M_t agrees within one standard deviation in two methods.

	LEP Data Only	
M_t (GeV)	$171 \pm 8^{+17}_{-19}$	155^{+18}_{-13}
M_H (GeV)	300 (Fixed)	86^{+202}_{-51}
α_s	$0.122 \pm 0.003 \pm 0.002$	0.121 ± 0.003
χ^2/DOF	10/9	9/8

Table 8.10: Results of the fits to LEP data alone inside the framework of the Standard Model. As the sensitivity to the Higgs mass is weak fits are performed with fixed M_H. Results of free M_H fit is given in the last column.

The two experiments CDF and DØ at Tevatron have confirmed the existence of the top quark and the mass of top quark from these two experiments is 175 ± 6 GeV [120–122].

In order to have a better constraint on the Higgs mass we include in the fit the measured value of the top quark mass. We also include all available electroweak results from different experiments which are : measurements of $A_b(=\frac{2g_V^b g_A^b}{{g_V^b}^2+{g_A^b}^2})$, $A_c(=\frac{2g_V^c g_A^c}{{g_V^c}^2+{g_A^c}^2})$, R_b and $\sin^2\overline{\theta}_W^{\,l}$ from SLD experiment at SLAC [112–115], measurement of $(1 - {M_W}^2/{M_Z}^2)$ from νN scattering experiments [123–125], and the W mass measurements from $p\overline{p}$ colliders [116, 119]. All these values are also listed in table 8.9. We have carried out the fit with M_t, M_H and α_s as the free parameters.

The Standard Model values corresponding to the fitted data are listed in the third column of table 8.9. The last column of the table gives the quality of the fit in terms of *Pull*, which is defined as:

$$\text{Pull} \quad = \quad \frac{Q_{meas} - Q_{fit}}{\Delta Q_{meas}} \qquad (8.13)$$

where Q_{meas} is the measured quantity, Q_{fit} is the fitted value and ΔQ_{meas} is the error on the measured quantity. As an example, the value of Pull of 1.0 means that the fitted value is deviating from the measured value by one standard deviation. Out of 19 values fitted only 6 values ($A_{FB}^{0,l}$, A_e, R_b, $A_{FB}^{0,b}$, and $\sin^2\overline{\theta}_W^{\,l}$, A_b of SLD) have Pulls between 1.0 and 2.2. On the whole the Standard Model fit to the measured quantities is good.

In table 8.11 we have listed the fitted values of M_t, M_H and α_s using all available measurements. It is seen from table 8.10 and table 8.11 that the fit results to LEP data alone is in agreement within one standard deviation with the results obtained from all available measurements. The value of Higgs mass thus deduced is,

	LEP +SLD + $p\bar{p}$ and νN data + M_t
M_t (GeV)	172 ± 6
M_H (GeV)	149^{+148}_{-82}
α_s	0.120 ± 0.003
χ^2/DOF	19/14

Table 8.11: Results of the fits to all data including the top quark mass.

$$M_H = 149^{+148}_{-82}\mathrm{GeV} \tag{8.14}$$

68% confidence level contour plot of M_t and M_H is shown in figure 8.3 using only LEP measurement and all available measurements. The upper limit on Higgs mass at 95% Confidence Level is 550 GeV.

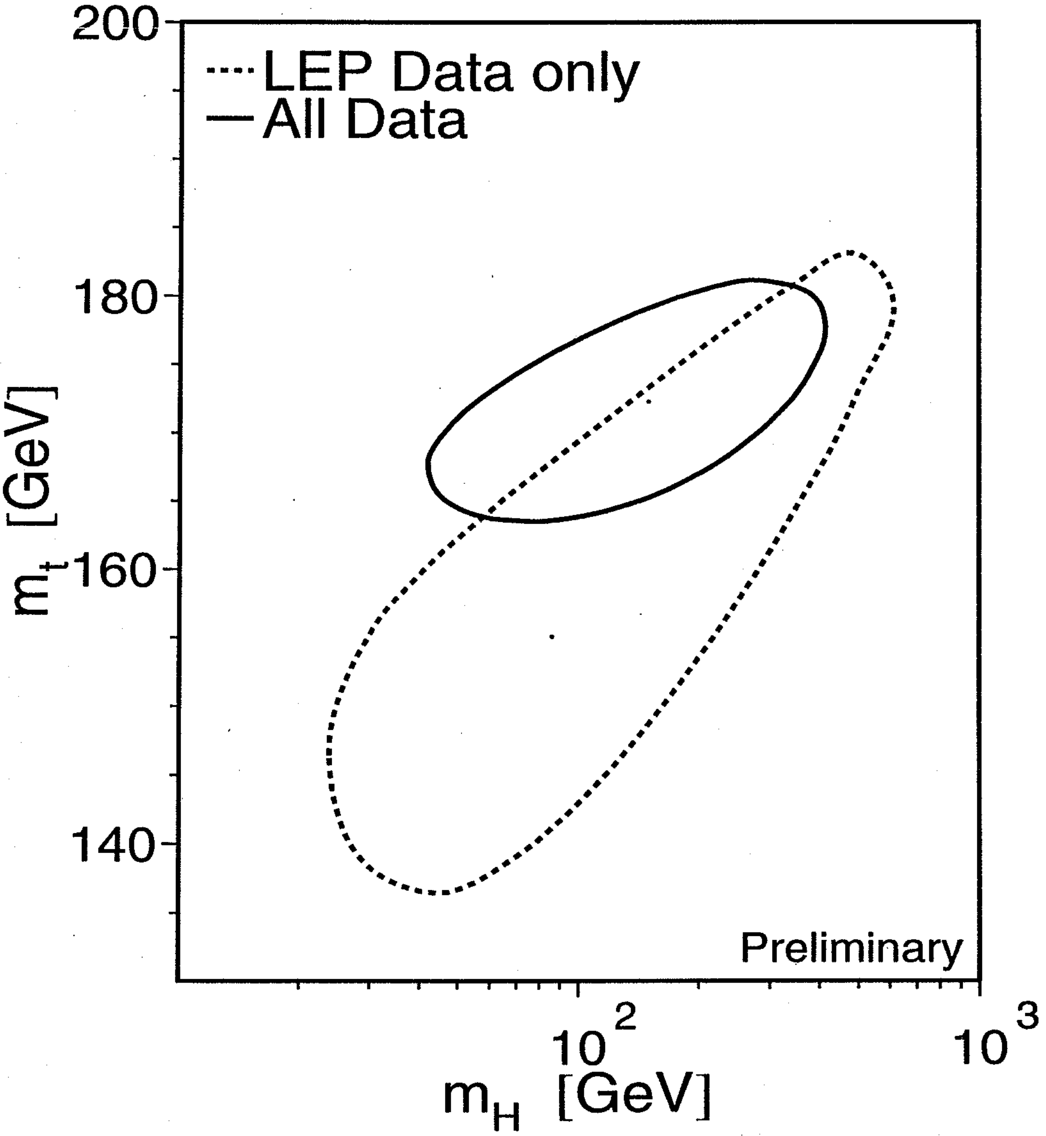

Figure 8.3: 68% confidence level contour plot of M_t vs M_H

Chapter 9

Summary

We have presented in this thesis the determination of the properties of the weak neutral vector boson Z^0 in detail which are produced in the e^+e^- interactions at LEP. The centre of mass energy of the LEP collider. was chosen at phase I for the resonance production of Z^0. Z^0 particles decay into hadrons, e^+e^-, $\mu^+\mu^-$ and $\tau^+\tau^-$ which are detected in the detector. The decays of Z^0 into a pair of neutrinos are not visible in the detector.

We have described in detail the measurement of the cross section and the forward backward asymmetry of the process $e^+e^- \rightarrow \tau^+\tau^-$. The data collected in the years 1992, 1994 and 1995 by the L3 detector are analysed. We have selected $\tau^+\tau^-$ events with background contamination of 2–3%. The measured values of the cross sections at different centre of mass energies together with statistical and systematic errors are listed in table 6.5. The dominant contribution to the systematic error comes from the selection criteria. The measured values of the cross sections are in good agreement with the Standard Model predictions. The forward backward asymmetry in $\tau^+\tau^-$ events is also measured and listed in table 6.6. The dominant contribution to the systematic error comes from the error in the charge confusion and background correction.

Measured values of cross sections and forward backward asymmetries are then fitted to the theoretical expectations in order to determine the properties of Z^0 boson. We have used the measurements in the L3 experiment from the year 1990 to 1995 based on 3.7×10^6 Z^0 events. The mass and total width of Z^0 is determined as,

$$\begin{aligned} M_Z &= 91188.1 \pm 2.9 \text{ MeV} \\ \Gamma_Z &= 2499.8 \pm 4.3 \text{ MeV} \end{aligned}$$

All four experiments at LEP measure Z^0 parameters following the same procedure. A global set of parameters are obtained averaging these four sets. The full statistics of 16.1×10^6 Z^0 events collected at LEP is used in this way.

The combined values of mass and the total width of Z^0 from the four LEP experiments are:

$$\begin{aligned} M_Z &= 91186.3 \pm 2.0 \text{ MeV} \\ \Gamma_Z &= 2494.6 \pm 2.7 \text{ MeV} \end{aligned}$$

The mass is measured with an accuracy of $\Delta M_Z/M_Z = 2.2 \times 10^{-5}$ which is very close to the accuracy obtained for the Fermi coupling constant $\Delta G_\mu/G_\mu = 1.7 \times 10^{-5}$. The total width of Z^0 is measured to a precision of $\Delta\Gamma_Z/\Gamma_Z = 1.1 \times 10^{-3}$.

The lepton universality which is one of the assumptions of the Standard Model is tested in two ways : from leptonic partial widths of Z^0 and from the effective couplings of Z^0 to leptons.

The measured values of the partial widths of Z^0 into different leptonic channels agree within errors as given by

$$\begin{aligned} \Gamma_e &= 83.96 \pm 0.15 \text{ MeV} \\ \Gamma_\mu &= 83.79 \pm 0.22 \text{ MeV} \\ \Gamma_\tau &= 83.72 \pm 0.26 \text{ MeV} \end{aligned}$$

The universal leptonic width is measured as,

$$\Gamma_{lept} = 83.91 \pm 0.11 \text{ MeV}$$

The effective couplings for individual leptonic modes agree within one standard deviation and the effective couplings obtained assuming lepton universality is given by,

$$\begin{aligned} g_A^l &= -0.50115 \pm 0.00034 \\ g_V^l &= -0.03688 \pm 0.00085 \end{aligned}$$

The value of the electroweak mixing angle is given by,

$$\sin^2\overline{\theta}_w^{\,l} = 0.2320 \pm 0.0003$$

The number of light neutrino families of mass $\leq M_Z/2$ is determined from the measured values of total and partial widths of Z^0 and is given by,

$$N_\nu = 2.989 \pm 0.012$$

LEP measurements are able to probe the weak radiative corrections which are at the level of 1%. As a consequence of that the value of the top quark mass (M_t), Higgs mass (M_H) and the strong coupling constant (α_s) are estimated.

Mass of the top quark is estimated in the framework of the Standard Model in two ways:

(i) By fixing the mass of Higgs at 300 GeV and keeping M_t and α_s as free parameters we get,

$$\begin{aligned} M_t &= 171 \pm 8^{+17}_{-19} \text{ GeV} \\ \alpha_s &= 0.122 \pm 0.003 \pm 0.002 \end{aligned}$$

The effect due to Higgs mass is given as the second error where M_H was varied in the range 60–1000 GeV.

(ii) We keep all three quantities M_t, M_H and α_s as free parameters and obtain the following results,

$$\begin{aligned} M_t &= 155^{+18}_{-13} \text{ GeV} \\ M_H &= 86^{+202}_{-51} \text{ GeV} \\ \alpha_s &= 0.121 \pm 0.003 \end{aligned}$$

The estimation of the top quark mass is in good agreement with the direct measurement of 175 $\pm$ 6 GeV at CDF and D$\emptyset$ experiments at Tevatron collider at Fermilab. This lends strong support to the electroweak radiative corrections of the Standard Model.

Using all available electroweak measurements and the measured value of M_t we estimate the Higgs mass to be,

$$M_H = 149^{+148}_{-82} \text{ GeV}$$

This yields an upper limit of 550 GeV at 95% confidence level.

The precise measurement of the electroweak parameters at LEP supports strongly the validity of the predictions of the Standard Model. The high precision obtained on the measured parameters indicates the success of the LEP experiment. The next generation of experiments will get the advantage of using these parameters measured at LEP as input.

The Z^0 physics era of LEP came to an end in October 1995. LEP is now running at higher centre of mass energy to produce $W^\pm$ pairs. Some of the major topics under study are: (a) precision measurement of mass and width of W boson, (b) determination of the triple gauge boson couplings of ZWW and γWW, and (c) search of new particles.

Appendix A

Calculation of Beam Spread Effect on Cross Section

The cross section as a function of the centre of mass energy (E) can be expressed as,

$$\sigma(\mathrm{E}) = \mathrm{a}_0 + \mathrm{a}_1\mathrm{E} + \mathrm{a}_2\mathrm{E}^2 \tag{A.1}$$

The beam energy spread is assumed to be Gaussian with standard deviation ω around the mean energy $\overline{E}$. The distribution function can be written as

$$\mathrm{F}(\mathrm{E}) = \frac{1}{\sqrt{2\pi}\omega}\, \mathrm{e}^{-\frac{(\mathrm{E}-\overline{\mathrm{E}})^2}{2\omega^2}} \tag{A.2}$$

The convoluted cross section is given by,

$$\begin{aligned} \sigma_{\text{convoluted}} &= \frac{1}{\sqrt{2\pi}\omega} \int_{-\infty}^{\infty} \mathrm{e}^{-\frac{(\mathrm{E}-\overline{\mathrm{E}})^2}{2\omega^2}}\, \sigma(\mathrm{E})\, \mathrm{dE} \\ &= \mathrm{a}_0 + \mathrm{a}_1\overline{\mathrm{E}} + \mathrm{a}_2\overline{\mathrm{E}^2} \end{aligned} \tag{A.3}$$

The effect on the cross section due to the convolution can be estimated as

$$\begin{aligned} \delta\sigma &= \sigma(\overline{\mathrm{E}}) - \sigma_{\text{convoluted}} \\ &= \mathrm{a}_2\, (\overline{\mathrm{E}}^2 - \overline{\mathrm{E}^2}) \\ &= -\mathrm{a}_2\, \omega^2 \end{aligned}$$

From equation (A.1) we get

$$\mathrm{a}_2 = \frac{1}{2}\frac{\mathrm{d}^2\sigma}{\mathrm{dE}^2} \tag{A.4}$$

We thus get the expression for $\delta\sigma$ as:

$$\delta\sigma = -\frac{1}{2}\,\omega^2\frac{\mathrm{d}^2\sigma}{\mathrm{dE}^2} \tag{A.5}$$

Appendix B

Cross Section and Asymmetry of $e^+e^- \rightarrow e^+e^-$ Events

We define the total cross section for electron in the following way,

$$\sigma_{\text{theo}} = \sigma^{\text{t+i}}_{\text{ALI}} + \text{R}\ \sigma^{\text{s}}_{\text{ZF}} \tag{B.1}$$

$$\text{R} = \frac{\sigma^{\text{s}}_{\text{ALI}}(\text{e}^-\text{e}^+ \text{ both in } 44^\circ - 136^\circ)}{\sigma^{\text{s}}_{\text{ALI}}(\text{e}^- \text{ in } 44^\circ - 136^\circ\ , \text{e}^+ \text{ in } 0^\circ - 180^\circ)} \tag{B.2}$$

$\sigma^{\text{t+i}}_{\text{ALI}}$ is the contribution of the t plus s–t interference term in the cross section, calculated using ALIBABA and $\sigma^{\text{s}}_{\text{ZF}}$ is the contribution from the s channel term, calculated using ZFITTER.

The forward backward asymmetry is defined as,

$$\text{A}_{\text{FB}} = \frac{\sigma_{\text{F}} - \sigma_{\text{B}}}{\sigma_{\text{F}} + \sigma_{\text{B}}} \tag{B.3}$$

$$\text{Forward} \Longrightarrow (\text{e}^- \text{ in } 44^\circ - 90^\circ\ ,\ \text{e}^+ \text{ in } 44^\circ - 136^\circ)$$
$$\text{Backward} \Longrightarrow (\text{e}^- \text{ in } 90^\circ - 136^\circ\ ,\ \text{e}^+ \text{ in } 44^\circ - 136^\circ)$$

We have the forward and backward cross sections as,

$$\begin{aligned} \sigma_F &= (\sigma^{\text{t+i}}_{\text{ALI}})_{\text{F}} + (\text{R}\ \sigma^{\text{s}}_{\text{ZF}})_{\text{F}} \\ &= (\sigma^{\text{t+i}}_{\text{ALI}})_{\text{F}} + \text{R}_{\text{F}}\ (\sigma^{\text{s}}_{\text{ZF}})_{\text{F}} \end{aligned} \tag{B.4}$$

$$\begin{aligned} \sigma_{\text{B}} &= (\sigma^{\text{t+i}}_{\text{ALI}})_{\text{B}} + (\text{R}\ \sigma^{\text{s}}_{\text{ZF}})_{\text{B}} \\ &= (\sigma^{\text{t+i}}_{\text{ALI}})_{\text{B}} + \text{R}_{\text{B}}\ (\sigma^{\text{s}}_{\text{ZF}})_{\text{B}} \end{aligned} \tag{B.5}$$

where we define,

$$R_F = \frac{\sigma^{s}_{\mathrm{ALI}}(e^- \text{ in } 44^\circ - 90^\circ \ , \ e^+ \text{ in } 44^\circ - 136^\circ)}{\sigma^{s}_{\mathrm{ALI}}(e^- \text{ in } 44^\circ - 90^\circ \ , \ e^+ \text{ in } 0^\circ - 180^\circ)} \tag{B.6}$$

$$R_B = \frac{\sigma^{s}_{\mathrm{ALI}}(e^- \text{ in } 90^\circ - 136^\circ \ , \ e^+ \text{ in } 44^\circ - 136^\circ)}{\sigma^{s}_{\mathrm{ALI}}(e^- \text{ in } 90^\circ - 136^\circ \ , \ e^+ \text{ in } 0^\circ - 180^\circ)} \tag{B.7}$$

The numerator of equation (B.3) becomes

$$\begin{aligned}\sigma_F - \sigma_B &= (\sigma^{t+i}_{\mathrm{ALI}})_F - (\sigma^{t+i}_{\mathrm{ALI}})_B + R_F\ (\sigma^{s}_{\mathrm{ZF}})_F - R_B\ (\sigma^{s}_{\mathrm{ZF}})_B \\ &= (\sigma^{t+i}_{\mathrm{ALI}})_{FB} + R_F\ (\sigma^{s}_{\mathrm{ZF}})_B - R_B\ (\sigma^{s}_{\mathrm{ZF}})_F \\ &\quad + (R_F + R_B)\ (A^{s}_{FB})_{ZF}\ \sigma^{s}_{\mathrm{ZF}}\end{aligned}$$

The denominator of equation (B.3) is given by

$$\sigma_F + \sigma_B = \sigma_{\mathrm{theo}} = \sigma^{t+i}_{\mathrm{ALI}} + R\ \sigma^{s}_{\mathrm{ZF}} \tag{B.8}$$

Finally we get the expression for forward backward asymmetry as,

$$\begin{aligned}A_{FB} = &\ \frac{(\sigma^{t+i}_{\mathrm{ALI}})_{FB}}{\sigma^{s}_{\mathrm{ZF}}\ (R + \frac{\sigma^{t+i}_{\mathrm{ALI}}}{\sigma^{s}_{\mathrm{ZF}}})} \\ &+ \frac{R_F\ (\sigma^{s}_{\mathrm{ZF}})_B - R_B\ (\sigma^{s}_{\mathrm{ZF}})_F}{\sigma^{s}_{\mathrm{ZF}}\ (R + \frac{\sigma^{t+i}_{\mathrm{ALI}}}{\sigma^{s}_{\mathrm{ZF}}})} \\ &+ \frac{(R_F + R_B)}{(R + \frac{\sigma^{t+i}_{\mathrm{ALI}}}{\sigma^{s}_{\mathrm{ZF}}})}\ (A^{s}_{FB})_{ZF}\end{aligned} \tag{B.9}$$

The values of R, R_F, R_B, $\sigma^{t+i}_{\mathrm{ALI}}$ etc. at different centre of mass energies calculated from ALIBABA are given in table B.1.

period	$\sqrt{s}$	σ^{t+i}_{ALI}	σ^{t+i}_{ALIFB}	R	R_F	R_B
1990	88.232	0.2273061	0.1839080	0.9924585	0.9954417	0.9905796
	89.236	0.2517507	0.2033608	0.9935337	0.9952893	0.9922325
	90.237	0.2632554	0.2120733	0.9943698	0.9952315	0.9936214
	91.230	0.1478053	0.1194070	0.9945143	0.9948002	0.9942274
	92.226	0.0190835	0.0153167	0.9937791	0.9942941	0.9931961
	93.228	0.0072142	0.0059802	0.9906903	0.9915247	0.9896631
	94.223	0.0183614	0.0148062	0.9868655	0.9887013	0.9844698
1991	91.253	0.1427678	0.1155951	0.9945915	0.9948957	0.9942854
	88.480	0.2330789	0.1878926	0.9926921	0.9953728	0.9909344
	89.470	0.2573517	0.2079048	0.9938887	0.9954573	0.9926818
	90.228	0.2632597	0.2122384	0.9944915	0.9954829	0.9936319
	91.222	0.1492914	0.1204535	0.9946074	0.9949815	0.9942324
	91.967	0.0364667	0.0292012	0.9941275	0.9943899	0.9938385
	92.966	0.0057151	0.0051484	0.9918255	0.9925945	0.9908967
	93.716	0.0120965	0.0100394	0.9889928	0.9902936	0.9873412
1992	91.294	0.1360398	0.1093479	0.9946020	0.9949643	0.9942354
1993	91.316	0.1307388	0.1053161	0.9945301	0.9948536	0.9942016
	89.449	0.2568661	0.2070016	0.9938741	0.9955501	0.9925887
	91.203	0.1526577	0.1233599	0.9946036	0.9949545	0.9942528
	93.033	0.0056538	0.0048726	0.9915249	0.9923079	0.9905743
1994	91.218	0.1498271	0.1209469	0.9945888	0.9949286	0.9942484
1995	89.452	0.2568134	0.2071268	0.9938308	0.9954948	0.9925539
	91.293	0.1357233	0.1092334	0.9945646	0.9949049	0.9942203
	92.984	0.0057879	0.0045131	0.9917631	0.9926761	0.9906588

Table B.1: The factors σ^{t+i}_{ALI}, R, etc. factors calculated at different centre of mass energies using ALIBABA

Publications of Suchandra Dutta

[1] Further Results on Cerium Fluoride Crystals.
Crystal Clear Collaboration, S.Anderson *et al.* , Nuclear Instruments and Methods **A332** (1993) 73.

[2] A Measurement of Tau Polarization at LEP.
L3 Collaboration, M. Acciarri *et al.* , Phys. Lett. **B341** (1994) 245.

[3] B^* Production in Z Decays at LEP.
L3 Collaboration, M. Acciarri *et al.* , Phys. Lett. **B345** (1995) 589.

[4] Energy and Particle flow in Three-Jet and Radiative Two-Jet Events from Hadronic Z Decays.
L3 Collaboration, M. Acciarri *et al.* , Phys. Lett. **B345** (1995) 74.

[5] Measurement of Exclusive Branching Fractions of Hadronic One-Prong Tau Decays.
L3 Collaboration, M. Acciarri *et al.* , Phys. Lett. **B345** (1995) 93.

[6] Search for Anomalous $Z \rightarrow \gamma\gamma\gamma$ Events at LEP.
L3 Collaboration, M. Acciarri *et al.* , Phys. Lett. **B345** (1995) 609.

[7] Combined Preliminary Data on Z Parameters from the LEP Experiments and Constraints
on the Standard Model.
The LEP Collaborations ALEPH, DELPHI, L3 and OPAL and
the LEP Electroweak Working Group.
CERN preprint CERN-PPE/94-187; November 25, 1994.

[8] Measurement of Energetic Single-Photon Production at LEP.
L3 Collaboration, M. Acciarri *et al.* , Phys. Lett. **B346** (1995) 190.

[9] Measurement of the Weak Charged Current Structure in Semileptonic b-hadron decays at the Z peak.
L3 Collaboration, M. Acciarri *et al.* , Phys. Lett. **B351** (1995) 375.

[10] Search for Neutralinos in Z Decays.
L3 Collaboration, M. Acciarri *et al.* , Phys. Lett. **B350** (1995) 109.

[11] Tests of QED at LEP Energies using $e^+e^- \rightarrow \gamma\gamma(\gamma)$ and $e^+e^- \rightarrow l^+l^-\gamma\gamma$.
L3 Collaboration, M. Acciarri *et al.* , Phys. Lett. **B353** (1995) 136.

[12] One-prong τ Decays with Neutral Kaons.
L3 Collaboration, M. Acciarri *et al.* , Phys. Lett. **B352** (1995) 487.

[13] Evidence for Gluon Interference in Hadronic Z Decays.
L3 Collaboration, M. Acciarri *et al.* , Phys. Lett. **B353** (1995) 145.

[14] Study of the $K^\circ_S K^\circ_S$ Final State in Two Photon Collision.
L3 Collaboration, M. Acciarri *et al.* , Phys. Lett. **B363** (1995) 118.

[15] Search for Neutral Charmless B Decays At LEP.
L3 Collaboration, M. Acciarri *et al.* , Phys. Lett. **B363** (1995) 127.

[16] Search for the Decays $B^\circ_d \rightarrow \gamma\gamma$ and $B^\circ_s \rightarrow \gamma\gamma$.
L3 Collaboration, M. Acciarri *et al.* , Phys. Lett. **B363** (1995) 137.

[17] A Combination of Preliminary LEP Electroweak Measurements and Constraints on the Standard Model.
The LEP Collaborations, ALEPH, DELPHI, L3, OPAL and
the LEP Electroweak Working Group.
CERN preprint CERN-PPE/95-172, November 25, 1994.

[18] Measurement of η Production in Two and Three-Jet Events from Hadronic Z Decays at LEP.
L3 Collaboration, M. Acciarri *et al.* , Phys. Lett. **B371** (1996) 126.

[19] Measurement of Hadron and Lepton-Pair Production at 130 GeV $< \sqrt{s} <$ 140 GeV at LEP.
L3 Collaboration, M. Acciarri *et al.* , Phys. Lett. **B370** (1996) 195.

[20] Studies of Hadronic Event Structure and α_s determination at $\sqrt{s} = 130, 136$ GeV.
L3 Collaboration, M. Acciarri *et al.* , Phys. Lett. **B371** (1996) 137.

[21] Search for Excited Leptons in e^+e^- Annihilation at $\sqrt{s} =$ 130–140 GeV.
L3 Collaboration, M. Acciarri *et al.* , Phys. Lett. **B370** (1996) 211.

[22] Measurement of Muon Pair Production at $50 < \sqrt{s} < 86$ GeV at LEP.
L3 Collaboration, M. Acciarri *et al.* , Phys. Lett. **B374** (1996) 331.

[23] Combining Heavy Flavour Electroweak Measurements at LEP.
The LEP Collaborations ALEPH, DELPHI, L3 and OPAL
Submitted to Nuclear Instruments and Methods.

[24] Search for Supersymmetric Particles at 130 GeV $< \sqrt{s} <$ 140 GeV at LEP.
L3 Collaboration, M. Acciarri *et al.* , Phys. Lett. **B377** (1996) 289.

[25] Search for Unstable Sequential Neutral and Charged Heavy Leptons in e^+e^- annihilation at $\sqrt{s} = 130$ and 136 GeV.
L3 Collaboration, M. Acciarri *et al.* , Phys. Lett. **B377** (1996) 304.

[26] Measurement of the Michel Parameters and the average tau neutrino helicity from tau decays in $e^+e^- \rightarrow \tau^+\tau^-$.
L3 Collaboration, M. Acciarri *et al.* , Phys. Lett. **B377** (1996) 313.

[27] Observation of Multiple Hard Photon Final States at $\sqrt{s} = 130$–140 GeV at LEP.
L3 Collaboration, M. Acciarri *et al.* , Phys. Lett. B, Accpted.

[28] Measurement of the Branching Ratios $b \longrightarrow e\nu X$, $\mu\nu X$, $\tau\nu X$ and νX.
L3 Collaboration, M. Acciarri *et al.* , Z. Phys. . **C71** (1996) 379.

[29] Search For New Particles In Hadronic Events With Isolated Photons.
L3 Collaboration, M. Acciarri *et al.* , Phys. Lett. B accepted

[30] Measurement of the B°_{d} Meson Oscillation Frequency.
L3 Collaboration, M. Acciarri *et al.* , Phys. Lett. **B383** (1996) 487.

[31] Search For Neutral Higgs Boson Production Through the Process $e^+e^- \rightarrow Z^* + H^{\circ}$.
L3 Collaboration, M. Acciarri *et al.* , Phys. Lett. B (accepted).

[32] Measurement of the Lifetime of the Tau Lepton.
L3 Collaboration, M. Acciarri *et al.* , Phys. Lett. B (accepted).

[33] Search for Neutral B Meson Decays to Two Charged Leptons.
L3 Collaboration, M. Acciarri *et al.* , Phys. Lett. B (submitted).

[34] Search for Exclusive B Decays to J and η or π° zero with the L3 Detector.
L3 Collaboration, M. Acciarri *et al.* , Phys. Lett. B (accepted).

[35] Measurement of Inclusive ω and η' Production in Hadronic Z Decays.
L3 Collaboration, M. Acciarri *et al.* , Phys. Lett. B (accepted).

[36] Study of the Weak Charged Hadronic Current in b Decays.
L3 Collaboration, M. Acciarri *et al.* , Phys. Lett. B (accepted).

[37] A Combination of Preliminary Electroweak Measurements and Constraints on the Standard Model.
The LEP Experiments: ALEPH, DELPHI, L3 and OPAL, the LEP Electroweak Working Group and the SLD Heavy Flavour Group.
CERN preprint CERN-PPE/96-183; 6 December 1996. L3 preprint 108.

[38] Measurement of $D_s \to \tau\overline{\nu}_\tau$ and a new limit for $B \to \tau\overline{\nu}_\tau$.
L3 Collaboration, M. Acciarri *et al.* , Phys. Lett. B (accepted).

[39] Search for Excited Leptons in e^+e^- Annihilation at $\sqrt{s}$=161 GeV.
L3 Collaboration, M. Acciarri *et al.* , Phys. Lett. B (submitted).

[40] Pair-Production of W Bosons in e^+e^- Interactions at $\sqrt{s}$=161 GeV.
L3 Collaboration, M. Acciarri *et al.* , Phys. Lett. B (accepted).

References

[1] S. L. Glashow, Nucl. Phys. **22** (1961) 579;
S. Weinberg, Phys. Rev. Lett. **19** (1967) 1264;
A. Salam, in Proceedings of the 8th Nobel Symposium, ed. N. Svartholm, (Almquist and Wiksell, Slockholm, 1968).

[2] UA1 Collaboration, C. Albajar *et al.* , Z. Phys. **C 44** (1989) 15.

[3] UA2 Collaboration, R. Ansari *et al.* , Phys. Lett. **B 186** (1987) 440.

[4] CDF, Collaboration, F. Abe *et al.* , Phys. Rev. Lett. **63** (1989) 720.

[5] J. Ellis *et al.* , Phys. Lett. **B 167** (1986) 457.

[6] G. Steigman *et al.* , Phys. Lett. **B 176** (1986) 33.

[7] UA1 Collaboration, Phys. Lett. **B 198** (1987) 271.

[8] C. Hearty *et al.* , Phys. Rev. , **D 39** (1989) 3207.

[9] U. Amaldi *et al.* , Phys. Rev. **D 36** (1987) 1385.
G. Costa *et al.* , Nucl. Phys. **B 297** (1988) 244.

[10] P. W. Higgs, Phys. Lett. **12** (1964) 132.

[11] J. Goldstone, Nuovo Cimento, 19 (1961) 154.

[12] V. Barger and R. Phillips *Collider Physics*, Addison-Wesley Publishing Company.

[13] M. Consoli *et al.* , *Z Physics at LEP 1* G. Altarelli, R. Kleiss and C. Verzegnassi CERN Yellow Report, CERN-89-08, Vol 1 (1989) 7.

[14] G. Burger *et al.* , *Z Physics at LEP 1*, eds G. Altarelli, R. Kleiss and C. Verzegnassi CERN Yellow Report, CERN-89-08, Vol 1 (1989) 55.

[15] R. Caffo *et al.* , *Z Physics at LEP 1*, eds G. Altarelli, R. Kleiss and C. Verzegnassi CERN Yellow Report, CERN-89-08, Vol 1 (1989) 171.

[16] M. Böhm *et al.* , *Z Physics at LEP 1*, eds G. Altarelli, R. Kleiss and C. Verzegnassi CERN Yellow Report, CERN-89-08, Vol 1 (1989) 203.

[17] T. Hebbeker, M. Martinez, G. Passarino and G. Quast, Phys. Lett. **B331** (1994) 165.

[18] L3 Collaboration, B. Adeva *et al.* , Nucl. Inst. Meth. **A289** (1990) 35.

[19] ALEPH Collaboration, D. Decamp *et al.* , Nucl. Inst. Meth. **A 294** (1990) 127.

[20] DELPHI Collaboration, P. Aarnio *et al.* , Nucl. Inst. Meth. **A 303** (1991) 233.

[21] OPAL Collaboration, K. Ahmet *et al.* , Nucl. Inst. Meth. **A 305** (1991) 275.

[22] S. Meyer *The LEP Collider, from design to approval and commissioning* CERN Yellow Report **CERN 91-08**.

[23] J. Jowett *The 8-bunch pretzel scheme* Proceedings of the first workshop on LEP performance, Chamonix 1991, CERN-SL **91-23**(1991).

[24] L. Arnaudon *et al.* , *The Energy Calibration of LEP in 1991* CERN-PPE **92-125**, CERN-SL **92-37**(DI).

[25] The Working Group on LEP Energy and LEP collaborations ALEPH, DELPHI, and OPAL. *Measurement of the mass of the Z boson and energy calibration of LEP* Phys. Lett. **B 307** (1993) 187, CERN-SL **93-17**.

[26] L. Arnaudon *et al.* , *Effects of Terrestial Tides on the LEP Beam Energy* CERN-SL **94-07**(AP).

[27] A. Hofmann *Performance Limitations at LEP* CERN-SL **94-58**(AP).

[28] R.Assmann *et al.* , *Energy Calibration with Resonant Depolarization at LEP in 1993* CERN-SL **94-61**(AP).

[29] L.Arnaudon *et al.* , *Accurate Determination of the LEP Beam Energy by Resonant Depolarization* CERN-SL **94-71**(BI).

[30] B.Jacobsen *1993 LEP Energy Spread and Variation From Spot Size Measurements* ALEPH **94-060**(BI).

[31] P. Collier *et al.* , *Operation Of LEP With Bunch Trains* CERN-SL **96-22** (OP).

[32] M.BÖge *et al.* , *Measurements of Collision Offsets and Diffrence in Vertical Dispersion at the LEP Interaction Points* CERN-SL **96-035**.

[33] G.Grun *et al.* , *A newly observed effect affects the LEP beam energy* CERN-SL **96-036**.

[34] G.Arduini *et al.* , *LEP1 operation, 1989-1995* CERN-SL **96-043**.

[35] B.Dhning *et al.* , *A Study of the Magnetic Dipole Field of LEP during the 1995 Energy Scan* CERN-SL **96-54**(BI).

[36] H. Akbari *et al.* , The L3 vertex detector: design and performance Nucl. Inst. Meth. **A315** (1992) 161.

[37] F. Beissel *et al.* , Construction and performance of the L3 cetral tracking detector Nucl. Inst. Meth. **A332** (1993) 33.

[38] M. Caccia *et al.* , Nucl. Inst. Meth. **A 315** (1992) 197; G. Ambrosi *et al.* , Nucl. Inst. Meth. **A 344** (1994) 133; O. Adriani *et al.* , Nucl. Inst. Meth. **A 348** (1994) 431; The L3 SMD collaboration, M. Acciarri *et al.* , Nucl. Inst. Meth. **A 351** (1994) 300; M. Acciarri *et al.* , Nucl. Inst. Meth. **A 360** (1995) 103.

[39] A. Bay *et al.* , The Xenon Monitor of the Electromagnetic Calorimeter, Nucl. Inst. Meth. **A 321** (1992) 119.

[40] The L3 BGO collaboration, J. A. Bakken *et al.* , Results on the calibration of the L3 BGO calorimeter with cosmic rays, Nucl. Inst. Meth. **A 343** (1994) 456.

[41] L3 Collaboration, O. Adriani *et al.* , Nucl. Inst. Meth. **A302** (1991) 53.

[42] The muon filter of the L3 detector, O. Adriani *et al.* , Nucl. Inst. Meth. **A 300** (1991) 493.

[43] A high resolution muon detector, B. Adeva *et al.* , Nucl. Inst. Meth. **A 323** (1992) 109.

[44] A. Adam *et al.* , Nucl. Inst. Meth. **A 383** (1996) 342.

[45] R. Bizzari *et al.* , Nucl. Inst. Meth. **A 283** (1989) 799;
P. Bagnaia *et al.* , Nucl. Inst. Meth. **A 324** (1993) 101;
P. Bagnaia *et al.* , Nucl. Inst. Meth. **A 344** (1994) 212.

[46] Y. Bertsch *et al.* , Nucl. Inst. Meth. **A 340** (1994) 309;
S.P. Beingessner *et al.* , Nucl. Inst. Meth. **A 340** (1994) 322.

[47] C. Dionisi *et al.* , Nucl. Inst. Meth. **A 336** (1993) 78.

[48] BHLUMI: Version 4.0 (Z pole), version 4.03 (above the Z pole) S. Jadach *et al.* , Comp. Phys. Comm. **70** (1992) 305 ;
S. Jadach *et al.* , Phys. Lett. **B353** (1995) 349 ;
S. Jadach *et al.* , Phys. Lett. **B353** (1995) 362 .

[49] M. Böhm, A. Denner and W. Hollik, Nucl. Phys. **B304** (1988) 687;
F. A. Berends, R. Kleiss and W. Hollik, Nucl. Phys. **B304** (1988) 712.

[50] J. H. Field and T. Riemann, private communication;
W. Beenakker in Proceedings of the Joint International Lepton-Photon Symposium & Europhysics Conference on High Energy Physics, Geneva, Switzerland 1991, Vol. 1, p. 28; M. Cacciari *et al.* , Phys. Lett. **B 286** (1992) 387.

[51] KORALZ 4.01 Monte Carlo Program is used for $\tau^+\tau^-$ and $\mu^+\mu^-$ final states:
S. Jadach, B. F. L. Ward and Z. Wąs, Comp. Phys. Comm. **79** (1994), 503.

[52] S.Jadac, J. Kühn, and Z. Was, *TAUOLA - a Library of Monte Carlo Programa to Simulate Decays of Polarized τ Leptons*, Comp. Phys. Comm. **64** (1991)275.

[53] JETSET 7.4 Monte Carlo Program:
T. Sjöstrand, Comp. Phys. Comm. **39** (1986) 347;
T. Sjöstrand and M. Bengtsson, Comp. Phys. Comm. **43** (1987) 367.

[54] X. Artru, G. Mennessier, Nucl. Phys. **B270** (1974)93 ;
B. Andersson, G. Gustafson, G.Ingelman, T. Sjöstrand, Physics Reports **97**(1983) 31.

[55] DIAG36 Monte Carlo program is used for 2γ final states:
F. A. Berends, P. H. Daverfeldt and R. Kleiss, Nucl. Phys. **B 253** (1985) 441.

[56] PYTHIA 5.6 Monte Carlo Program:
H.U. Bengtsson, T. Sjöstrand, Comp. Phys. Comm. **46** (1987) 43.

[57] R. Brun *et al.*, "GEANT 3", *User Guide*, CERN DD/EE/84-1 (Revised), September 1987.

[58] H. Fesefeldt, *The Simulation of Hadronic Showers: Physics and applications* RWTH Aachen,PITHA 85/02 (1985).

[59] L3 Collaboration, B. Adeva *et al.* , Z. Phys. **C 51** (1991) 179.

[60] L3 Collaboration, O. Adriani *et al.* , Physics Reports **236** (1993) 1.

[61] L3 Collaboration, M. Acciarri *et al.* , Z. Phys. **C 62** (1994) 551.

[62] I.C. Brock *et al.* , Luminosity Measurement in the L3 Detector at LEP, CERN-PPE **96-89**(1996) Submitted to Nucl. Inst. Meth.

[63] Particle Data Group, M. Aguilar-Benitez *et al.* Phys. Rev. **D 50** (1994) 1173.

[64] The Working Group on LEP Energy "LEP Energy Calibration in 1993, 1994 and 1995", Internal note, LEP Energy Group/96-05, July 1996.

[65] S. Brandt *et al.* , Phys. Lett. **12** (1964) 57;
E. Fahri, Phys. Rev. Lett. **39** (1977) 1587.

[66] D. Bardin *et al.* , FORTRAN package ZFITTER, Preprint CERN-TH 6443/92;
D. Bardin *et al.* , Z. Phys. **C44** (1989) 493 ;
D. Bardin *et al.* , Nucl. Phys. **B351** (1991) 1 ;
D. Bardin *et al.* , Phys. Lett. **B255** (1991) 290 .

[67] W. Beenakkar, F. A. Berends and S. C. van dar Marck, Nucl. Phys. **B349** (1991) 323.

[68] F. James, CERN program library Long Writeup 506, MINUIT, 1994.

[69] S. N. Ganguli, Treatment of Systematic Errors in Z-lineshape Fitting Procedure, **L3 Note 1267** October 1992.

[70] S. N. Ganguli, Implementation of LEP energy uncertainty in the L3 Lineshape Fitting Package, **L3 Note 1194** July 1992.

[71] S. N. Ganguli and M. N. Kienzle-Focacci, Some details on the Z lineshape fitting procedure using $e^+e^- \rightarrow e^+e^-$ data, **L3 Note 1396** April 1993.

[72] D. Bourilkov and A. Gurtu, Fitting $e^+e^- \rightarrow e^+e^-$ channel at LEP energies, **L3 Note 1581** March 1994.

[73] S. Dutta, S. N. Ganguli and A. Gurtu, Improvements in the Z lineshape fitting package, **L3 Note 1904** January 1996.

[74] L3 Collaboration, O. Adriani *et al.* , Phys. Lett. **B 309** (1993) 451.

[75] M. L. Swartz, *Reevaluation of Hadroni Contribution to* $\alpha(\mathrm{M_Z}^2)$,SLAC-PUB-6710, November 1994, SLAC-PUB-95-7001, September 1995.

[76] A. D. Martin and D. Zeppenfeld, Phys. Lett. **B345** (1994) 558.

[77] H. Burkhardt and B. Pietrzyk, Phys. Lett. **B356** (1995) 398.

[78] S. Eidelman and F. Jegerlehner, Z. Phys. , **C67** (1995) 585.

[79] The LEP Collaborations ALEPH, DELPHI, L3, OPAL and LEP Electroweak Working Group, *Updated Parameters of the Z Resonance from Combined Preliminary Data of LEP Experiments*, CERN-PPE/93-157.

[80] ALEPH Collaboration, D. Decamp *et al.* , Z. Phys. **C 48** (1990) 365;
ALEPH Collaboration, D. Decamp *et al.* , Z. Phys. **C 53** (1992) 1;
ALEPH Collaboration, D. Buskulic *et al.* , Z. Phys. **C 60** (1993) 71;
ALEPH Collaboration, D. Buskulic *et al.* , Z. Phys. **C 62** (1994) 539;
ALEPH Collaboration, *Preliminary Results on Z Production Cross Section and Lepton Forward-Backward Asymmetries using the 1990-1995 Data*, contributed paper to ICHEP96, **PA-07-069.**

[81] DELPHI Collaboration, P. Aarnio *et al.* , Nucl. Phys. **B 367** (1991) 511;
DELPHI Collaboration, P. Abreu *et al.* , Nucl. Phys. **B 417** (1994) 3;
DELPHI Collaboration, P. Abreu *et al.* , Nucl. Phys. **B 418** (1994) 403;
DELPHI Collaboration, DELPHI Note 95-62 PHYS 497, July 1995;
DELPHI Collaboration, DELPHI Note 96-118 CONF 65, contributed paper to ICHEP96, **PA-07-001.**

[82] OPAL Collaboration, G. Alexander *et al.* , Z. Phys. **C 52** (1991) 175;
OPAL Collaboration, P. D. Acton *et al.* , Z. Phys. **C 58** (1993) 219;
OPAL Collaboration, R. Akers *et al.* , Z. Phys. **C 61** (1994) 19;
OPAL Collaboration, *A Preliminary Update of the Z^0 Line Shape and Lepton Asymmetry Measurements with the 1993 and 1994 Data*, OPAL Physics Note **PN 166,** February 1996;
OPAL Collaboration, *The Preliminary OPAL SiW luminosity analysis: Results for the 1994 Summer conferences*, OPAL Physics Note **PN 142,** July 1994;
OPAL Collaboration, *A Preliminary Update of the Z Line Shape and Lepton Asymmetry Measurements with a Revised 1993-1994 LEP energy and 1995 Lepton Asymmetry*, OPAL Physics Note **PN 242,** July 1996.

[83] L3 Collaboration, *Preliminary L3 Results on Electroweak Parameters using 1990-1995 Data*, **L3note 1980** August 1996.

[84] ALEPH Collaboration, D. Buskulic *et al.* , Z. Phys. **C 69** (1996) 183.

[85] DELPHI Collaboration, P. Abreu *et al.* , Z. Phys. **C 67** (1995) 183.
DELPHI Collaboration, *An updated measurement of tau polarisation*, DELPHI 96-114 CONF 42, contributed paper to ICHEP96, Warsaw, 25-31 July 1996, **PA07-006.**

[86] L3 Collaboration, O. Acciari *et al.* , Phys. Lett. **B 341** (1994) 245.

[87] A Preliminary Update of A_τ and A_e Using 1994 Data, **L3 Note 1792** 1995.

[88] OPAL Collaboration, G. Alexander *et al.* , *A Precise Measurement of the Tau Polarisation and its Forward-Backward Asymmetry at LEP* CERN-PPE/96-078, Submitted to Z. Phys. C.

[89] ALEPH Collaboration, D. Buskulic *et al.* , Z. Phys. **C 71** (1996) 357.

[90] DELPHI Collaboration, P. Abreu *et al.* , Phys. Lett. **B 227** (1992) 371;
DELPHI Collaboration, *Measurement of Inclusive Charge Flow in Hadronic Z decays,* DELPHI 96-19 PHYS 594.

[91] OPAL Collaboration, P. D. Acton *et al.* , Phys. Lett. **B 294** (1992) 436;
OPAL Collaboration, OPAL Physics Note, PN 195 (1995).

[92] ALEPH Collaboration, D.Buskulic *et al.* , Phys. Lett. . **B 335** (1994) 99;
ALEPH Collaboration, *An Upgraded Measurement of* $A_{FB}^{b\bar{b}}$ *from the charge asymmetry in Lifetime Tagged Z Decays* contributed paper to ICHEP96, Warsaw, 25-31 July 1996 **PA10-018.**

[93] ALEPH Collaboration, D. Buskulic *et al.* , Z. Phys. **C 62** (1994) 1;
ALEPH Collaboration, D. Buskulic *et al.* ,*The Forward–Backward Asymmetry for Charm Quarks at the Z pole: an Update*, Contributed Paper to EPS-HEP-95 Brussels, **eps0634.**

[94] DELPHI Collaboration, P.Abreu *et al.* , Z. Phys. **C 65** (1995) 569;
DELPHI Collaboration, P.Abreu *et al.* , Z. Phys. **C 66** (1995) 341;
DELPHI Collaboration, *Measurement of the Forward-Backward Asymmetries of* $e^+e^- \rightarrow Z \rightarrow b\bar{b}$ *and* $e^+e^- \rightarrow Z \rightarrow c\bar{c}$, DELPHI 95-87 PHYS 522.

[95] L3 Collaboration, O. Adriani *et al.* , Phys. Lett. **B 292** (1992) 454.

[96] L3 Collaboration, M. Acciarri *et al.* ,Phys. Lett. **B 335** (1994) 542.

[97] L3 Collaboration, *Measurement of* R_b *and* $BR(B \rightarrow l)$ *from b-quark semileptonic decays,* **L3 Note 1449**, July 16 1993.

[98] L3 Collaboration, I. Brock *et al.* , *L3 Results on* $A_{FB}^{b\bar{b}}$, $A_{FB}^{c\bar{c}}$ *and* χ *for the Glasgow Conference,* **L3 Note 1624.**

[99] OPAL Collaboration, R. Akers *et al.* , Z. Phys. **C 67** (1995) 365.

[100] OPAL Collaboration, CERN-PPE/96-101 24 July 1996.

[101] ALEPH Collaboration, D. Buskulic *et al.* , Z. Phys. **C 62** (1994) 179;
ALEPH Collaboration, D. Buskulic *et al.* , Phys. Lett. **B 384** (1996)414;
ALEPH Collaboration, D. Buskulic *et al.* , *Measurement of the semileptonic b branching ratios from inclusive leptons in Z decays*, Contributed Paper to EPS-HEP-95 Brussels, **eps0404**.

[102] ALEPH Collaboration, *Measurement of Rb using a Lifetime-Mass Tag*, contributed paper to ICHEP96, Warsaw, 25-31 July 1996 **PA10-014**;
ALEPH Collaboration, *A Measurement of* R_b *using Mutually Exclusive Tags*, contributed paper to ICHEP96, Warsaw, 25-31 July 1996 **PA10-015**.

[103] DELPHI Collaboration, P.Abreu *et al.* , Z. Phys. **C 66** (1995) 323.

[104] DELPHI Collaboration, P. Abreu *et al.* , Z. Phys. **C70** (1996) 531;
DELPHI Collaboration, P. Abreu *et al.* , *Measurement of the partial decay width* $R_b = \Gamma_{b\bar{b}}/\Gamma_{had}$ *with the DELPHI detector at LEP* , contributed paper to ICHEP96, Warsaw, 25-31 July 1996 **PA01-061**.

[105] L3 Collaboration, O. Adriani *et al.* , Phys. Lett. **B 307** (1993) 237.

[106] L3 Collaboration, *Measurement of the Z Branching Fraction into Bottom Quarks Using Lifetime Tags*, contributed paper to ICHEP96, Warsaw, 25-31 July 1996 **PA05-049**.

[107] OPAL Collaboration, G. Alexander *et al.* , Z. Phys. **C 70** (1996) 357;
OPAL Collaboration, R. Akers *et al.* , *Updated Measurement of the Heavy Quark Forward-Backward Asymmetries and Average B Mixing Using Leptons in Multihadronic Events*, OPAL Physics Note PN226 contributed paper to ICHEP96, Warsaw, 25-31 July 1996 **PA05-007**.

[108] OPAL Collaboration, R. Akers *et al.* , Z. Phys. **C 65** (1995) 17;
OPAL Collaboration, *An Update of the Measurement of* $\Gamma_{b\bar{b}}/\Gamma_{had}$ *using a Double Tagging Method*, OPAL Physics Note PN181.

[109] ALEPH Collaboration, *Measurement of the partial decay width of the Z into* $c\bar{c}$ *quarks* contributed paper to ICHEP96, Warsaw, 25-31 July 1996 **PA10-016**. The results of the exclusive-exclusive and inclusive-exclusive double-tag D-meson measurements have been averaged for this note.

[110] DELPHI Collaboration, *Summary of* R_c *measurements in DELPHI*, DELPHI 96-110 CONF 37 contributed paper to ICHEP96, Warsaw, 25-31 July 1996 **PA01-060**.

[111] OPAL Collaboration, R. Akers *et al.* , Z. Phys. **C 67** (1995) 27;
OPAL Collaboration, G. Alexander *et al.* , Z. Phys. **C 72** (1996) 1;
OPAL Collaboration, *A measurement of* $BR(c \to D^*)$ *and* $\Gamma_{c\bar{c}}/\Gamma_{had}$ *using a double tagging method*, OPAL Physics Note PN227 contributed paper to ICHEP96, Warsaw, 25-31 July 1996 **PA05-011**.

[112] SLD Collaboration, K. Abe *et al.* , Phys. Rev. Lett. **73** (1994) 25.

[113] M. Woods,*The SLD ALR Result and Review of Weak Mixing Angle Results at LEP and SLC*, Talk given at the EPS-HEP-95 Conference, Brussels, to appear in the Proceedings.

[114] SLD Collaboration, *Measurement of* R_b *at SLD*, contributed paper to ICHEP96, Warsaw, 25-31 July 1996 **PA10–23**.

[115] *Left-right Forward-backward Asymmetry for c and b Quarks*, contributed paper to ICHEP96, Warsaw, 25-31 July 1996 **PA10–26**.

[116] UA2 Collaboration, J. Alitti *et al.* , Phys. Lett. **B276** (1992) 354.

[117] CDF Collaboration, F. Abe *et al.* , Phys. Rev. Lett. **65** (1990) 2243 and Phys. Rev. **D43** (1991) 2070.

[118] CDF Collaboration, F. Abe *et al.* , *Measurement of the W Boson Mass*, FERMILAB-PUB-95/033-E and FERMILAB-PUB-95/035-1995.

[119] DØ Collaboration, preliminary result presented by U. Heintz, Les Rencontres de Physique de la Vallee d'Aoste, La Thuile, March 1996.

[120] CDF Collaboration, *Measurement of the Top Quark Mass at CDF*, contributed paper to ICHEP96, PA-08-018.

[121] DØ Collaboration, *Measurement of the top mass from events with two isolated leptons produced in* $p\bar{p}$ *collisions at DØ*, contributed paper to ICHEP96, PA-05-027;
DØ Collaboration, *Measurement of the top mass from events with single isolated leptons produced in* $p\bar{p}$ *collisions at DØ*, contributed paper to ICHEP96, PA-05-028.

[122] P. Grannis, talk presented at ICHEP96, to appear in the proceedings.

[123] CDHS Collaboration, H. Abramowicz *et al.* , Phys. Rev. Lett. **57** (1986) 298;
CDHS Collaboration, A. Blondel *et al.* , Z. Phys. **C45** (1990) 361.

[124] CHARM Collaboration, J.V. Allaby *et al.* , Phys. Lett. **B177** (1986) 446;
CHARM Collaboration, J.V. Allaby *et al.* , Z. Phys. **C36** (1987) 611.

[125] CCFR Collaboration, K. McFarland, *An improved measurement of* $\sin^2\theta_W$ *from neutrino-nucleon deep inelastic scattering*, proceedings of the XV workshop on Weak Interactions and Neutrinos, Talloires France, G. Bonneaud *et al.* eds., Tufts University and L.A.L. Orsay (Sept.1996) vol II p. 607.

[126] *Reports of the working group on precision calculations for the Z resonance*, eds. D. Bardin, W. Hollik and G. Passarino, CERN Yellow Report 95-03, Geneva, 31 March 1995.

[127] S. Bethke, Proceedings of the Linear Collider Workshop in Waikoloa/Hawaii, April 1993;
S. Catani, Proc. of the EPS Conference on High-Energy Physics, Marseille, July 22-28, 1993, Editions Frontieres, Ed. J. Carr-M. Perrottet, page 771 ;
S. Banerjee, Proc. of the EPS Conference on High-Energy Physics, Marseille, July 22-28, 1993, Editions Frontieres, Ed. J. Carr-M. Perrottet, page 299.

[128] S. Bethke, Proceedings of the QCD '94 Conference, Montpellier, France,Nucl. Phys. (Proc. Suppl.) **39B,C** (1995) 198.

[129] A Combination of Preliminary Electroweak Measurements and Constraints on the Standard Model.
The LEP Experiments: ALEPH, DELPHI, L3 and OPAL, the LEP Electroweak Working Group and the SLD Heavy Flavour Group.
CERN preprint CERN-PPE/96-183; 6 December 1996. L3 preprint 108.